Diss. ETH No. 14548

Development of Microzonation Methods: Application to Basle, Switzerland

A dissertation submitted to the
SWISS FEDERAL INSTITUTE OF TECHNOLOGY ZÜRICH
for the degree of

Doctor of Natural Sciences

presented by
Fortunat Johannes Paul Kind
Dipl. Math. ETH
born March 10, 1971
citizen of Chur, (GR)

accepted on the recomendation of

Prof. Dr. Domenico Giardini, examiner
Dr. Donat Fäh, co-examiner
Prof. Dr. Frank Scherbaum, co-examiner
PD Dr. Peter Huggenberger, co-examiner

2002

Contents

List of Figures

List of Tables

Zusammenfassung

In dieser Arbeit werden die lokalen Standorteffekte bei Erdbeben in der Stadt Basel in der Schweiz untersucht und eine seismischen Mikrozonierungskarte zusammengestellt. Aufgrund fehlender Starkbebenaufzeichnungen wurde der indirekte Weg über die Bestimmung der geophysikalischen Untergrundstruktur unter der Region Basel und numerische Modelierung gewählt. Neben den direkten Resultaten für die Stadt Basel ist auch die Weiterentwicklung von kostengünstigen Methoden für solche Studien ein Teilziel der Arbeit. Der Schwerpunkt liegt dabei bei Methoden, die auf der natürlichen seismischen Bodenunruhe beruhen, da sie mit geringem finanziellem Aufwand verbunden sind und auch innerhalb einer Stadt angewandt werden koennen.

In einem ersten Teil wird eine Karte der fundamentalen Resonanzfrequenzen des Untergrundes mittels der H/V Polarisationsanalyse von seismischer Bodenunruhe erstellt. Zum einen gibt die Fundamentalfrequenz eine untere Grenze für denjenigen Frequenzbereich an, in welchem mit einer Verstärkung der Bodenbewegung während eines Erdbebens gerechnet werden muss. Sie ist daher schon für sich eine wichtige Grösse in einer Mikrozonierung. Andererseits ist die Fundamentalfrequenz über die S-Wellen Geschwindigkeit mit der Tiefe des S-Wellenkontrastes verbunden, der für die Standorteffekte verantwortlich ist, was eine Interretation der Fundamentalfrequenz für die Struktur erlaubt, falls die S-Wellen Geschwindigkeiten bekannt sind. Innerhalb der Rheingrabenstruktur sind die Fundamentalfrequenzen sehr tief (0.4-1Hz), was auf weiche Sedimente bis in grosse Tiefen hindeutet. Durch die grosse Dichte der Messungen im Stadtgebiet von Basel war der Vergleich benachbarter Messungen möglich und erlaubte eine zuverlässige Interpolation der Frequenzen.

In einem zweiten Teil der Arbeit wurde eine Methode zur Bestimmung von S-Wellen Geschwindigkeiten entwickelt. Scherwellen sind einer der kritischen Faktoren bei lokalen Standorteffekten und sie sind häufig nur ungenügend bekannt. Die Methode basiert auf der Aufzeichnung von natürlicher Bodenunruhe mittels eines seismischen Arrays von sehr kleiner Ausdehnung. Nach erfolgreichen Tests der Methode wurden an fünf Standorten in Basel Messungen durchgeführt und damit S-Wellen Geschwindigkeiten bis in über 100m Tiefe bestimmt.

Mit einem geologischen 3D Modell als Ausgangsbasis wurde dann in einem dritten Teil ein geophysikalisches 3D Modell der oberflächennahen Geologie er-

stellt (Tiefe ca 1km). Verwendet wurden die Daten aus den Array Messungen, Informationen aus der Literatur, von einem neuen tiefen Bohrloch in Basel und von zwei neueren seismischen Linien. Zur Validierung wurden die Fundamentalfrequenzen aus dem Modell bestimmt und mit den gemessenen Werten verglichen. Der Vergleich zeigte, dass die Tiefe der weichen Sedimente unter der Stadt Basel bisher unterschätzt worden war, und erlaubte eine Korrektur der geologischen Information.

In einem letzten Teil wurden Erdbeben auf dem Modell simuliert. Aus dem Vergleich mit Modellierungen auf einer Referenzstruktur wurde die spektrale Amplifikation der Bodenbewegung bestimmt. Über die Fundamentalfrequenzen und Amplifikationskurven konnte die Stadt Basel schlussendlich in Zonen ähnlichen Verhaltens bei Erdbeben eingeteilt werden.

Abstract

In this thesis the local site effects during earthquakes in the city of Basle in Switzerland are studied and a seismic microzonation map is determined. Because strong motion recordings are not available, an indirect approach was chosen, consisting in building a geophysical structural model for the region of Basle and then numerical simulation of earthquakes. Beside the results for the city of Basle itself, the development of inexpensive methods for determining structural information was a goal of the study. Techniques based on the analysis of ambient vibrations are a major part of the study, because they can be applied readily even in urban areas.

In the first part of this work we derive a map of the fundamental frequency of resonance of the ground from single station recordings of ambient vibrations, through H/V polarization analysis of ambient vibrations. The fundamental frequency on one hand indicates the lower boundary of the frequency range where ground motion amplification occurs and therefore gives already indications for a microzonation. On the other hand the fundamental frequency of resonance is linked through the S-wave velocity to the depth of the impedance contrast responsible for the local site effects, allowing structural interpretation of the frequency if the the velocity structure is known. Within the Rhine graben structure the fundamental frequencies are quite low (0.4-1Hz), which indicates soft sediments of large thickness. Because of the high density of the measurements in the city of Basle, a comparison of neighbouring measurements was possible and allowed a reliable interpolation of the frequencies.

In a second part of the thesis a method for determining S-wave velocity structures was developed. S-waves are a major factor in local site effects during earthquakes and they are often not sufficiently constrained. The method is based on recordings of ambient vibrations on seismic arrays of small aperture. After successful test, the method was applied at five sites in Basle and S-wave velocities for depths of more than 100m were determined

Starting from a geological 3D model, a geophysical 3D model of the close surface sediments (depth 1km) was determined in a third part of the thesis. The array measurement results were a major contribution, further information was taken from literature, from a recent deep borehole in Basle and from two recent seismic lines. Fundamental frequencies were then determined from the

model so as to validate the model against the measured values. The comparison showed that the depth of the soft sediments beneath the city of Basle had been underestimated previously. A correction of the geologic information was then possible with this data.

In the last part of the study scenario earthquakes were simulated on the model. From the comparison with numerical modelling of the identical events on a reference structure spectral amplification of the ground motion could be determined. Using the fundamental frequencies of resonance and the calculated amplification, the city of Basle was zoned into areas of similar behaviour during earthquakes.

Chapter 1

Introduction

Recent earthquakes (Michocan, Loma Prieta, Kobe, Izmit) have shown that society has yet to learn how to sufficiently mitigate the risk associated to the recurrence of earthquakes. Earthquakes are the most important natural disasters that can affect the area of Switzerland (Bundesamt für Zivilschutz, 1995). Exposure and vulnerability to the effects of earthquakes are not known sufficiently for this area, and the vulnerability is increasing as urban centers grow. Although the present seismicity in Switzerland is moderate, strong earthquakes have occurred during the last centuries. Basle was severely damaged by the earthquake in 1356 (MSK intensity IX-X) and the region of Sion has been the seismically most active region in Switzerland during the last 125 years (Rüttener, 1995), to the point that the new national hazard map of Italy, which covers also bordering areas, assigns a higher probability of ground shaking to the Valais than to eastern Sicily, a region notorious for its disastrous earthquakes.

The first seismic hazard study for Switzerland was conducted by Mayer Rosa & Merz (1976) with a probabilistic approach (Cornell, 1968) and lead to comprehensive seismic hazard maps (Sägesser & Mayer Rosa, 1978; Müller & Mayer Rosa, 1980), which are used in the current Swiss building code SIA160. So far macroseismic intensity was chosen as the hazard parameter due to the lack of strong motion data. The historical record contains data for the last 1000 years, the events are shown in Fig 1.1. The city of Basle is marked by a cluster of earthquakes, the 1356 event being the largest known for Switzerland. Although the Basle area has been relatively quiet in the last decades, the possibility for large earthquakes is present.

To address the issue of seismic hazard and risk in Switzerland further, the research project "Earthquake Scenarios for Switzerland" has been initiated by the Swiss Seismological Service, with the cooperation of the Institute of Structural Engineering at ETH Zürich and the Geologic- Paleontologic Institute of the University of Basle. The project consists of four parts. In a pilot study paleoseismic investigation aim at better constraining the return period for large earthquakes and at extending the earthquake record used for the probabilistic hazard assess-

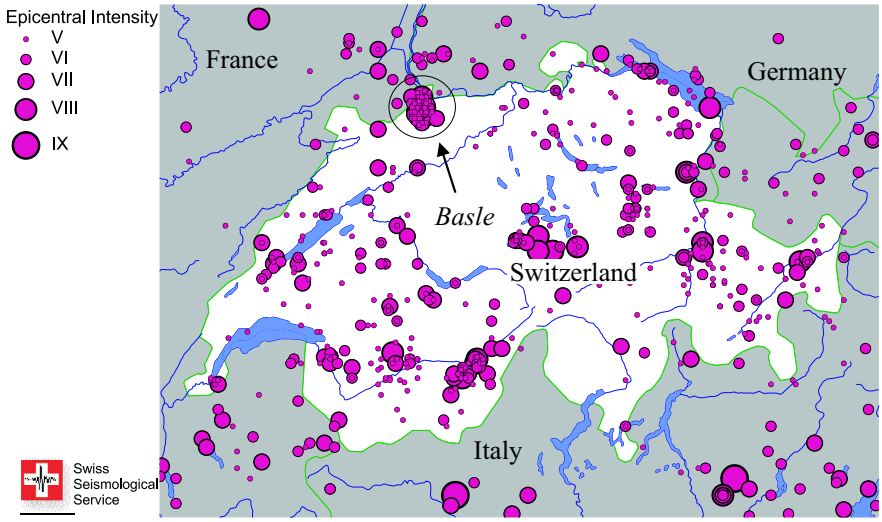

Figure 1.1: Macroseismic Earthquake Catalogue of Switzerland, 1021-1999

ment (Becker et al., 2000, 2001). In a second part the ground motion attenuation model for Switzerland is calibrated, to improve the probabilistic seismic hazard assessment (Bay, 2002). The third part (this thesis) provides information on local site conditions in Basle, on methods to derive such information and the computation of amplification in the different locations in Basle. The fourth part then consists of a vulnerability analysis of buildings in the City of Basle (Lang, 2001). By combining parts two to four of the project realistic damage scenarios for the city of Basle can be calculated. An example of such damage scenarios was derived early in the earthquake scenario project (Fäh et al., 2001b).

Microzonation

As a result of the heterogeneity of the earth's crust, seismic waves undergo multiple reflections, refractions and transformations on their path from the earthquake source to the site of observation. This phenomenon is most pronounced near the earth surface, where geological and geotechnical conditions vary strongly. As a result, whenever an earthquake strikes, the pattern of destruction follows the invisible lines of the geophysical ground properties; one building being destroyed, while a neighbouring building of similar construction remains intact. Mapping the effects of local site conditions is the main task of microzonation.

There are many forms of local phenomena summarized by the term local site effect. In general some form of amplification or deamplification of the seismic wave energy, caused by the local ground structure is meant. Further effects are liquefaction of the ground, induced land slides or rock falls and other nonlinear behaviour of the soil. In this study the focus is on the phenomena associated with the amplification of seismic wave energy, because only the knowledge about

the seismic wave amplification allows a further determination of nonlinear or secondary effects. Good reviews on the subject of local site effects are eg. Faccioli (1991), Finn (1991) or Kudo (1995).

The fundamental phenomenon responsible for the amplification of ground motion over soft sediments is the trapping of seismic waves due to the impedance contrast between sediments and the underlying bedrock. When the structure is horizontally layered (one-dimensional case), this trapping affects only body waves, which travel up and down in the surface layers. In the more realistic case lateral heterogeneities are present and can trap also surface waves. Heterogeneities can be thickness variations in sediment-filled valleys or the basin edges. At such lateral heterogeneities additional surface waves are generated through wave conversion, causing ground motion amplification. Also the topography has been observed to cause amplification at hill crests and deamplification at hill bases through focusing and scattering of wave energy. Finally 2D and 3D structures can be excited in their Eigenmodes. The type and distance of the source is very important for all site effects, as the type of wave and its angle of incidence determine the level of amplification.

A microzonation study assumes that the degree of regional seismic hazard – the expected ground shaking – is already known from the probabilistic hazard maps or from deterministic earthquake scenarios. The site effects are then understood as a frequency dependent amplification of the ground motion, relative to a real or virtual reference site for which the regional seismic hazard is known. Methods to assess the amplification can be divided into empirical and indirect approaches (modeling). No standardized method exists: Up to now each study has to make the best out of the constraints given by the site and the available information. We will outline here the most commonly used approaches, without claiming completeness of the list.

Empirical approaches: A number of empirical methods to derive the amplification have been explored. The most direct approach is the determination of standard spectral ratios, where the ground motion spectrum from earthquake data at a site are divided by the respective spectrum from a reference site nearby (Borcherdt, 1970). The distance between sample site and reference site has to be small compared to the distance between sample site and hypocenter, such that the differences in the recorded motion at the two sites are only caused by the local ground structure. The problem with this technique is firstly the need for a large number of seismic instruments and a high seismicity to allow enough recordings from earthquakes. The second difficulty is the availability of a reference site in the vicinity of the stations. Often reference sites have to be chosen that are biased by their own local structure, or reference sites that are too far away.

The use of ambient vibrations to overcome the lack of earthquake data has been tested in several studies, with ambiguous results (Rovelli et al., 1991; Guttierez & Singh, 1992; Yamanka et al., 1993; Field & Jacob, 1995). While there is no lack of signal, the sources are unknown and the correlation of the signals

between sample site and reference site can vary between very high and inexistent, depending on frequency range and location. The need for results often prevails over the scientific reliability of the method. Reference sites close enough to the sample site to guarantee the correlation of the signals are almost impossible to find except for very special cases.

A further approach to avoid the uncertainty involved with reference sites is the use of a surface instrument and a borehole instrument at the depth of the seismic contrast responsible for amplifications. Here the actual amplification through the local site conditions can be determined. The problems are here the high instrumentation costs caused by the borehole and the need for high seismicity and many instrumented sites.

An alternative empirical method is to derive site effects from macroseismic observations of damage distributions (ISSMFE, 1994; Jongmanns & Campillo, 1990; Kagami et al., 1995). But again much data has to be available beforehand and the link is very weak between observed damage and the physical parameters needed by the engineers for prevention measures in construction.

Indirect approaches: The indirect approaches to assess amplification effects circumvent the lack of earthquake or other empirical data by generating them synthetically. Geophysical models of the sites are constructed and the amplification is then determined with numerical methods. The level of sophistication is various here, reaching from simplifications based only on the shear wave velocity contrast between soft sediments and bedrock up to numerical modeling of earthquake scenarios on a detailed geophysical model. While for a given structural model various numerical methods for the calculation of possible amplifications exist, the problems lie in the determination of the subsurface structure. The relevant parameters are wave propagation velocities, quality factors for the propagation and the density of the sediments. Especially the S-wave velocity is difficult and costly to measure and can limit the reliability of a model. The knowledge about the depth and geometry of deep basins filled with sediments can be another limiting factor, and also limits the applicability of numerical methods.

A simplifying approach to the determination of local site effects can also be the definition of representative site classes for a region. Within each site class the amplification capability is determined at a representative site. At all other sites only the site class has to be identified. For this type of approach many attempts have been made to associate geotechnical or geological properties with site amplification. The applicability though of such attempts is limited, because they are often reduced to surface investigations and the deeper structures such as sedimentary basins cannot be identified.

At hardly any location are the necessary dense instrumental or macroseismic data available to allow for an empirical evaluation of local site effects, and neither are the detailed structural models available. This is also the case for Switzerland and Basle. But while the lack of earthquake data cannot be actively overcome, the structure at a site can be investigated. So an indirect approach through modeling

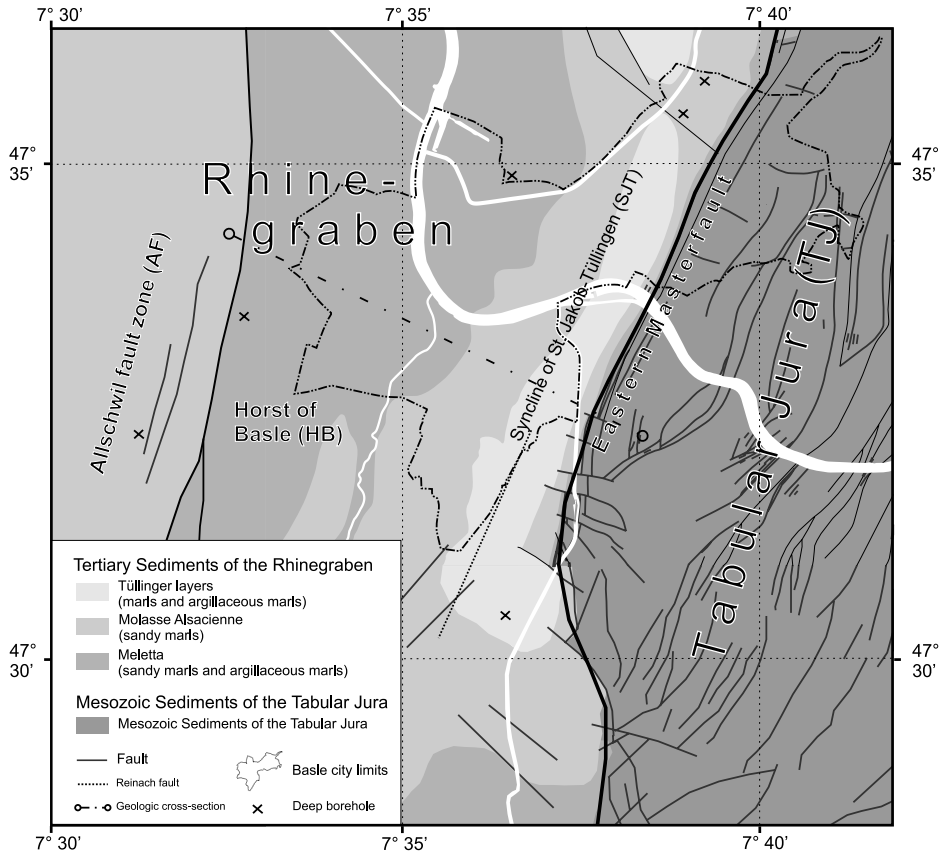

Figure 1.2: Stratigraphic units below the surficial Quaternary sediments in the Basle area (modified after Noack et al. (1999)).

has to be chosen. Currently the investigation of deeper structural properties with boreholes or seismic methods are very cost intensive and difficult to apply in urban areas. In this study we contribute to the development of cost efficient methods to determine structural properties to depth. Especially for the S-wave velocities where The lack of cost efficient methods – applicable in urban areas – is the field where this study contributes, beside the determination of site amplification for the city of Basle. Especially for the measurement of S-wave velocities, new methods have to be found.

In microzonation the link to the civil engineers has to be made. The current Swiss Building Codes, SIA160, and the future Swiss Codes and European Codes do take earthquake hazard into account in the form of response spectra for acceleration or displacement of the ground motion. The products of a seismic hazard zonation have to be compliant with the input parameters needed by the engineers, therefore the amplification of response spectra are a good way to express local site effects.

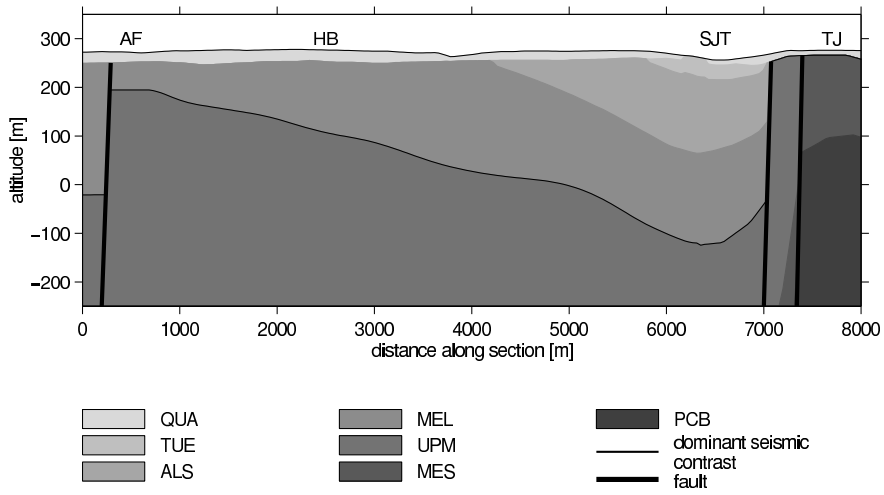

Figure 1.3: Representative cross-section of the geology in Basle. Table 4.1 explains the stratigraphic units represented by the abbreviations. The dominant seismic S-wave velocity contrast is indicated as a line between MEL and UPM.

Motivation and thesis outline

A qualitative microzonation for the city of Basle has already been performed by Fäh et al. (1997b). The zonation was mainly based on the properties of the quaternary sediments, plus the influence of the ground water table, the bedrock lithology and the distance to the eastern master fault of the Rhine Graben. A major finding in the study was the very low fundamental frequencies of resonance within the Rhine Graben, indicating that much deeper sediments are involved in site amplifications. As there was no earthquake data or reference amplification data for similar sites available, the result was limited to qualitative modifications of the ground motion and no quantitative values could be determined. The results indicate that the deep Rhine Graben structure might cause high levels of ground motion amplification, which should be assessed quantitatively.

In order to provide a quantitative microzonation for Basle, an indirect approach is chosen. First the structure is determined and then numerical modelling performed to determine ground motion amplification. The aim of this study is twofold: 1) Methods for determining structure and site effects in a cost efficient way are developed and tested. 2) We provide site amplification results for the city of Basle. We use existing methods, develop and apply new techniques to determine the structure, then calculate amplifications on the determined structure. Techniques based on the analysis of ambient vibrations are a major part of the study, because they can be applied readily even in urban areas.

In the first part of this work we derive a map of the fundamental frequency of resonance of the ground from single station recordings of ambient vibrations, through H/V polarization analysis. The fundamental frequency on one hand

indicates the lower boundary of the frequency range where ground motion amplification occurs and therefore gives already indications for a microzonation. In addition the fundamental frequency of resonance is linked through the S-wave velocity to the depth of the impedance contrast responsible for the local site effects. In a second part a technique for determining S-wave velocity structures based on ambient vibration recordings on a small scale array is developed. The S-wave velocity is a crucial parameter in site amplification and often badly constrained. Subsequently the technique is applied at several sites in Basle to derive S-wave velocities especially for the deeper sediments. Thirdly the structural model is constructed from a geological 3D model by assigning velocity profiles from the measurements and collected literature values. The model is validated against the measured fundamental frequencies, which shows that the thickness of the sediments with low S-wave velocities had been underestimated in many parts of the city. The fourth and last part is then the calculation of site amplification on 2D sections of the full model.

Geology of the Basle area

A general overview of the geology in the Basle area is given in Fig. 1.2. The city of Basle is close to the eastern master fault of the Southern Rhine Graben. The vertical offset at the border fault of the Rhine Graben is about 1400m. Within the Rhine Graben (on the down-thrown side), the Mesozoic strata (Triassic to Jurassic; UPM, MES, PCB) are covered by 500 to 1000m of Tertiary sediments. Three main Graben structures can be distinguished in the Basle area (Fischer et al., 1971; Gürler et al., 1987). The most recent Oligocene sediments in the area were deposited in the asymmetric syncline of St. Jakob-Tüllingen (SJT) adjacent to the main border fault. To the west the Rhine-Graben then rises to the horst of Basle (HB). Further west follows the "Allschwil fault zone" (AF), which sets off the Graben sediments in the order of 500m. The profile in Fig. 1.3 illustrates these structures.

The sedimentary composition of the Tertiary layers is known by outcrops located predominantly at the Graben borders, six deep drill holes, and a dense network of more than 3000 shallow boreholes drilled to the base of the Quaternary for geotechnical and ground water purposes (Noack, 1993). The following Oligocene layers can be distinguished in the boreholes (Fig. 1.3): the mostly argillaceous marls and clays of the Meletta layers (MEL, max. 350m thick), which become sandier towards its transition to the "Molasse Alsacienne" (ALS). The "Molasse Alsacienne", with a maximum thickness of 300m, is an intercalation of sandy layers and argillaceous marls. The topmost Tüllinger layers (TUE, max. 200m thick) consist of calcareous to argillaceous marls alternating with freshwater carbonates. Gypsum is frequent at their base. Carbonates are found predominantly in the northern part, whereas the marly facies is more developed towards the south.

Above the Tertiary sediments, 5 to 40m of Pleistocene and Holocene sandy gravels (QUA) were deposit by the River Rhine and its tributaries. The composition of the gravels is well known throughout the urban area from the borehole database. To the east, on the shoulder of the Rhine-Graben, the Mesozoic sediments of the Tabular Jura are covered directly by 5 to 50m thick Pleistocene and Holocene colluvial deposits and isolated patches of Pleistocene gravels. In the Rhine valley up to 45m of mostly sandy Rhine gravels overlay Mesozoic bedrock.

Chapter 2

H/V Polarization Survey of the Region of Basle

2.1 Introduction

Made well known by Nakamura (1989), the use of the H/V polarization method to derive fundamental frequencies of the ground has become increasingly popular during the last decade, mostly because of its simplicity in application. Experimental as well as theoretical studies (eg. Field & Jacob, 1995; Lermo & Chavez Garcia, 1994; Lachet & Bard, 1994) confirmed the methods ability to derive the fundamental frequency of resonance of the ground and they established the explanation of the H/V polarization peak by the ellipticity of the fundamental mode Rayleigh wave. Yamanka et al. (1994) and Fäh et al. (2001a) even successfully used the peak to invert for the local S-wave velocity structure.

2.2 Data and Processing

The data available was collected in three campaigns in 1995, 1999 and 2000 in spring and autumn, totaling 255 sites. In the first campaign for the qualitative microzonation (Fäh et al., 1997b) a set of 27 ambient vibration measurements has been collected in 1995 during summer (data set 1, DS1). The measurements consisted of 11 hourly recordings of 13 Minutes each, starting at 6pm with the last recording at 4am. The sensors were set in small holes so as to reduce the effect of the uppermost soil layer. Because of the high quality of the dataset, it offers an ideal opportunity to study the properties of the H/V polarization in general and the way the peaks can be interpreted.

In a second step more than 262 additional measurements were done to cover the city of Basle with a density of 500m and parts of the surrounding area with ambient vibration measurements during summer 1999 (data set 2, DS2). Primarily sites were selected where the thickness of the quaternary sediments is known

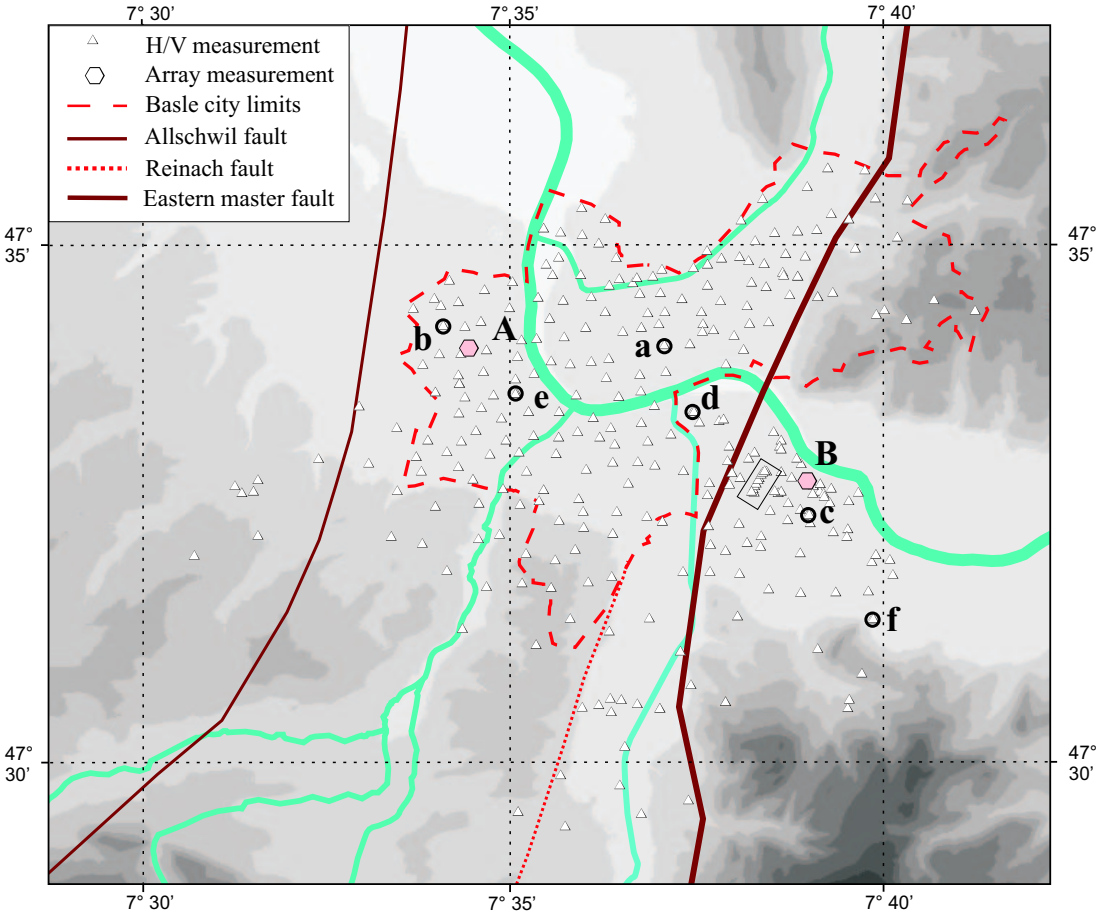

Figure 2.1: Site map for the H/V polarization survey. The topography is indicated in grey-scale steps of 50m. Letters and markers identify sites which are referred to in the text.

from boreholes. Additional measurements were made to fill gaps in the coverage. The position of the measurement sites are indicated as triangles in Fig 2.1. With the experience from the first measurements, the measurements in the second stage were done during the day for at least 15 Minutes each. The sensor was placed on soil or grassy patches where possible, otherwise on the asphalt of the sidewalk. Only 47 measurements had to be rejected, most measurements – even on sidewalks of busy major streets – could be used and interpreted, resulting in 228 sites where the fundamental frequency was determined.

As a side product of measurements with a portable small scale array, additional data from 5 synchronous measurements with 13 sensors distributed over an area of 200m diameter was available for H/V polarization analysis (data set 3, DS3). The measurements were done to derive S-wave velocities (see chapter 3). At all five sites data was recorded for 6 Minutes during daytime. While the data in DS1 and DS2 were recorded with 5s sensors, the array data was recorded with 1s sensors, so for the low frequency sites they are not applicable.

In the details of the calculations no standard exists and many different approaches are used. The frequency range of interest in our study is 0.2Hz-15Hz, limited on the lower end by the 5s Eigenperiod of the sensors used, and at the upper end by the frequency band related to building Eigenvibrations. To calculate the H/V polarization spectra, the datasets are split in time windows of 80s with an overlap of 50%. A sine square windowing function with 25% tapering tails on both ends is applied and the individual spectra are logarithmically smoothed using a boxcar window with a width of 10% of the frequency. The H/V polarization ratio for each window is formed as

$$P(f) = \frac{\sqrt{H_{EW}^2(f) + H_{NS}^2(f)}}{V(f)}, \tag{2.1}$$

where H and V denote the spectra of the horizontal and vertical components. The H/V polarization of the single windows are averaged after removal of windows with strong transient disturbances from nearby sources, identified by visual inspection.

For the representation of the polarization curve a logarithmic scale is used for the frequency and a linear scale is used for the amplitude. The reason for the logarithmic frequency scale lies in the close association of the fundamental frequency with the depth of the sediments; low frequencies are associated with deep sediments and high frequencies are associated with shallow sediments. The logarithms of the wavelength λ and of the fundamental frequency f_0 are linked through the relationship

$$\log(f_0) = \log(c) - \log(\lambda)$$

in a linear way, where c is the phase velocity. As the depth of the sediments affecting the fundamental frequency is depending on the wave length at this

frequency, the logarithmic scale is easier to interprete than a linear scale for the frequency. Fig. 2.2 illustrates this advantage further: The peaks at different frequencies are comparable in shape at a logarithmic scale, which is not the case on a linear scale.

2.3 Stability of H/V ratios

The level of ambient vibration energy has been reported to vary during the day and the year (Udwadia & Trifunac, 1973; Yamanka et al., 1993). Before the selection of the fundamental frequency of resonance f_0 from the curves we therefore had a look at the stability in time and space of the H/V polarization curves. The main questions were: How does this influence and change the polarization curve and its major peaks? How long a time series do we need to derive a time invariant polarization curve? How much do the ratios vary spatially? To answer these questions we compare results of multiple recordings at the same and adjacent sites. We look at an example from each of the three main regions of the study area, defined through the fundamental frequency ranges of 0.2-0.7Hz, 0.7-1.5Hz and frequencies higher than 1.5Hz. The locations of the sites in the comparisons are indicated by lowercase letters in Fig. 2.1.

Stability in time

The hourly recordings during the night from data set 1 (DS1) give a good indication of the short term time variation of the polarization curve. Some recordings in DS2 have been done at identical sites as in DS1 and give information on the long term variation. Fig 2.2a-c show one site from each of the general frequency categories as examples the overlayed polarization curve for the 13 Minutes recorded at 18:00, 23:00 and 4:00. The peaks are very consistent for all three peak categories. For the long term variation we considered data from recordings at the same sites with differences in the recording date of one month for Fig 2.2d, several month for Fig 2.2e and several years for Fig 2.2f.

This data indicates that one recording of approximately 15 minutes is sufficient to retrieve a time invariant H/V ratio within the limits of error inherent in the method. Neither long term nor short term variation change significantly the location of the main peak. The amplitudes of the peaks are very similar in general, but not in every case: In Fig 2.2c the polarization curve of one additional measurement with 3 years time difference is shown as thick black line. It has the same location of the main peak, but it has only about half the amplitude at the main peak compared to the other measurements at the same site. The reason for the difference might be a worse coupling to the ground or a different composition of the wave field. But the significant discrepancy in amplitude indicates that the amplitude information in the polarization curves has still to be studied in much

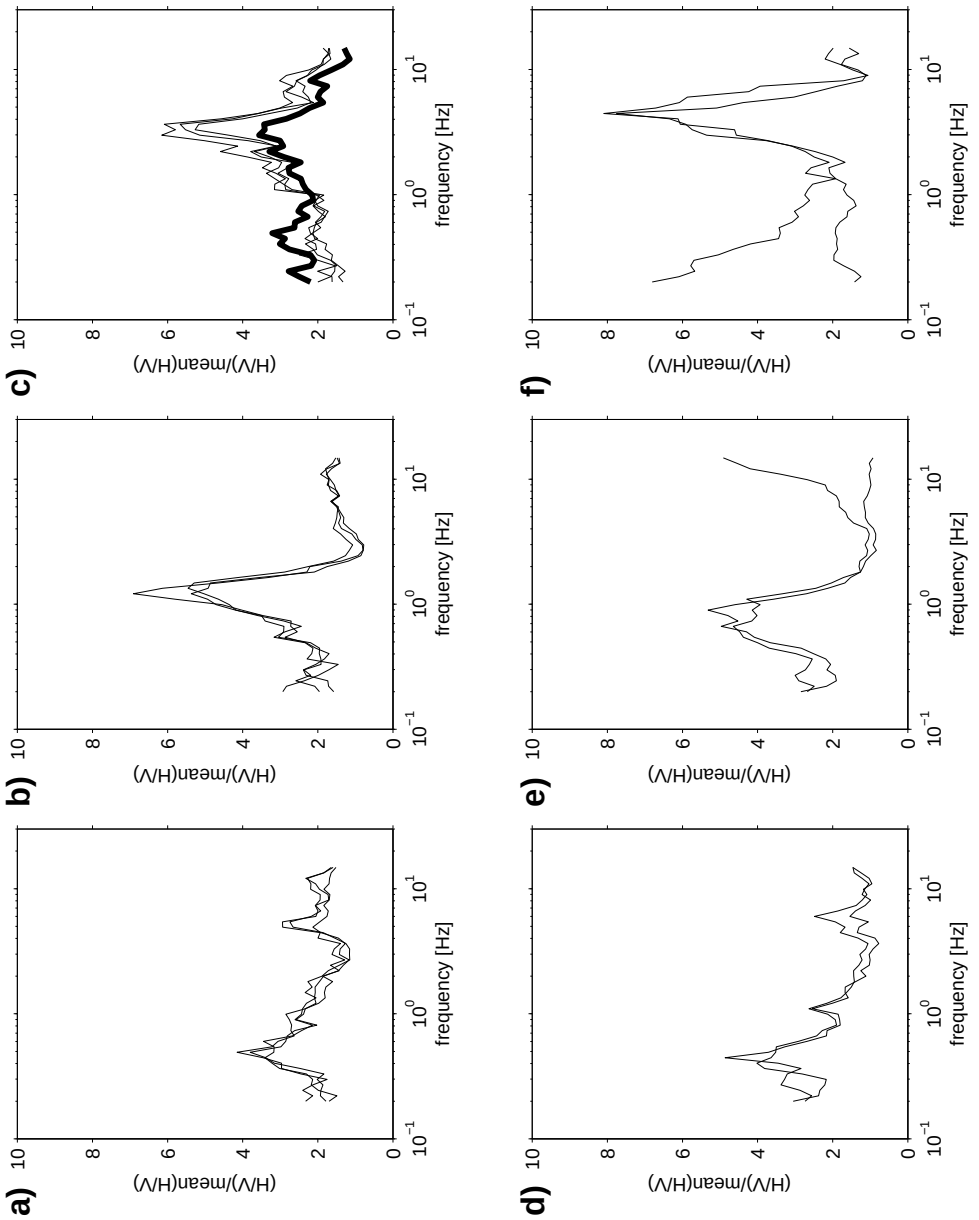

Figure 2.2: Stability in time of the H/V polarization : The figures show results from recordings at the identical site in intervals of a few hours for a-c, figure d shows recording time difference of one month, e several month and f several years. The thick line in c is also a measurement at the identical location, but with a time difference of several years; but the amplitude is much different in this recording. The lowercase letters correspond to the locations indicated in Fig. 2.1.

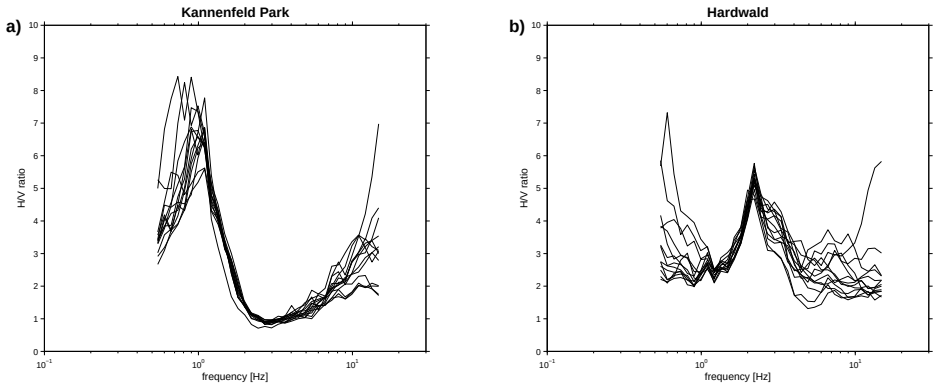

Figure 2.3: Overlay of the H/V polarization from the data of all sensors from two array measurements.

more detail before it can be used.

Stability in space

The aim of the polarization survey is a mapping of fundamental frequencies in the city of Basle. For this we have to interpolate between single measurements and we need to know how smooth the variation of the frequencies is. Fig 2.3a-b show the overlay of the polarization analysis from two array measurements from data set 3 (DS3). These are thirteen sensors well distributed within a circular area of about 200m diameter. The amplitude varies slightly, but the shape of the peaks agree very well and the location of the peak is well defined within a margin of a few percent of the frequency. We attribute the stronger variations in Fig 2.3a to the fact that the peak lies close to the Eigenperiod of the sensor (1s) used in the array. The variations aside from the main peak can be attributed to different source distances and lateral inhomogeneities.

The array in Fig 2.3a was located on a large flat meadow within a park, all sensors being positioned on equivalent material. For Fig 2.3b the array was within a forest with topographic variations of plus minus one meter. Some sensors were located on strongly compacted gravel paths, others on softer humus. This strongly supports the findings of (Fäh et al., 2001a), that the higher frequency flank of the main peak is closely related to the ellipticity of the fundamental mode Rayleigh wave and very sensitive to the surficial sediment structure.

A further experiment was conducted at a site on the Tabular Jura, where the sediment thickness is well known. The location of the test is shown in Fig. 2.1 with a box around the measurement sites. In a line of 425m length, 9 ambient vibration measurements were done. The sediment thickness varies from 13m at the beginning of the line to 15m in the middle and then increases to 40m at the

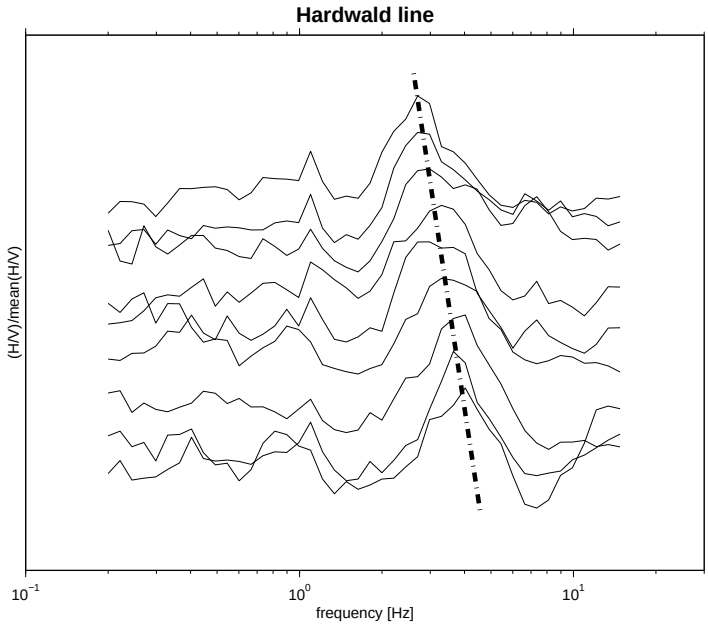

Figure 2.4: H/V polarization from 9 ambient vibration measurements along a line of 450m length.

end of the measurement line. The results are shown in Fig 2.4, the curves being shifted upwards with distance. The main peak clearly moves from 3Hz at the end of the line to 4Hz at the beginning of the line in a continuous way, as indicated by the dash dotted line. With a S-wave velocity of approximately 450m/s, the changes are continuous over a distance corresponding to 3-4 wave lengths of the waves propagating at the fundamental frequency.

We conclude that the H/V polarization curves we derived are stable in time over short term and long term variations and in space they vary continuously on a scale of the order of 500m or larger. Furthermore the H/V polarization characteristics remain qualitatively constant over daily variations and over long time spans, further supporting its link with the ground structure.

2.4 Fundamental Frequency of Resonance

The identification of f_0 from the H/V polarization main peaks is not always straight forward, as Fig. 2.2(e) can illustrate as an example. The H/V polarization main peaks are sometimes broad with a plateau on top, so the identification of f_0 is not straight forward. Fäh et al. (2001a) showed in numerical models that while the upper flank of the main peak is independent of the source distance, the lower frequency side of the peak does vary with the source distance. With increasing depth of the sediments the peak amplitude of the H/V polarization de-

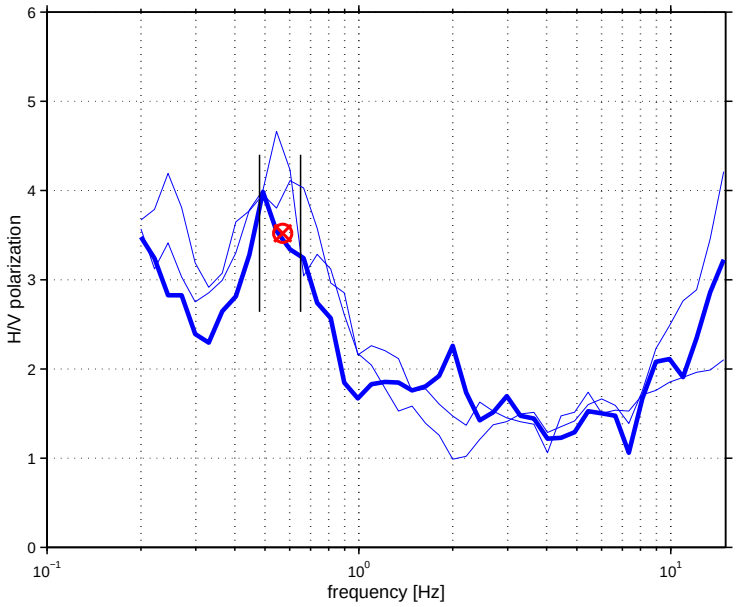

Figure 2.5: Illustration of the selection of f_0: The bold line is the curve of interest, while the thin lines show the measurements of the 2-3 closest sites. Beside f_0 (crossed circle) a range where f_0 might be selected as well is identified between the vertical lines.

creased and became difficult to identify. Furthermore are measurements within a city often contaminated with transient signals from passing cars or persons, resulting in large H/V polarization amplitudes at low frequencies. For a microzonation measurements at such sites cannot always be avoided, as major centers in a city tend to be busy all day.

Based on the results of the stability on the H/V polarization curves in time and space f_0 was selected manually with an overlay of curves from the closest neighbouring measurement sites in the background (Fig. 2.5). In this way f_0 from peaks of lower amplitude or with a broad top or tilted shape were better identifiable and the estimation of an uncertainty in the identification of f_0 was possible. For the Rhine Graben part of the city of Basle with f_0 below 1.5Hz, sediment thicknesses of at least 80m and a measurement site spacing of ca. 500m this approach worked very well. For the Tabular Jura with f_0 above 1.5Hz and sediment thicknesses of less than 40m the wave length at this frequency is much shorter and therefore the coverage was not enough for this approach at many sites. To express the uncertainty in the selection of f_0 a frequency interval was also selected to determine minimal and maximal bounds for the selection of the frequency (vertical lines in fig. 2.5). The resulting distribution of f_0 for the Basle area is shown in Fig. 2.6 with the half-width of the selected frequency range. The

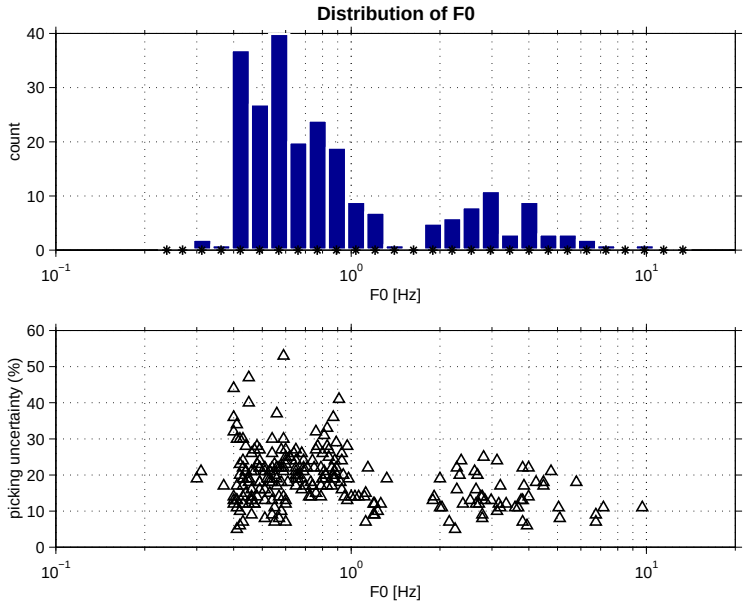

Figure 2.6: Distribution of f_0 and its uncertainty.

points inside and outside of the Rhine Graben are clearly separated at 1.5Hz. The uncertainty of the selected f_0 amounts to 15% of the frequency over the Tabular Jura and is slightly higher within the Rhine Graben. Relative uncertainty is used consistently with the logarithmic scale of the frequency. Only the area close to the Rhine with a relatively flat topography are included. Areas with significant topography were excluded as the interpretation of a H/V polarization measurement was problematic; this is explained in the next subsection. The lighter spot close to the Rhine is associated with a thicker cover of Quaternary gravels accumulated by the Rhine.

The f_0 values at each site are finally interpolated linearly and slightly smoothed, resulting in a fundamental frequency map shown in Fig. 2.7. In colour scale the fundamental frequencies are shown, overlayed with the city limits of Basle in red, the river Rhine as heavy grey line and smaller rivers as thin gray lines. Grey lines indicate the major known faults in the area. It is striking how close f_0 follows the main geologic structures. The deep Syncline of St. Jacob Tüllingen is clearly identified with low frequencies around 0.4Hz. To the west the frequencies continuously increase to 1.1Hz over the Horst of Basle, to drop down again to 0.4Hz, west of the Allschwil fault zone, where the softer material has again thicknesses of several hundreds of meters. A French study (Sebe, 1997) found similar frequencies west of the Allschwil fault zone. To the east f_0 has a clear jump at the master fault of the Rhine-Graben and increases to values above 1.5Hz. The lighter colors south of the Rhine with f_0 close to 2Hz mark an area where the Quaternary sediments have thicknesses up to 40m. Additionally the ground wa-

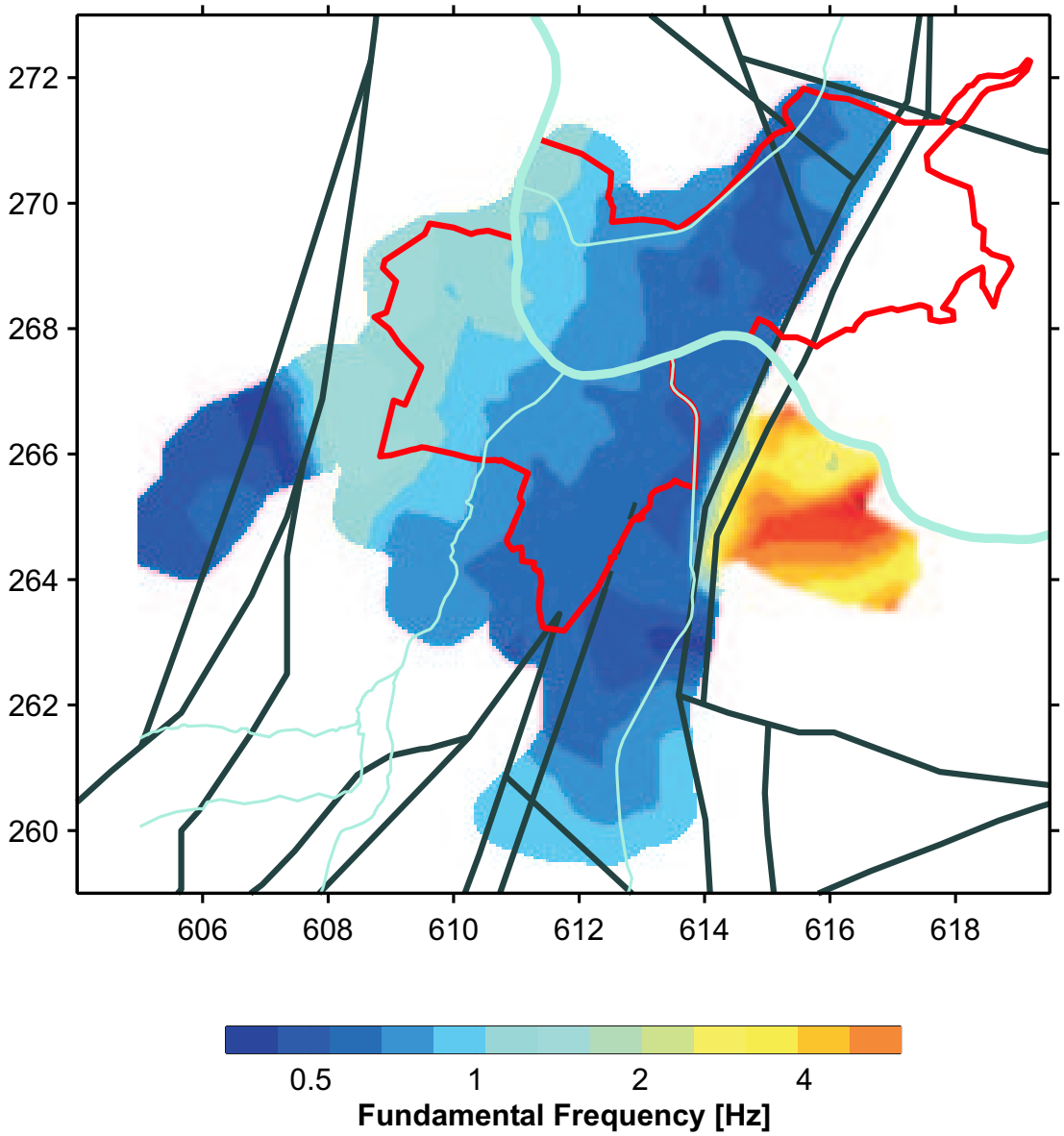

Figure 2.7: Map of fundamental frequencies in Basle. For orientation the rivers are shown in light blue and the limits of the canton of Basle in red. Grey thick lines indicate known faults in the area. The coordinates are in kilometers.

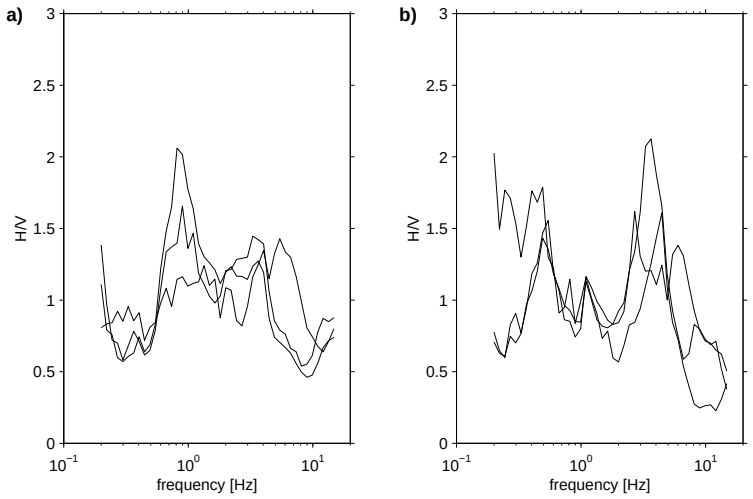

Figure 2.8: Examples of H/V measurements within strong topography. Curves from several neighbouring sites are overlain, exhibiting two distinct peaks at a lower and a higher frequency.

ter level is kept high artificially, which weakens the bedrock below and lowers the relevant seismic contrast by several meters into the bedrock. This interpretation is also confirmed by the S-wave measurement in this area (section 3.5), where an increase of the S-wave velocity was not found at the geological interface, but deeper down, inside the next geologic unit. The red areas over the Tabular Jura have known Quaternary thicknesses of 10-20m, well associated with the identified f_0.

Topography

A special case for the H/V polarization is the topography. The behavior of Rayleigh waves in rough topography is not well understood and eg. probably depending on direction. We have to expect 2D and even 3D effects. On the Tabular Jura close to the Rhine the topography is still quite flat, while the area to the north and south of the Rhine are mountainous with maximum elevations of $\approx$ 400m above the level of the Rhine. Some measurements were conducted in these areas, examples are shown in Fig. 2.8 from sites at the bottom of small valleys. The figures show overlays of measurements at different times and close by locations. Characteristic are the double peaks, one at a very low frequency and one at a higher frequency, but still too low for an association with the depth of the surface sediments. In these thin layers the Rayleigh waves would propagate parallel to the inclined surface at higher frequencies and smaller wavelength, while at larger wavelength the topography will be insignificant. The double peaks could be associated with 2D-effects, but we have no conclusive interpretation. For this

reason we excluded the topography affected sites from the data set. At the western edges of the study area several measurements on topography affected sites were retained in the data set. But the topographic variations there are small, the frequencies consistent with neighbouring sites on approximately one-dimensional sites and the wavelength associated to the fundamental frequency is much larger than the vertical variation. Therefore we retained these points. But further research is needed to interpret H/V polarization measurements from sites with strong topographic variations.

2.5 F_0 and Quaternary S-wave velocities

In the case of a single layer over a half-space, a simple formula links together f_0, the S-wave velocity (V_S) and the thickness of the soft sediment layer (h):

$$f_0 = V_S/(4h) \tag{2.2}$$

The formula actually gives the fundamental resonance of a one-dimensional body of thickness h. If two of the involved parameters are known, this formula allows the estimate of the third parameter. For the Basle region a large database of boreholes through the Quaternary is available (Noack, 1993). This data could be used in the H/V polarization survey. Most measurement sites were selected beside one of these boreholes, offering the opportunity to test the use of this formula to estimate S-wave velocities from the knowledge of the sediment depth and f_0. The sites have been differentiated from the geological borehole information into four general site classes (Fäh et al., 1997b), also available from the database. In the same study S-wave velocities were derived for these site classes from SPT measurements.

In a first step sites from the Tabular Jura were selected, where the bedrock beneath the Quaternary sediments consisted of Mesozoic rock. The S-wave velocity contrast should be very high and the H/V polarization should therefore have a clear first peak caused by this contrast. From the four site classes normal gravel, sandy gravel, calcified gravel and artificial fill, the first three classes were sampled. In Figure 2.9 the fundamental frequency derived from the H/V polarization peak is plotted versus the thickness of the quaternary sediments on a logarithmic scale, differentiated for the site classifications (crosses and filled symbols). Dotted lines indicate constant velocities, in steps of 100m/s. A dash dotted and a continuous line indicate where the estimates resulting from formula (2.2) should cluster, if they were to agree with values in Fäh et al. (1997b) determined from SPT measurements. The values are too widely distributed to allow a derivation of an S-wave velocity for the site classes. A finer differentiation of the Mesozoic sediments does not alter the result.

The reason for the failure of the formula to derive S-wave velocities is twofold. Firstly the geological classification of the whole sediment column into one site

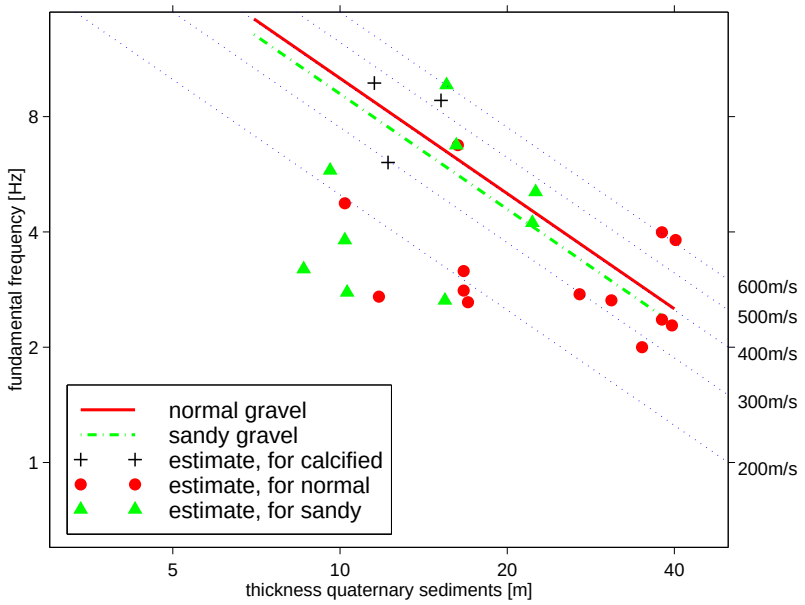

Figure 2.9: Estimates of V_S from f_0 and the thickness of the soft sediments. Only sites where the geology identifies stiff Mesozoic material below the Quaternary sediments are shown.

class might not be correlated with the average S-wave velocity appropriate for the sediment column. This would result in a large variation of velocity estimates for a single sediment class. But the very large bandwidth of less than 200m/s up to 600m/s cannot be explained in this way. The second explanation is that the geological contrast identified in the borehole is not the seismically relevant contrast. The sites shown here all have a relatively high ground water table. The ground water and weathering of the bedrock material have probably weakened the first few meters of the bedrock, which explains the extremely low velocities. An experiment with an array technique and an S-wave reflection line in the same area confirmed this explanation (chapter 3): The S-wave velocity contrast was at least 10m lower than where it would have been assumed from the geologic information.

Secondary H/V polarization peaks

In the evaluation of the fundamental frequency for measurement sites within the Rhine-Graben an interesting feature of the H/V polarization curve appeared: At some sites a second significant and clearly identifiable peak is visible at higher frequencies (Fig. 2.10). Such peaks were found at 69 of 178 sites in the Rhine-Graben. The lower part of Fig. 2.11 shows the location these sites marked as

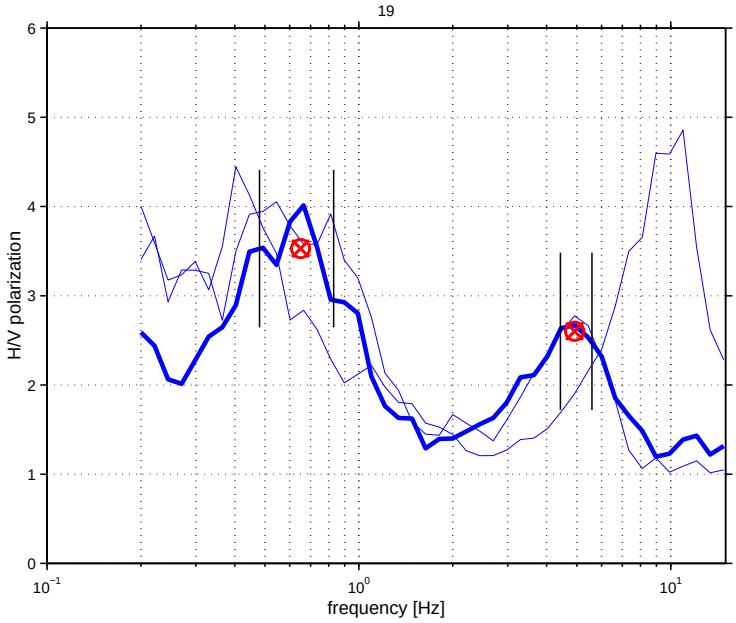

Figure 2.10: Example of a H/V polarization curve with two peaks, the first one associated with the deep soft material, while the second is probably associated with the thickness of the Quaternary sediments.

crosses, circles indicate sites where the primary peak could be assigned to the Quaternary sediments. As formula (2.2) is valid for the fundamental resonance frequency of a 1D homogeneous body, it is reasonable to use it for the same kind of S-wave velocity estimate as in the previous section, but this time for the secondary peak. The largest concentration of crosses on the location sketch in Fig. 2.11 is in the "Lange Erlen" and "Bäumlihof" area in Basle, consisting of a few square kilometers of fields and forest. As this is a drinking water protection are, traffic is very low and sources are at least at a distance in the order of a few hundreds of meters.

In Fig. 2.11 f_0 is plotted versus the thickness of the Quaternary sediments, crosses marking the points from the Rhine-Graben and circles marking the points from the Tabular Jura, already shown in Fig. 2.9. The scatter of the points is similar to the points from the Tabular Jura, but the estimated S-wave values are actually higher. The average S-wave velocity of the Quaternary sediments in region of Basle is between 400m/s and 500m/s as array measurements from five sites in Basle show (chapter 3). Although the estimates from the Rhine-Graben do not allow the clear determination of the S-wave velocity, their scatter is similar or even smaller than the scatter from the points over the Tabular Jura. We conclude that the frequency of these secondary peaks of the H/V polarization curve can reasonably be associated with the Quaternary sediments in the Rhine-Graben.

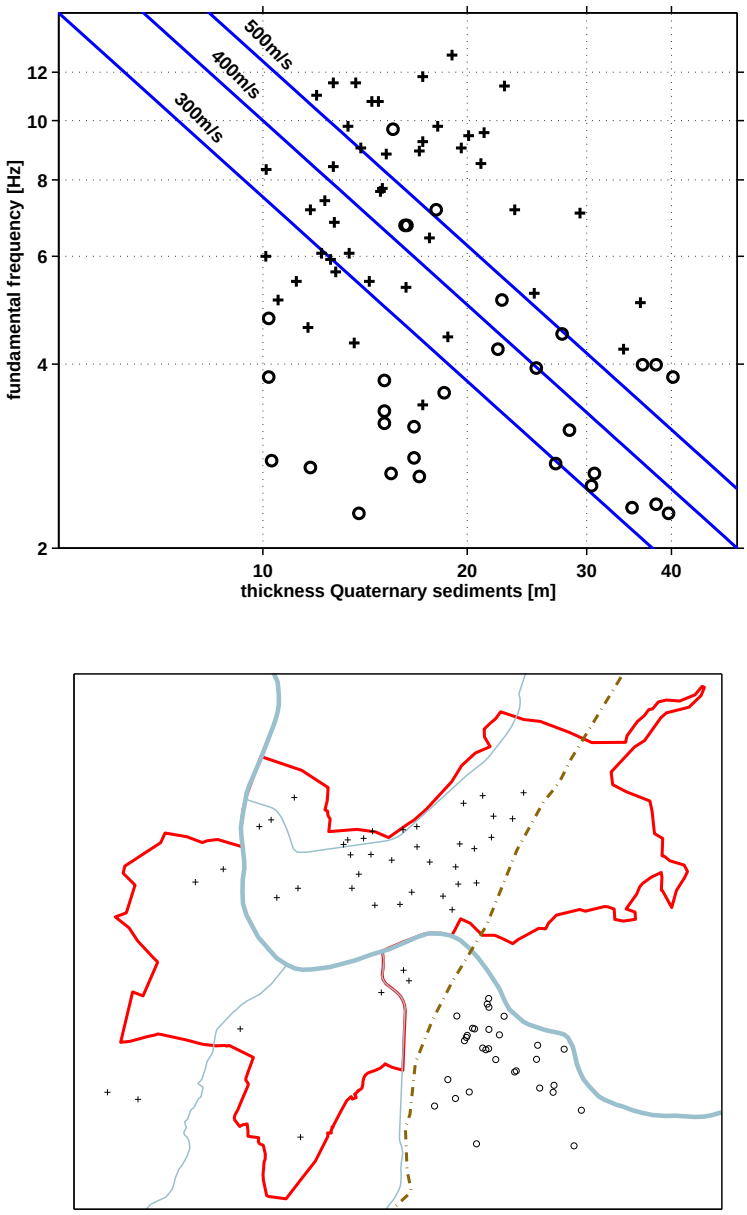

Figure 2.11: Comparison of sediment thickness vs. the center frequency of the peak that is probably associated with the Quaternary sediments and a sketch of their location. Values and locations with frequencies selected from a primary peak are marked with circles, while sites and frequencies from a secondary peak are marked with crosses. Only sites with at least 10m of Quaternary sediments are used.

2.6 Conclusions

A very detailed study of f_0 in the area of Basle is presented. The f_0 map is an important contribution as well to the understanding of the geological and geophysical structure of the area as to future earthquake hazard microzonation studies for the area. The variability in time and space of f_0 has been studied and verified that the H/V polarization gives reliable results. Measurements at any daytime and on any ground surface proved to be possible, provided there are more measurements in the close neighbourhood. The high density of measurements in the survey allowed for an increased reliability in the identification, but the uncertainty in f_0 remain at 15% in most cases.

The estimation of S-wave velocities from f_0 proved to be not reliable in the area of Basle, mainly because of high ground water levels weakening the bedrock surface. The attempt showed that the geological depth of the bedrock can significantly deviate from the S-wave velocity contrast responsible for the H/V polarization .

Chapter 3

Application of an array technique to ambient vibrations

Accepted for publication by GJI

Abstract

The S-wave velocity is a very important factor in local hazard assessment. The direct measurement with conventional methods is very costly, therefore inexpensive and efficient methods are needed to make local hazard assessment better feasible. Techniques based on the analysis of ambient vibration recordings from small scale arrays of sensors have become popular recently. One technique that is favoured by several research groups is the extraction of the dispersion curve by estimation of the f-$\mathbf{k}$-spectrum and its inversion for the S-wave velocity structure. This technique is very inexpensive, gives information well into the bedrock and it is applicable to seismically noisy sites, where conventional seismic techniques are difficult or impossible to apply. We compare the properties of sensor configurations used in different studies and show their respective advantages and disadvantages for the f-k-spectrum estimation. At synthetic data we illustrate the applicability and some technical aspects of the method. Results from a test measurement show very good agreement with S-wave seismic data and the geologic information for the test site.

3.1 Introduction

For the estimation of the local site response in an earthquake the shear wave velocity is an important parameter, on which ground motion amplification and soil liquefaction predictions are mainly based. However there is a lack of reliable economic methods to determine this velocity. For S-wave reflection seismics it is difficult to generate sufficient energy that penetrates to larger depths and in the analysis of data the discrimination of P-wave and S-wave information is quite complex. Vertical seismic profiling or similar borehole seismics are better

established, but they are very expensive in application. An additional drawback of seismic methods is the high frequency range of the generated and measured waves, which is much higher then the range of interest in site-effect determination. An alternative to the expensive seismic techniques is the derivation of S-wave velocities from ambient vibrations measured on an array of geophones.

Ambient vibrations are composed mainly of surface waves, often dominated on the vertical component by the fundamental mode Rayleigh wave. But the composition of the wave field is quite complex as multiple wavelets are coming from all directions at the same time. By extracting the dispersion of the surface waves and inverting it for the S-wave velocity structure, just exactly the data needed for the determination of local site effects at the frequencies of interest can be derived. The analysis of microtremor data for surface wave dispersion is an idea that occupied seismologists already for a long time. Eg. Ramirez (1940) made experiments with a tripartite array or Toksöz (1964) experimented with this concept. The critical point is the extraction of the surface wave dispersion, while for the inversion one of the multiple established methods can be used. We apply the f-$\mathbf{k}$-spectrum estimation technique developed by Capon (1969) during the sixties at the LASA wide aperture array. In the studies of Asten & Henstridge (1984), Horike (1985) and Matsushima & Okada (1990) the technique was applied successfully to ambient vibrations and S-wave velocity structures could be derived. Succeeding works like Milana et al. (1996), Kawase et al. (1998) or Liu et al. (2000) also reported good results. The advantages of the technique are that it is not invasive and uses passive sources, which makes it very inexpensive, that it penetrates to depth well below the usual 20-30m of boreholes and that is applicable at sites where the level of ambient vibrations prohibit seismic techniques. Therefore a further development of the method to allow routine application is very desirable.

With this paper we want to contribute to some methodological aspects of this technique, so as to make it easier in application. First we study the array configuration and how it influences the wavenumber resolution. Then we compare different configurations that have been used for their advantages and disadvantages. Furthermore we perform synthetic tests to validate the technique and improve the processing procedure. Finally we show the results from an experimental measurement done at a calibrated site in Switzerland, to show how the relevant S-wave velocity information for local site effect determination can be derived in a simple and cost efficient way.

3.2 Theory

F-k-spectrum

The wave field $W(x, y, t)$ of seismic ground motion can be represented through a Fourier Transform of time and space as a frequency-wavenumber spectral density function (f-**k**-spectrum, $P(f, \mathbf{k})$). The value of the spectrum for a point $(f_0, \mathbf{k}_0)$ in the f-**k**-space corresponds to the energy in the wave field of the plane wave with frequency f_0 and wavenumber $\mathbf{k}_0$. The dominant modes of wave propagation show up as local maxima in the spectrum, so that phase velocities can be extracted and the dispersion curves of these modes can be built.

High-resolution beamforming (HRBF) uses the cross power spectral densities of an array of sensors to estimate the f-**k**-spectrum, refining it with coherency estimates. It is applicable if the wave field can be reasonably approximated as superposition of plane waves for the frequencies and phase velocities of interest. This implies that the resolvable signals have sources at distances an order of magnitude larger than the array aperture and that the local structure can be approximated with horizontal homogeneous layers. The useful signals for this method are dispersed and coherent over the array area, while non coherent and not dispersed signals act as noise in the determination of surface wave dispersion.

f-k-spectrum estimation

In the following we summarize the basic concept of the high-resolution beamforming (HRBF) method. For details of the calculations we refer to Capon (1969). In the HRBF the output of an array of p seismic sensors at positions $\mathbf{r}_j$, $(j = 1 \dots p)$ is recorded. The estimation $\hat{P}(f, \mathbf{k})$ of the true f-**k**-spectrum $P(f, \mathbf{k})$ is calculated as

$$\hat{P}(f, \mathbf{k}) = \left[\sum_{j=1}^{p} \sum_{l=1}^{p} q_{jl}(f) \exp(i\mathbf{k} \cdot (\mathbf{r}_j - \mathbf{r}_l)) \right]^{-1} \tag{3.1}$$

where $q_{jl}(f)$ are the elements of the inverse of the complex coherency matrix for sensors j and l. If the time length of the signals used for the estimation of the coherency matrix is large enough, the statistical expectancy value of the estimate $\hat{P}(f, \mathbf{k})$ of the f-**k**-spectrum is the convolution of the true f-**k**-spectrum $P(f, \mathbf{k})$ with a frequency window W_f and a wavenumber window $W_\mathbf{k}$, scaled with

a constant C:

$$\hat{P}(f_0, \mathbf{k}_0) = C \int_{\mathbb{R}^2} \int_{-\pi}^{-\pi} P(f, \mathbf{k}) W_{\mathbf{k}}(\mathbf{k}, \mathbf{k}_0, f_0) W_f(f - f_0) \frac{df}{2\pi} d\mathbf{k} \quad (3.2)$$

$$W_{\mathbf{k}}(\mathbf{k}, \mathbf{k}_0, f_0) = \left| \sum_{j=1}^{p} A_j(\mathbf{k}_0, f_0) \exp(i(\mathbf{k} - \mathbf{k}_0) \cdot \mathbf{r}_j) \right|^2$$

$$= \sum_{j=1}^{p} \sum_{l=1}^{p} A_j(\mathbf{k}_0, f_0) A_l(\mathbf{k}_0, f_0) \cos((\mathbf{k} - \mathbf{k}_0) \cdot (\mathbf{r}_j - \mathbf{r}_l)) \quad (3.3)$$

The frequency window $W_f(f)$ is the transfer function of the tapering function applied to the signal time windows; its shape can be controlled by choosing an appropriate window length and function. The definition of the wavenumber window $W_{\mathbf{k}}(\mathbf{k}, \mathbf{k}_0, f_0)$ is given in equation (3.3). The wavenumber response is defined through the array configuration (terms $\cos((\mathbf{k} - \mathbf{k}_0) \cdot (\mathbf{r}_j - \mathbf{r}_l))$) and it is modified with weights $A_j(\mathbf{k}_0, f_0)$. The weights are derived from the signal and represent a maximum likelihood filter suppressing the power of all waves traveling at other wavenumbers and frequencies than $(f_0, \mathbf{k}_0)$, but let pass undistorted all plane waves with these parameters. From equation (3.2) we see that the closer $W_{\mathbf{k}}$ approximates a Delta function, the better is the estimate of the f-$\mathbf{k}$-spectrum.

By setting the weights A_j in equation (3.3) constant to 1/p and $\mathbf{k}_0 = 0$, we get the beampattern $B(\mathbf{k})$ of the array configuration:

$$B(\mathbf{k}) = \frac{1}{p^2} \sum_{j=1}^{p} \sum_{l=1}^{p} \cos(\mathbf{k} \cdot (\mathbf{r}_j - \mathbf{r}_l)) \quad (3.4)$$

The beampattern is the wavenumber response of the regular beamforming technique. The improvement in the high-resolution estimator works in the following way: Where coherent signals are present in the wave field, the weights A_j are large and the full energy of the signal is passed to the f-$\mathbf{k}$-spectrum. If the coherency is low, the weights A_j are small and therefore the energy passed to the spectrum is reduced. The result is an effective reduction of the smearing of local maxima in the f-$\mathbf{k}$-spectrum caused by the finite width of the wavenumber window.

Any coherent signal can be resolved by the estimator. This implies for our application that a significant content of body waves - which are coherent on the array - can increase the coherency at frequencies and wavenumbers not corresponding to the surface waves and thereby deteriorate the determination of surface wave dispersion.

Accuracy and Resolution

For a wave field composed of an arbitrary number of uncorrelated signals and a low level of incoherent noise, the accuracy of the HRBF can be arbitrarily high

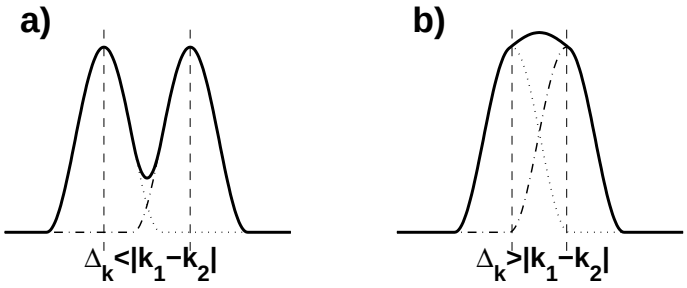

Figure 3.1: Spectral power in the wave field against wavenumber at a fix frequency for two waves traveling with wavenumbers $\mathbf{k}_1$ and $\mathbf{k}_2$. In (a) the wavenumber difference is large enough for both wavenumbers to be resolved. In (b) the difference is to small and a single wrong wavenumber is interpreted.

(Woods & Lintz, 1973; Asten & Henstridge, 1984). But there is a number of possible sources of error that have to be considered and that influence the choice of parameters in an experiment.

Firstly the ambient vibration wave field is composed of an unknown and possibly very large number of signals. Correlated signals coming from several directions can form an elongated peak at the center of gravity of the different wavenumbers involved in the two-dimensional wavenumber space (Woods & Lintz, 1973). This suggests the use of short time windows, such that multiple signals are less likely.

Secondly the width of the wavenumber window $W_{\mathbf{k}}$ (3.3) limits the resolution of two signals with a small wavenumber difference. The problem is illustrated in Fig. 3.1. We assume a wave field of two plane waves with frequency f_0 and wavenumbers $\mathbf{k}_1$ $\mathbf{k}_2$, having only a small difference $d\mathbf{k} = |\mathbf{k}_1 - \mathbf{k}_2|$. We display in Fig. 3.1 spectral power versus wavenumber. If $d\mathbf{k}$ is larger than some critical value $\Delta_{\mathbf{k}}$, both wavenumbers show up as peaks in the spectrum (Fig. 3.1a). If $d\mathbf{k}$ is smaller than $\Delta_{\mathbf{k}}$, the two peaks merge into one single peak and an intermediate wrong value is evaluated (Fig. 3.1b). The lowest wavenumber that can be resolved is $\Delta_{\mathbf{k}}/2$. For smaller wavenumbers the peaks from different directions might merge. So the width of the wavenumber window limits the resolution of multiple wavenumbers and also the lower end of wavenumbers that can be resolved.

Thirdly the method is very sensitive to mismatch in the steering beam (Cox, 1973). In the HRBF the f-$\mathbf{k}$-spectrum is calculated for a selected grid of wavenumbers (steering beams). If the noise level in the wave field is low, then the wavenumber resolution of the HRBF will be very high and therefore a dense sampling in the wavenumber domain is needed in the calculation of the f-$\mathbf{k}$-spectrum. Care has to be taken to sample the wavenumber domain sufficiently dense, so as to detect all peaks correctly. For all three possible sources of error

a good knowledge of the wavenumber response (3.3) of the HRBF is important, which is largely defined through the array configuration.

3.3 Array configuration

As the wavenumber response $W_{\mathbf{k}}$ (3.3) of the HRBF is depending on the recorded data itself, it cannot be studied theoretically. The classical way to look at this problem is to consider the signal dependent weights in $W_{\mathbf{k}}$ as an improvement of the beampattern defined through the array configuration and to study the beampattern (3.4) instead. The resolution capability $\Delta_{\mathbf{k}\,\mathrm{beam}}$ of the beampattern can be regarded as a lower limit of the resolution capability of the method. For the resolution capability $\Delta_{\mathbf{k}}$ of the HRBF, factors of improvement of three to six ($\Delta_{\mathbf{k}} \approx \Delta_{\mathbf{k}\,\mathrm{beam}}/3$) have been observed by Asten & Henstridge (1984) and Horike (1985).

In the different applications of the HRBF to ambient vibrations, a number of configurations have been used, such as regularly spaced crosses and L-shapes (Horike, 1985), irregularly spaced crosses (Asten & Henstridge, 1984; Milana et al., 1996) or regular configurations based on triangles (Kawase et al., 1998; Liu et al., 2000). Typical configurations and the corresponding beampatterns are shown in Fig. 3.3. The properties of array configurations have been extensively studied for the nuclear test ban treaty control theoretically and in practical applications (Carpenter, 1965; Haubrich, 1968). The purpose of these arrays is the detection of regional and teleseismic events and the improvement of the gain in signal to noise ratio for these phases. For the regional seismic arrays like NORESS or GERESS, a configuration of 25 sensors arranged in concentric circles has been used, which optimally suppresses the local noise through a minimum sensor spacing larger than the coherency distance of the local noise (Mykkeltveit, 1985; Harjes, 1990).

In the analysis of ambient vibrations the signals of interest are the local "noise" sources and therefore the minimum sensor spacing of the regional seismic systems actually gives a maximum aperture for the array configuration. The main focus is on detailed resolution of the wavenumber spectrum and for this purpose a sharp mainlobe and a low background level in the wavenumber window $W_{\mathbf{k}}$ are necessary. The array configuration influences these properties through the beampattern (3.4). Barber (1959) and Haubrich (1968) show ways how the beampattern can be understood and optimized; results we make use of.

Beampattern

The beampattern (3.4) of an array of sensors is formed as the sum of cosine functions with a periodicity defined through the distances between to sensors $\mathbf{r}_j - \mathbf{r}_l$. All combinations of the sensors are used. In equation (3.4) we rewrite

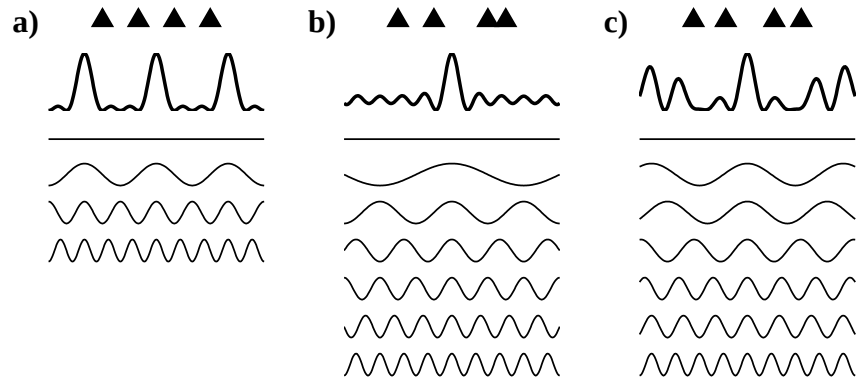

Figure 3.2: Examples of beampatterns for (a) a regular and (b,c) two irregular array configuration. They are composed as weighted sums of cosine functions with periods inversely proportional to the distances between pairs of sensors $P_{\mathbf{k}} = 2\pi / |r_j - r_l|$.

the wavenumber as $\mathbf{k} = k\,\mathbf{e_k}$, where $\mathbf{e_k}$ is the unit directional vector of the wavenumber and k is the wavenumber value. For a given direction $\mathbf{e_k}$ the periods of the cosine functions then become $2\pi/(\mathbf{e_k} \cdot (\mathbf{r}_j - \mathbf{r}_l))$. So the beampattern problem of a real two-dimensional array is reduced for each direction to the beampattern of a one-dimensional line array.

In Fig. 3.2 the compositions of the beampatterns for three line array configurations of four sensors are shown. In the first line we show the sensor positions, in the second line the beampattern for the array and below the separate contributing cosine functions. The largest distance between two sensors - the array aperture - contributes the shortest cosine period and therefore defines the width of the peak of the beampattern (last line); the shortest inter sensor distance defines the period of the repetition of the pattern, the wavenumber aliasing period (Fig. 3.2a). Between the main peaks of the aliasing pattern, the maxima and minima of the contributing cosines cancel each other out more or less effectively.

The important aspect of the configuration is therefore not the position of the sensors themselves but the vector distances that are formed through each pair of two sensors in the array. Haubrich (1968) called this set of vectors the *coarray* of the configuration. Irregular arrays with just a few sensors can produce the same coarray as a regular array with an even sensor distribution. With a limited amount of sensors an irregular configuration can combine a large aperture for a sharp main peak and with small inter-sensor distances for large aliasing periods. Two examples of irregular line arrays are given in Fig. 3.2(b)/(c). In (b) the third sensor is moved half a sensor distance to the right compared to the configuration in (a), while in (c) the middle two positions are randomly selected. Because the distances between sensors are multiples of the shortest distance in example (b), the beampattern has mainly changed to a larger aliasing period by a factor of two

Table 3.1: Beampattern properties of the configurations in Fig. 3.3

config.	$\Delta_{\mathbf{k}\,\mathrm{beam}}$ [rad/m]	P_{alias} [rad/m]	background [db]
A	0.018	0.17	-13
B	0.018	> 0.2	-11.1
C	0.021	> 0.2	-11.2
D	0.014	0.12	-13.6
E	0.018	0.14	-12.8

and a slightly higher background level. In example (c) the actual aliasing period is increased as well, but high side lobes appear. A flat background response is desirable, so that aliasing from side lobes can be clearly identified, if they occur.

We conclude that an irregular array configuration based on multiples of a minimal distance give the best combination of low background level and large spatial aliasing periods. Haubrich (1968) called this kind of arrays isometric and most of his optimized configurations were very close to isometric.

Comparison of array configurations

We compare configurations used in previous investigations and two theoretical configurations (Fig. 3.3). For better comparison we use all configurations with the same number of sensors and with a size that fits within a square of a fixed side-length. We preferred this constraint to a normalization of the maximum aperture, as it is easier to apply when setting up an experiment. For each configuration we show on the right the beampattern as contours in Decibel.

Three values are used to quantify the quality of the beampattern. Following Woods & Lintz (1973) we extract the maximum radius of the -3db contour from the beampattern as a measure for the width of the main peak and therefore as the criterion for the resolution $\Delta_{\mathbf{k}\,\mathrm{beam}}$. We choose the wavenumber distance to the closest side lobe with a level of at least -3db of the main peak as a measure for the aliasing period (P_{alias}). To quantify the background level in the beampattern, we calculate the mean value of the beampattern in the ring $\Delta_{\mathbf{k}} < |\mathbf{k}| < P_{alias}$. These values are given in Table 3.1.

The rectangular configurations in Fig. 3.3 are less isotropic compared to the other configurations. This is caused by the projections of many sensors on the same point for the azimuth along the axis of the cross or L. The beampatterns of the triangular and circular shapes are more symmetrical, but they also have high side lobes distributed symmetrically. If the azimuth of the strong noise sources is known, the rectangular configurations with the directionally well defined side lobes allow for a good analysis. But if the sources are unknown, a symmetrical distribution of distant side lobes and low background level are better.

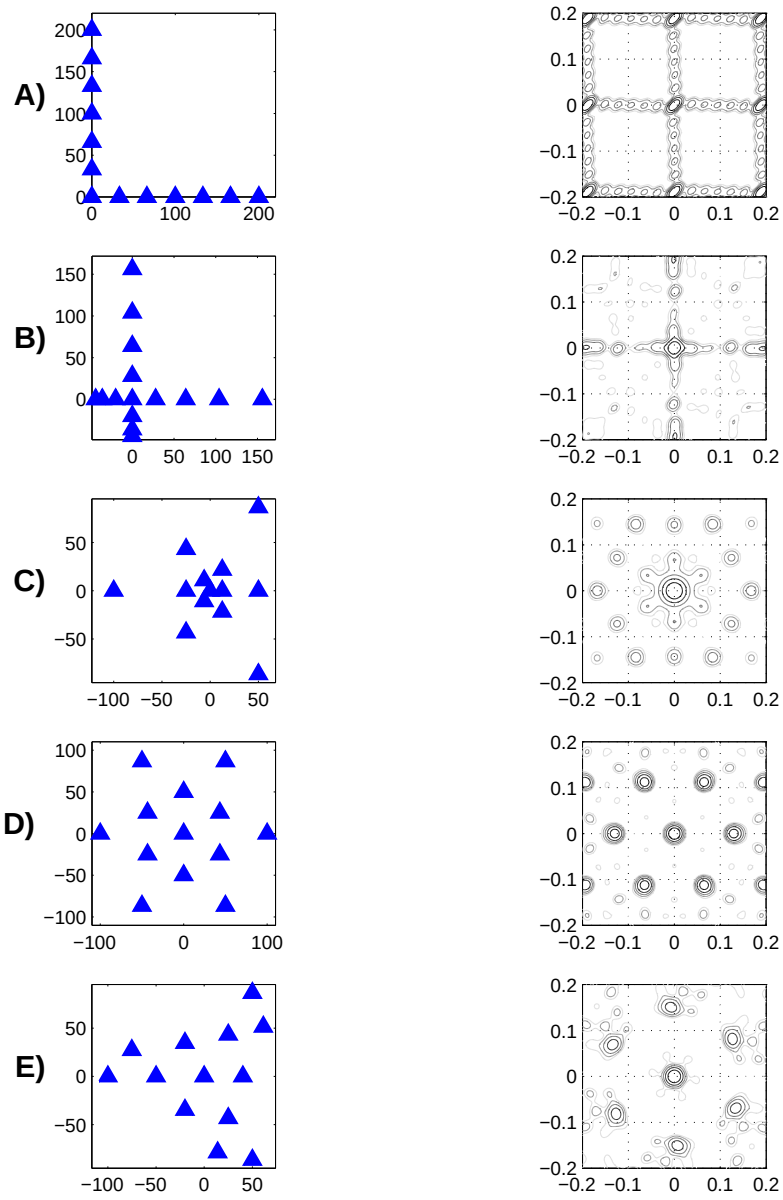

Figure 3.3: Array configurations and their beampatterns. A) is comparable to one of the configurations in Horike (1985), B) is comparable to Milana et al. (1996), C) to Liu et al. (2000). D) adopts the recommendations of concentric circles for regional seismic arrays and E) is a configuration found with a heuristic optimisation of a configuration of four concentric circles with three sensors each. The beampattern contours are drawn in decibel down from the maximum.

The comparison of the values in Table 3.1 shows that the advantages of a low background level usually trade off with a shorter aliasing period. Configuration D excels in the sharpness of the main peak and the lowest background pattern, while its aliasing period is the shortest of the five configurations considered. Configuration C has a very good aliasing period, because of the short distances involved, but the main peak is the widest of the five configurations and the background level is relatively high.

The comparison of the configurations in Fig. 3.3 indicates that there is not one best configuration, but each configuration has some small advantages and disadvantages over the others. We conclude from this comparison that the important aspect when choosing a configuration is that a wide spectrum of vector distances between the sensors is generated (large coarray), which can be achieved with a multitude of configurations. The choice of the configuration needs to take into account the conditions at the local site of an experiment and possibly the knowledge about the azimuth of strong sources of ambient vibrations. Because of their symmetry configurations C, D and E are better suited for general applications than A and B, while configuration E shows the best compromise between aliasing, width of the main peak and background level, so we chose configuration E for our test measurement. However the differences are too small to exclude any of the five configurations from applications.

3.4 Synthetic tests

To validate the HRBF technique we perform a test with synthetic data. We generate realistic synthetic ambient vibrations, using a finite difference (Fäh, 1992), an algorithm of second order accuracy and numerically stable for materials with normal as well as high Poisson's ratio. Fig. 3.4 describes the structural model and the scheme for generating ambient vibrations. Point sources are located randomly in a zone close to the left boundary of the finite difference grid, with depth down to 50m, to include possible conversions of wave types at lateral inhomogeneities and at layer interfaces. The configuration of the sensors is a regularly spaced line array with 8 sensors and a sensor spacing of 50m. Uncorrelated white noise was superposed at each sensor with the same spectral content as the FD-signal to simulate realistic noise conditions.

Fig. 3.5(a) shows the frequency-phase velocity-diagram of the analysis of the synthetic wave field. The second panel (Fig. 3.5b) displays the theoretical dispersion curves of the fundamental and the next higher Rayleigh mode of the structure as solid lines and some aliases of these curves as dashed lines. The spectrum of the vertical component at one of the two central receivers in the array is given in Fig. 3.5(c). The fundamental frequency of resonance of the structure is at 3Hz, which is reflected in the high energy peak at this frequency. Below 2Hz only a small amount of energy is present due to the size and depth

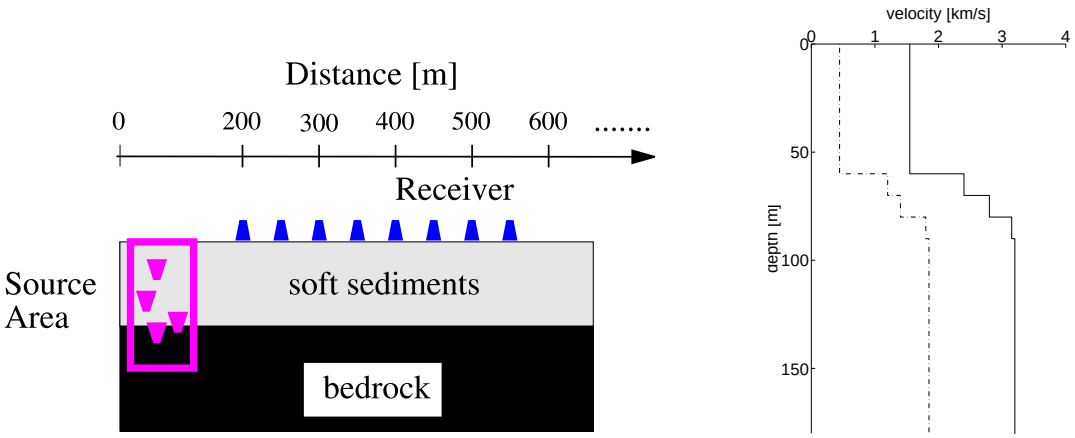

Figure 3.4: Model for the generation of synthetic ambient vibrations and the velocity structure modelled. The structure is one-dimensional and consists of 60m of soft sediments overlaying bedrock. The density is $1.8kg/m^3$ in the sediments, $2.4kg/m^3$ in the bedrock; Q_S is kept constant at 100, while Q_P changes from 200 in the sediments to 250 in the bedrock.

of the sources. The fundamental mode dispersion curve is clearly resolved in the range of 2-8Hz, whereas at higher frequencies the aliases interfere with the dispersion curve and the multiplicity of peaks makes the identification of the correct curve very difficult. In the range of 6-8Hz also the dispersion of the second higher mode Rayleigh wave is seen (Fig. 3.5a).

The resolution limit $\Delta_{\mathbf{k}} = \Delta_{\mathbf{k}\,\mathrm{beam}}/3$ defined through the beampattern is indicated with a dash-dotted line in Figs. 3.5(a) and (b), assuming an improvement of a factor of three from the beampattern by the HRBF. The dotted line delineates the limit $\Delta_{\mathbf{k}\,\mathrm{beam}}$ from the beampattern alone. The smearing towards higher velocities at 2Hz already indicates the influence of the lower resolution boundary, but the actual limit here is the energy content in the signal. The width of the main lobe of the beampattern of the line array is 0.018 rad/m. Following Asten & Henstridge (1984) or Horike (1985) in assuming a factor three for the improvement through the HRBF, we get a resolution of $\Delta_{\mathbf{k}} = 0.006\,\mathrm{rad/m}$. The smallest wavenumber that can be resolved in this case is $\Delta_{\mathbf{k}}/2 = 0.003\,\mathrm{rad/m}$ corresponding to a phase velocity of approximately 4000m/s at 2Hz. The test illustrates the capability of the HRBF to resolve the dispersion of the fundamental mode Rayleigh wave from ambient vibrations, and the type of signals and problems to be encountered with real data.

The increasing width of the peaks at low frequency illustrates the inverse proportionality of wavenumber and phase velocity. Although the peaks in the

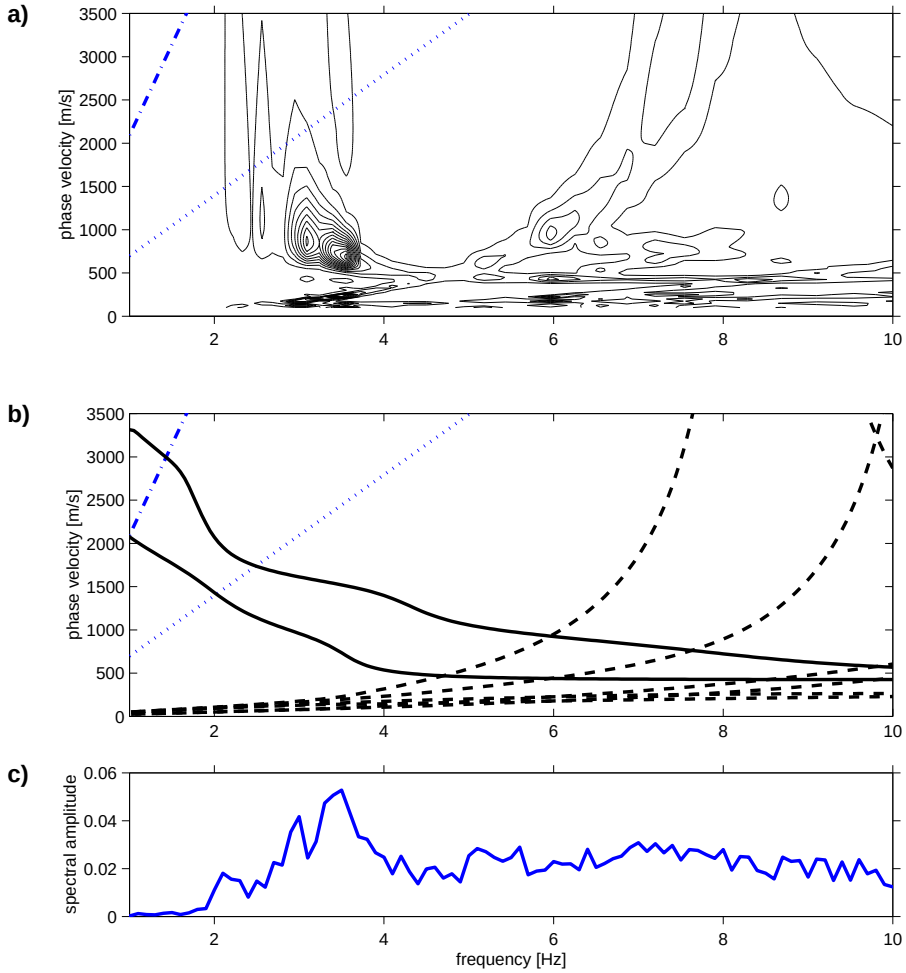

Figure 3.5: Analysis of synthetic data with HRBF: (a) contours of the f-**k**-spectrum, (b) the theoretical dispersion curves of the fundamental and first higher Rayleigh mode of the modelled structure as solid lines and some of their aliases as dashed lines, (c) representative spectrum of the vertical component at one of the two central receivers. The dotted line in (a) and (b) indicates the limit of the resolution as defined by the beampattern, whereas the dash-dotted line delineates the actually expected limit for the HRBF.

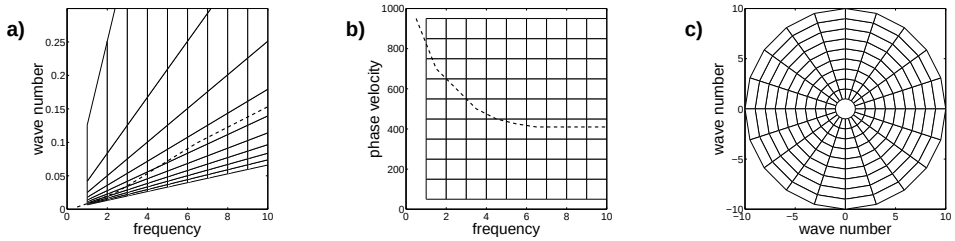

Figure 3.6: Illustration of the velocity defined wave number resolution. A regularly spaced sampling in the phase velocity domain (b) results in an a wavenumber sampling with variable spacing (a), with high resolution where it is required. For the two-dimensional wave number sampling a polar grid allows to use this kind of sampling in an efficient way (c). The dashed line represents the dispersion curve.

wavenumber domain have a fixed width, the corresponding range of phase velocities is frequency dependent ($c = 2\pi f / |\mathbf{k}|$) and therefore increases with low frequencies. This implies that a frequency dependent wavenumber sampling of the f-$\mathbf{k}$-spectrum should be used to achieve a good phase velocity resolution. We tested several schemes for sampling the f-$\mathbf{k}$-spectrum and found that a wavenumber sampling defined through the velocity range that should be resolved is optimal. Fig. 3.6 illustrates the concept. To make this scheme applicable, the two-dimensional wavenumber sampling should be done in polar coordinates. Care has to be taken that the maximum cell diameter remains smaller than the resolution capacity $\Delta\mathbf{k}$, to avoid mismatch problems. We tested this scheme on the synthetic data successfully and used it in the analysis of the subsequent measurements.

3.5 Ambient vibration measurement test

To test the HRBF in real conditions a measurement was taken in the Hardwald just outside the city of Basel, Switzerland (Fig. 3.7). The site is a light forest of 3km^2 in a drinking water protection area near the river Rhine. The advantages of the site are that most artificial sources are far away compared to the array diameter, while the ground structure is very well known from many boreholes drilled for the ground water control. The site is characterized by 35 to 40 meters of quaternary gravels above the bedrock consisting mostly of Triassic chalks with some small graben structures of Keuper and Lias. The approximation of horizontal layering applies well to the site and the topography is flat with small irregularities of less than one meter. The average shear wave velocities are known from literature values as 300 - 500m/s in the gravels and 1000 - 2200m/s in the bedrock, giving a strong S-wave velocity contrast (Fäh et al., 1997b). This is

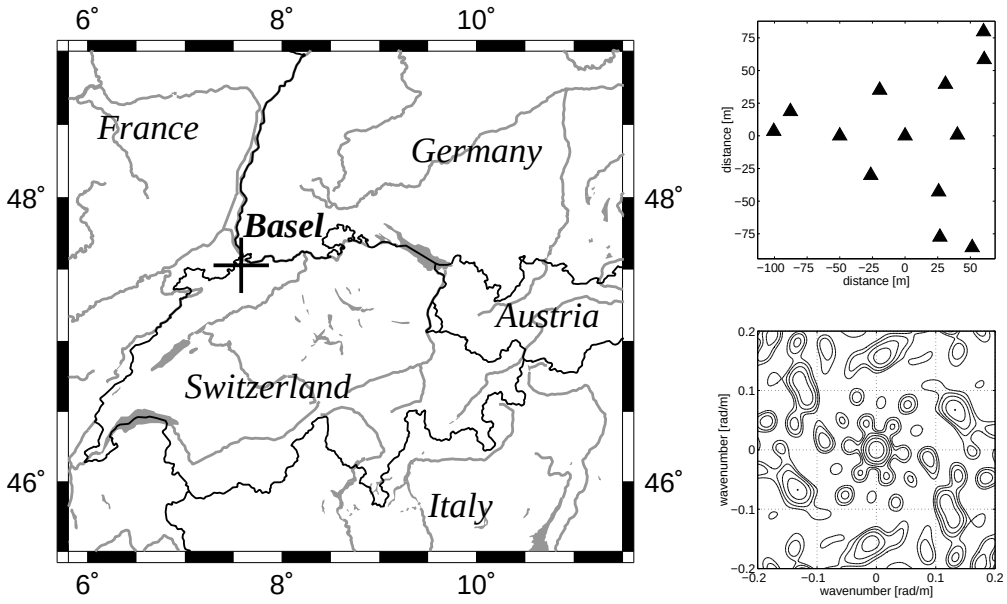

Figure 3.7: Location of the test site within Europe. The site is just outside the city limits of Basel. On the upper right the configuration used in the measurements is given. The beampattern of the configuration is given on the lower right. The width of the main peak is 0.0177rad/m, the background level is -11.3db and the aliasing period is larger than 0.2rad/m.

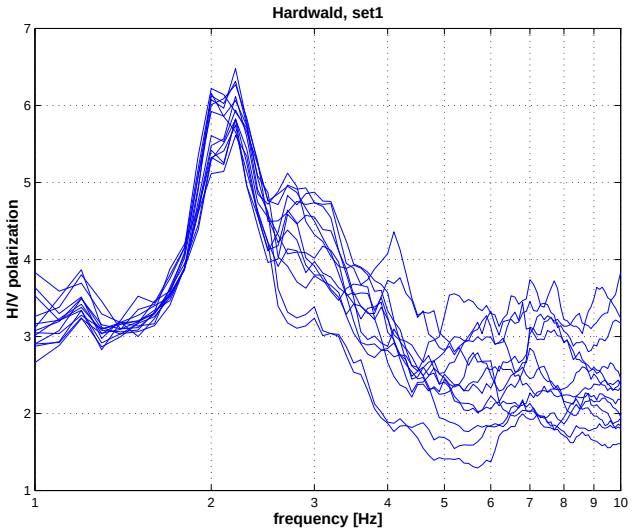

Figure 3.8: Overlay of the H/V polarization analysis of the data at each of the 13 sensors in the array.

confirmed by the H/V polarization analysis of the array sensor data, shown in Fig. 3.8. The curves are very uniform, suggesting one-dimensionality, and have a strong and clear peak at 2.2Hz, reflecting the strong velocity contrast. The variations towards higher frequencies suggest slight lateral inhomogeneities in the surface layer, as they have to be expected.

We deployed 13 three component short period sensors with a configuration as close as possible to example E in Fig. 3.3. The precision of the timing synchronization of the instruments was tested to be 1ms. Two sets of data were recorded during daytime with 2ms sampling interval for six minutes. The configuration and its beampattern are given in Fig. 3.7.

In the HRBF analysis the range 1 - 10Hz is analysed at fifty logarithmically distributed frequencies. The wavenumber sampling is done with a grid in polar coordinates with a directional resolution of 2.5^o and a wavenumber sampling corresponding to a phase velocity range of 100-3500m/s in steps of 25m/s. For each frequency layer the maximum spectral amplitude is determined and all values combined into the dispersion curve. Fig. 3.9 shows the extracted dispersion curve overlaid to the directional maxima of the f-$\mathbf{k}$-spectrum, to illustrate the uncertainty.

As we have already seen in the synthetic test, the frequency range where the dispersion curve can be extracted from the spectrum is limited. At the lower frequency end the width of the main peak limits the dispersion curve, because signals from multiple directions merge to one peak and therefore shift the peak to smaller wavenumbers or higher velocities. The rapid increase of the maxima below 2.2Hz is caused by this merging. No phase velocities could be

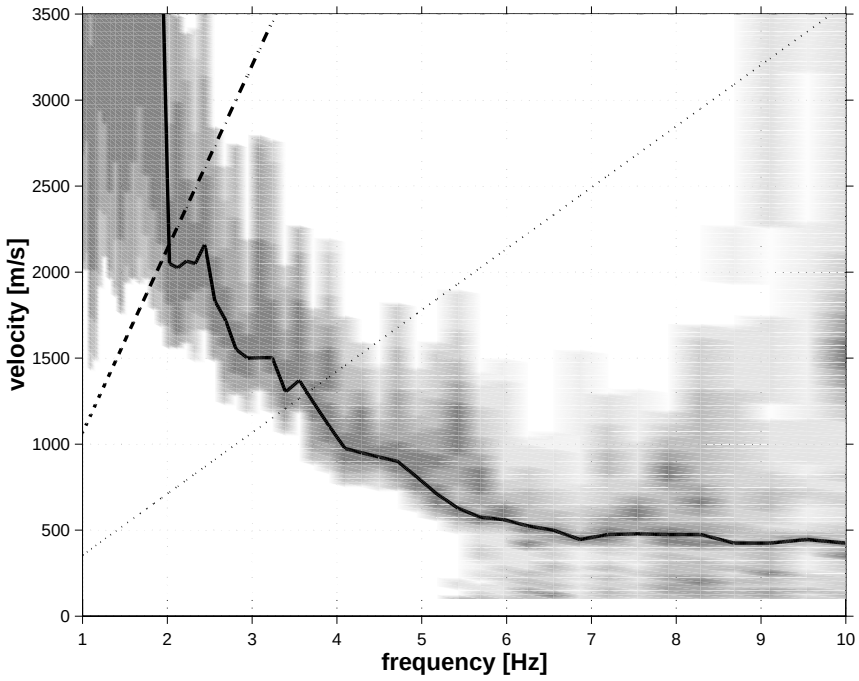

Figure 3.9: The continuous black line shows the dispersion curve extracted from the f-**k**-spectrum. Underlaid in a greyscale are the directional maxima of the spectrum. The thick dash dotted line shows the limit of one third of the beampattern width suggested by Asten & Henstridge (1984) as a limit for the resolution, agreeing closely with the limit from our test measurement results. The dotted line indicates the limit defined through the beampattern alone to illustrate the improvement possible by the HRBF.

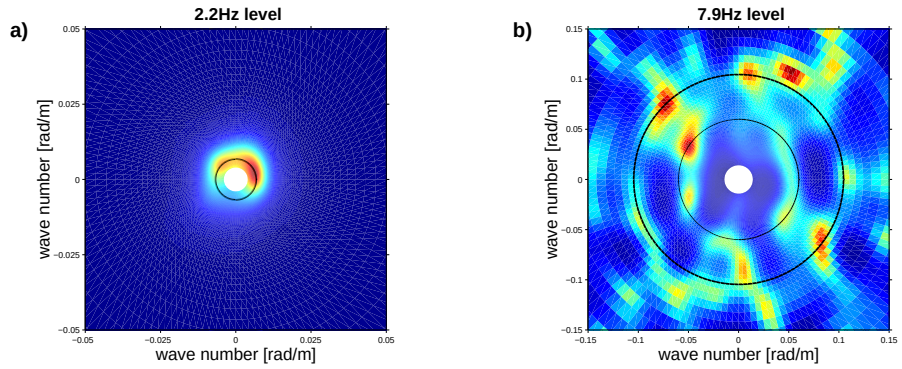

Figure 3.10: Examples of the f-k-spectrum at two frequency levels in the wavenumber domain. As expected from the theory, the peaks lie on circles with radii corresponding to the wavenumber of the excited surface wave mode at this frequency. In a) the level at 2.2Hz shows how the peaks at low frequency/high velocity are close to the center and will merge for lower frequencies. In b) the outer circle marks the fundamental mode wavenumber, while the inner circle indicates the wavenumber of a higher mode. Further peaks outside the circles are aliasing effects. The wavenumber range shown corresponds to the phase velocity range from 300m/s up to infinity at wavenumber zero.

identified below 2.2Hz. In Fig. 3.10a the section of the f-$\mathbf{k}$-spectrum for the frequency 2.2Hz is displayed as spectral amplitude against wavenumber. For lower frequencies and slightly higher phase velocities the peaks merge in the center as illustrated in Fig. 3.1(b). The dash-dotted line in Fig. 3.9 delineates the resolution limit $\Delta_{\mathbf{k}} = \Delta_{\mathbf{k}\,\mathrm{beam}}/3$, whereas the dotted line indicates the limit as defined through the beampattern. We find the same limit for the resolution of the dispersion curve in the results of the test measurement as suggested by Asten & Henstridge (1984). A further limitation of the analysis is the energy content of the different Rayleigh modes. Fäh et al. (2001a) suggest that in the range below the fundamental frequency of resonance the energy in the ambient vibrations can be distributed arbitrarily in other modes than the fundamental. The peak of the H/V polarization curves from the array data in Fig. 3.8 is at 2.2Hz, coinciding quite closely with the lower limit of the frequency range, where the dispersion curve can be extracted.

For the upper frequency end, the aliasing complicates the extraction of the curve. As could be seen in the synthetic test in Fig. 3.5, the multiple aliases of the peaks in the spectrum come closer together and make the identification of the fundamental mode difficult. Especially if higher modes contribute significantly to the spectrum, the multiplicity of peaks and aliases make the identification of the fundamental mode difficult. Fig. 3.10(b) shows the section of the f-$\mathbf{k}$-spectrum for the frequency 7.9Hz. The fundamental mode can be identified with some difficulty (outer circle), and also a second higher mode is visible (inner circle).

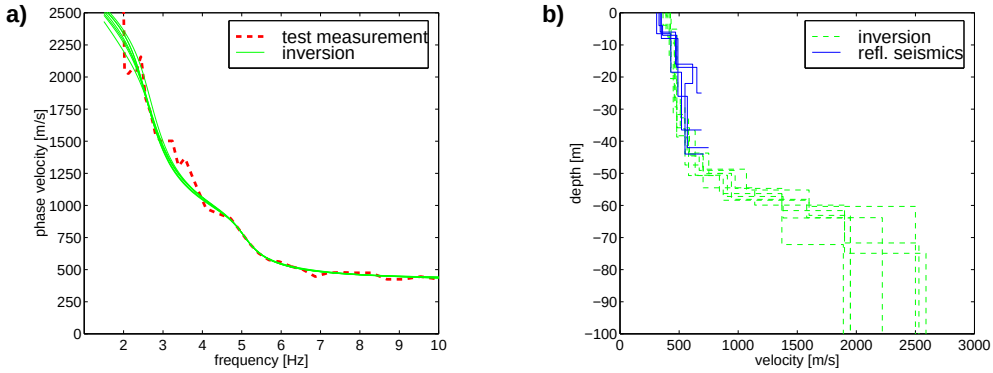

Figure 3.11: Results from the inversion of the data from the test site Hardwald. In a) the thick dashed line is showing the dispersion result from the test measurement. Superposed as thin continuous lines are the dispersion curves from the inversion results. In b) the corresponding velocity profiles of the inversion results are drawn as dashed grey lines with 4 profiles taken from a seismic reflection line crossing the array site superposed as continuous black lines.

The slight directional variations might indicate some deviation of the structure from the one-dimensional model.

Inversion

Our application aims at the derivation of S-wave velocities as they are needed for the assessment of local site effects in seismic hazard studies. A number of inversion algorithms and strategies are available and we choose one arbitrarily to illustrate the possibilities of the f-**k**-spectrum with the inversion results. With more effort the inversion results could be improved and a better control of the error attained, but we focus here on the extraction of the dispersion curve and not the inversion. So far we only use the dispersion of the fundamental-mode Rayleigh wave from the vertical component for the inversion. By looking at the second mode and the horizontal component, the method can be improved further.

The inversion scheme we use is a genetic algorithm procedure. The layer thickness and S-wave velocity of seven layers for the unconsolidated sediments and for two bedrock layers are selected as free parameters. The maximum depth of the sediments with S-velocities below 1400m/s is limited to 144m. Due to the non-uniqueness of the solution, several runs are performed with different ranges for the layer parameters and different weights to the segments of the dispersion curve during the inversion. The dispersion curve was calculated with modal summation (Panza, 1985) for all models in each iteration and the difference to the measured dispersion used as cost function. Iteratively the models were improved resulting in several plausible models. The inversion result is by nature non unique

and with the scheme used we have not much control on the absolute error. The great advantage of the approach used is the simplicity and quickness for reaching a reasonable result.

The dispersion of the best fitting models resulting from seven inversion runs are plotted in Fig. 3.11(a) as thin lines superposed to the dispersion extracted from the f-$\mathbf{k}$-spectrum (heavy line). The corresponding shear-wave velocity structures of the inversion results are given in Fig. 3.11(b) as grey dashed lines. The first 35-45 meters with shear-wave velocities between 400m/s and 500m/s are typical for the Quaternary gravels in this area. The depth range is in agreement with the information from surrounding boreholes at distances of about 100-200m from the array test site suggesting about 35-40m of gravels. We interpret the following 25 meters with a strong gradient as the eroded surface of the bedrock. The shear-wave velocity of the bedrock is consistently very high, in good agreement with the literature values in the range of 1000-2200m/s. The high contrast is also in excellent agreement with the large H/V polarization peaks in Fig. 3.8.

At the site of the array measurement an experimental shear-wave seismic reflection line has also been done (F. Nitsche[1], unpublished results). In Fig. 3.11(b) results from this experiment are shown as heavy dashed lines. They represent evaluations of the S-wave velocity profile from four points across the array. The values correspond very well with the inversion results from the dispersion curve measured with the array. They also illustrate an important advantage of the method compared to conventional borehole or reflection seismic S-wave techniques: Conservatively we get results from inversion to a depth of at least 100m with a very inexpensive method.

[1]Institute for Geophysics, ETH Zürich, Switzerland

3.6 Conclusions

The applicability of high-resolution beamforming to derive phase velocities from ambient vibrations was tested. First we compared the properties of different sensor configurations that had been used previously. Shapes based on triangles or circles are more generally applicable than rectangular shapes, but if the azimuth of strong ambient vibration sources is known in advance, rectangular shapes are very useful too. The comparison of the beampattern main peak width, aliasing pattern and background level show advantages and disadvantages of the configurations, but the differences are very small. Only the general properties of maximum aperture, shortest sensor distance, directional symmetry and a wide range of vector distances have to be provided for a good configuration. This result underlines the flexible application of the technique also to sites where the layout of the instrumentation is restricted.

Tests with synthetic ambient vibrations confirm the capability of the method to extract the correct phase velocities of the excited Rayleigh modes and gave insight in the form of the results that have to be expected. The analysis parameters for the wavenumber resolution could be optimized for better resolution where it is needed and for faster calculations.

A measurement at a site close to the city of Basel in Switzerland illustrates the applicability of the method. The dispersion curve of the fundamental mode Rayleigh wave was determined for the frequencies from 2.2Hz upwards up to 10Hz and inverted for the S-wave velocity structure. The resulting structural models correspond well to data from a S-wave reflection survey and the geological information for the site.

The array technique is a very cost and time efficient tool for measuring S-wave velocities, as only half a day of field work and two to three days of data processing is needed for a measurement. For the study of local earthquake hazard and in deterministic modelling of earthquake scenarios, the lack of S-wave velocity information is often the source of large uncertainties. This array technique and other methods based on ambient vibrations are a step towards the feasibility of seismic zonation through numerical modelling of site effects.

Chapter 4

Geophysical Model

4.1 Geometry of the 3D Model

At the Geological- Palaeontological Institute of the University of Basle the geologic information for the 3D geologic structure in the area of Basle has been compiled and integrated into a digital model (Zechner et al., 2001). This model presents the geometrical base for the geophysical model. The 3D model consists of seven geological discontinuities and the surface planes of 22 known major faults in the area. An illustrative snapshot of the model is given in Fig. 4.1. The geologic cross section in Fig 1.3 is derived from the model and illustrates the six sedimentary bodies inclosed by the geologic interfaces: They are the Quaternary sediments (QUA), the Tüllinger Layers (TUE), the Molasse Alsacienne (ALS), the Meletta layers (MEL), the lower Tertiary and upper Mesozoic sediments (UPM) and finally the Mesozoic sediments (MES). Below the last discontinuity the Paleozoic sediments and christaline basement rocks (PCB) complete the model. Table 4.1 lists the stratigraphic units and their abbreviations.

The decision to differentiate and model the interface geometry between the first four geologic units of the model (QUA,TUE,ALS,MEL) was based mainly on the distinct lithology at the bottom of the Quaternary sediments, as it is mapped from the database of boreholes in the Basle area (Noack, 1993). The Tertiary interface below the Meletta layers was modeled because literature values indicated a significant S-wave velocity contrast at this interface. The Mesozoic sediments are included because they form the pre-Quaternary basement rock of the Tabular Jura part of the model. The model covers an area of approximately 400km^2 and contains the complete Basle region. In the deepest part of the model in the Rhine Graben the MES/PCB discontinuity reaches a depth of 2000m.

The surface interface is derived from the digital elevation model of the region and therefore quite precise. The second layer representing the pre-quaternary interface is very well constrained from a large database of boreholes down to the Tertiary sediments (Noack, 1993). The uncertainty increases as the density of

Abbreviation	Stratigraphy
QUA	Quaternary sediments
TUE	Tüllinger layers (Tertiary); marls and argillaceous marls
ALS	Molasse Alsacienne (Tertiary); sandy marls
MEL	Meletta layers (Tertiary); sandy and argillaceous marls
UPM	lower Tertiary/ first Mesozoic sediments; Sannoisien (Tertiary) and upper Mesozoic sediments down to Lias
MES	lower Mesozoic; Mesozoic sediments of the Lias and older
PCB	lowest Mesozoic sediments ("Buntsandstein"), Paleozoic sediments ("Rotliegendes") and crystalline basement.

Table 4.1: Stratigraphic units represented in the 3D-mode and their abbreviations.

the borehole data thins out with distance from the inhabited areas. The prequaternary surface of the TUE, ALS and MEL derive also from the borehole information. The deeper interfaces are compiled from structural interpretations by Gürler et al. (1987) and Bitterli-Brunner & Fischer (1988). They provide some profile sections and interpreted maps of the MEL/UPM and the MES/PCB discontinuities, based on unpublished seismic cross section data for exploration of natural resources (oil/gas). The information was digitized and then interpolated for the different interfaces with the GOCAD geological object design code (GOCAD, 1999). In addition, the surfaces of the 22 major known faults in the area were constructed, and intersected according to their likely structural-geological relationship. The final model parts, or volumes, are bound by model horizons representing stratigraphic contacts and modeled fault surfaces.

From this approach, the geometry of the geological interfaces is mainly determined through interpolation between the deep boreholes, qualitative constraints and interpretations. An exception is the thickness of the Quaternary sediments, which is well constrained. The geological information on the deeper structures are few, resulting in an uncertainty on the actual position of the interfaces, that increases with depth and lateral distance from the deep boreholes (see Fig. 4.1, drill rig symbols).

4.2 Geophysical Parameters

The geophysical parameters needed for numerical simulation of seismic wave propagation are density, P-wave velocity, S-wave velocity and the corresponding Q values to model anelasticity. Two recent studies compiled literature values for the region, Fäh et al. (1997b) and Steimen et al. (2002). The parameter the least constrained by the literature is the S-wave velocity. A major goal of this

Figure 4.1: Geologic 3D model geometry (Zechner et al., 2001). Through the transparent topography with contours the geologic units below the surficial Quaternary sediments can be seen (labels as defined in table 4.1). Between the red bottom layer and the topography the seismic contrast layer is visible in yelow. The faults included in the model are partially visible as blue shade. Blue drilling rig symbols indicate deep boreholes from which information was available. A red line indicates the limits of the canton of Basle for orientation.

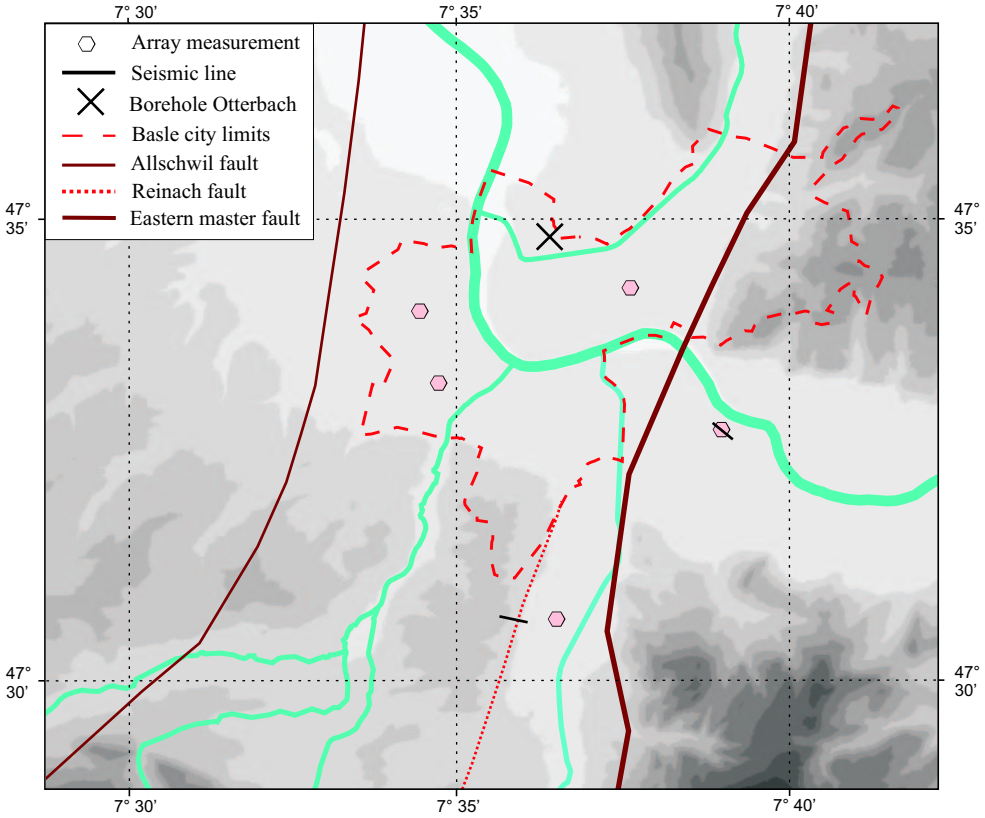

Figure 4.2: Overview of the new data sources for seismic velocities available for the model.

study was to fill this gap, as S-waves are a crucial factor in earthquake hazard. Therefore we concentrated our efforts on determining reliable S-wave parameters. P-wave velocities are more readily available and we could take advantage of two seismic lines. For the deeper lower Tertiary/ first Mesozoic layers Sonic log information from a recent deep borehole (GPI Basle, 2001) was accessible.

To derive the S-wave velocities for the four seismically softer layers and the lower Tertiary/ first Mesozoic, the application of an array technique to ambient vibrations was developed (chapter 3). A campaign of five array measurements was performed in Basle (Fig. 4.2, hexagons). The sites were selected to sample the four Tertiary layers in the Rhine-Graben and the upper Mesozoic, where the layer is close to the surface in the Tabular Jura. The inverted S-wave velocity structures are presented in Appendix A. The measurements constrained the S-wave velocity of the Quaternary and the Tertiary sediments. For the three Tertiary units TUE, ALS and MEL a slight gradient was derived.

A deep borehole recently drilled for a geothermal tests and exploration was accessible and provided caliber, gamma-ray/density and sonic logs (GPI Basle, 2001). The results are shown in appendix B, the position is marked as cross in Fig. 4.2). For the softer sediments above the lower Tertiary/ first Mesozoic no data was available due to technical difficulties in the borehole. The velocity values are practically constant, with variations corresponding to caliber variations in the borehole. The average values determine the data for the lower Tertiary/ first Mesozoic and the lower Mesozoic in the geophysical model.

P-wave velocity data from two seismic profiles were accessible from sites indicated as lines in Fig. 4.2. One reflection seismic line was done in a paleoseismic study across the fault causing the 1356 earthquake (Meghraoui et al., 2001), the other line is unpublished so far (F. Nitsche, personal communication). The interval velocities derived for the time to depth conversion in the seismic profiles were used for the P-wave velocities in the Quaternary and Tüllinger layers and they also confirmed the P-wave velocities in the lower Mesozoic. Finally the P-wave velocities for the Molasse Alsacienne and the Meletta layers had to be taken from the literature (Clark (Ed.), 1966). The densities and Q values derive from literature values and estimates collected in the earlier studies Fäh et al. (1997b) and Steimen et al. (2002).

The collection of all average values and the uncertainty ranges in the velocities are listed in table 4.2. For the Tertiary layers TUE, ALS and MEL the velocity gradient as described by table A.1 can be used to refine the model, depending on the application.

model unit	ρ $[kg/m^3]$	V_P $[m/s]$	Q_P	V_S $[m/s]$	Q_S
QUA	1850	800^C (600-1000)	30	450^A (400-500)	15
TUE	1850	2200^C (1800-2600)	50	725^A (650-900)	25
ALS	1850	2200^D (2000-2800)	50	650^A (600-800)	25
MEL	2000	1800^D (1400-2500)	50	600^A (450-700)	25
UPM	2350	3400^B (3200-3600)	125	2000^B (1800-2200)	50
MES	2550	4000^B (3600-4500)	125	2350^B (2150-2650)	50

^{A}Array measurement; ^{B}Borehole sonic log; ^{C}Reflection seismics; ^{D}Literature

Table 4.2: Geophysical parameters of the 3D model. The stratigraphic meaning of the model unit abbreviation is explained in table 4.1. The velocity values are averages for the whole layer, the values in parenthesis are minimal and maximal values as either determined in the measurements or in the variability of literature values.

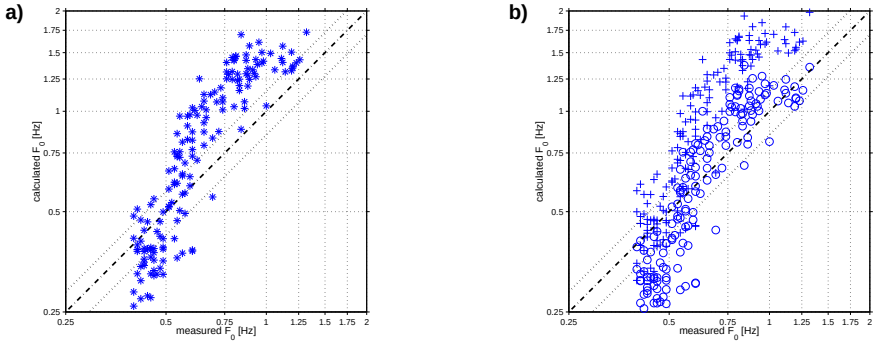

Figure 4.3: Measured versus calculated fundamental frequencies from the model before the corrections to the geology. The dotted range marks the ±15% uncertainty margin in the measured frequencies. Part a) shows the f_0 values calculated with the average S-wave velocity model, while part b) shows the f_0 values calculated with the maximum S-wave velocities as crosses and circles for the minimal S-wave velocity models.

4.3 Refinement of the model with H/V polarization

At this stage the model consists of the collection of all necessary information and its uncertainty. To verify and refine the model, we use the data from the H/V polarization survey, that provided fundamental frequencies for the Basle area (chapter 2). The fundamental frequencycan be calculated in a simple way from the geophysical model and therefore provides a simple means for validation of the model. Because of the irregular distribution of the H/V polarization measurement points and the focus of the interest on the city of Basle, the validation was limited to a the area of the city of Basle itself. Over the Tabular Jura no attempt at model validation was done: The shorter wavelength associated with the higher fundamental frequencies are more sensitive to lateral inhomogeneities, so variations in the composition of the soft sediments are of more importance.

For all measurement sites within the Rhine Graben and inside or close to the border of Basle (160 out of 250), a 1D sediment profile was extracted from the digital 3D model. The relevant contrast for the H/V polarization is between the Meletta layers and the lower Tertiary/ first Mesozoic, clearly identified from the velocity model. Fundamental frequencies were then calculated as vertical 4-way S-wave travel times between surface and the contrasting interface. Fig. 4.3a) shows the comparison of calculated and measured frequencies before the correction to the geometry of the 3D model. The dotted lines indicate the ±15% uncertainty margin in the measured frequencies. The maximal and minimal S-wave velocities derived for the geophysical model were used to calculate upper and lower limits

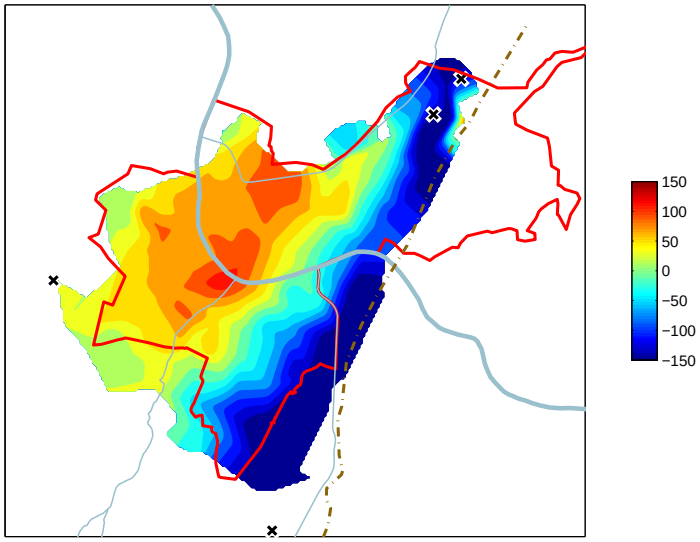

Figure 4.4: Magnitude of the corrections applied to the model geometry at the bottom of the Meletta layer in meters. Positive values indicate an increase of the thickness, negative values a decrease. Crosses mark the location of deep boreholes constraining the deeper interfaces.

as well. The corresponding values are shown in Fig. 4.3b) as crosses for the maximum and circles for the minimum velocity model.

In the higher frequency range, the calculated frequencies are to large. Even considering the uncertainties in the S-wave velocity and the measurements does not give an acceptable agreement. The concerned sediment depth ranges between 50m and 100m from the surface, where the S-wave velocity is very well constrained through the array measurements, so the velocity model cannot be the cause for the discrepancy. The fundamental frequencymeasurements are well constrained as well, considering their stability and conservative uncertainty constraint of 15%. This suggests that the error lies in an underestimation of the thickness of the sedimentary layers in this part of the model, which is based on extrapolation from data sources at distances in the order of kilometers. Comparison of the S-wave measurement inversion with the digital model (Figs. A.3,A.5) had already indicated the same, but the most convincing piece of evidence are the results from the newly accessible data of the deep borehole Otterbach (GPI Basle, 2001), which confirmed the corrections on the horst of Basle.

The much lower calculated values for the measured frequencies below 0.6Hz cannot be explained by the uncertainty in the constant velocity model either. The gradient visible in the array measurements can reduce the difference slightly, but

it cannot explain the difference fully either. Estimated theoretical 2D resonance frequencies determined for a section of the syncline of St. Jacob Tüllingen by Steimen (1999) coincide with the theoretical 1D fundamental frequencies and the H/V peaks as well. So it is possible, that the low f_0 in the syncline is associated with a 2D resonance, but so far no conclusive data is available for discriminating the 1D and the 2D case in Basle. Weighting the lack of hard data on the geometry of the model at depth against the uncertainty of the velocity model in the deeper sediments and the 2D/1D question, we favor a correction of the geometry to the 1D interpretation of f_0 in order to get a model from a consistent approach. The amplification calculations in chapter 5 justified the approach, as the amplification peaks coincide with the fundamental frequencies. But the spatial extent of the amplification peaks is so widespread across the syncline, such that a 2D interpretation can neither be identified nor ruled out.

From the deviations in f_0 at all measurement points corrections to the depth of the MEL/UPM interface were calculated and integrated in the model. The magnitude of the corrections is shown in Fig. 4.4, they range from more than 50m over the horst of Basle to more than 100m within the Rhine Graben. In the construction of the geological model, the interfaces in the Tertiary layers depend on each other. So the modification of the MEL/UPM interface initiates corrections to the ALS and TUE layers as well. The effects are illustrated in Fig. 4.5, where sections along identical coordinates are shown for the initial and the corrected model, the location of the sections is indicated in Fig. 1.2. The modifications from the fundamental frequencies concern the dominant seismic contrast (black line) in the model. The layers MEL, ALS and TUE are then constructed with thickness constraints and information from the geology below the Quaternary surface sediments. Over the horst of Basle only the MEL layers are concerned, their depth is significantly increased below the city. In the syncline of St. Jacob Tüllingen the modifications are most significant, here all three sedimentary layers are reduced in thickness. Within the fault zone of the Rhine Graben master-fault the model is modified as well, but the geometry of interfaces is unknown, because of probable staggering of the fault and deformations of the layering. As the approximation of horizontal layering breaks down in the fault zone, fundamental frequencies cannot be interpreted in this zone.

Fig. 4.6 shows the f_0 comparison results from the model with the newly interpolated lower Meletta interface. A very interesting result is that the uncertainty of approximately 15% in the determination of the fundamental frequency from measurements matches the uncertainty in the f_0 resulting from the possible ranges in the S-wave velocity model.

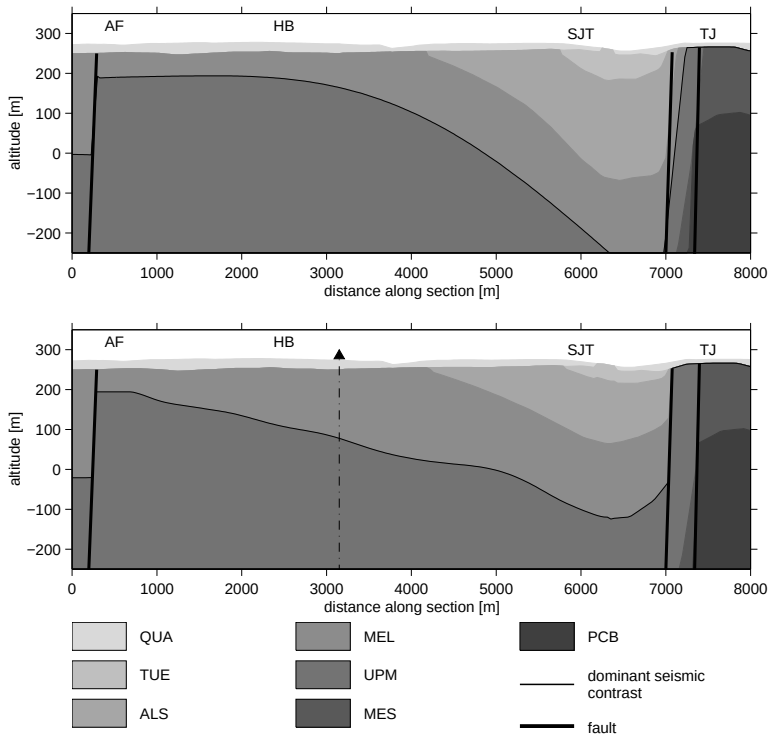

Figure 4.5: Illustration of the corrections to the geologic model. The upper part of the figure shows a section from the initial model, while the lower part of the figure shows the same section after the correction. The labeled structures are the Allschwil fault zone (AF), the horst of Basle (HB), the syncline of St. Jacob Tüllingen and the Tabular Jura (TJ). A triangle and a dash dotted line indicate the area of the horst of Basle where the new borehole confirmed the corrections to the model geometry.

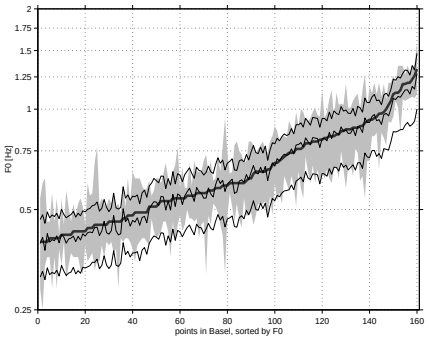

Figure 4.6: Measured versus calculated fundamental frequencies from the corrected geometrical model. The measured f_0 (thick grey line) is shown sorted by value with the grey shaded area indicating the uncertainty from the interpretation of the H/V ratios. The thin black lines show the calculated f_0 and the uncertainty range in the calculations derived from the uncertainty in the S-wave velocity model.

4.4 Conclusions

With the corrections on the 3D model a consistent geophysical 3D model could be derived. All available geological information has been integrated and led to the 3D geometry of the model. For the geophysical parameters of the model also all available information has been considered and the largest gap, the S-wave velocities, was filled with measurements. The array method applied for S-wave measurements proved to be an efficient tool for deriving S-wave velocities from ambient vibrations.

The use of fundamental frequencies to verify the 3D model proved to be a very valuable tool to improve the model uncertainties. As well in the Syncline of St. Jakob Tüllingen as over the Horst of Basle, the method allowed to correct the overall soft sediment thickness, that were based on a qualitatively good, but quantitatively uncertain geometrical model. This also emphasizes the quantitative uncertainty in 3D geometries derived from the interpolation over large distances between cross sections and from the interpretation of seismic profiles for the sections themselves. The effect of these uncertainties can be large and the extensive use of H/V polarization measurements commends itself with its inexpensiveness and efficiency.

The weak spot of the model are the geophysical parameters at depths of more than 100m, where a velocity gradient is probable, but undetermined. Only data from future deeper boreholes or an array experiment on a larger scale can reveal more information about that part of the structure. But the 3D model derived here represents the state of knowledge for the region of Basle and can be used as reference model for further seismic exploration and numerical modeling of earthquake site effects.

Chapter 5

Ground motion amplification in Basle

The final part of this thesis is the determination of ground motion amplification for the Basle area. This is done by numerical modelling of scenario earthquakes on 2D sections of the geophysical model. Spectral amplifications are derived by comparison with a corresponding simulation on a reference structure. As the wave field of a specific earthquake is depending on the source distance, depth, fault mechanism and fault orientation, a single scenario is not sufficient to cover all the possible amplification effects. In a specific scenario a site might not show any amplification due to the specific wave field of the source, while another source type or location might cause amplifications. Therefore a variety of scenarios with varying source parameters are calculated to determine ground motion amplification along the sections and its variability from the sources. We restrict the computations to the SH-part of the wave field.

From the S-wave velocity information we deduce that within the Rhine graben the amplification effects are mainly caused by the soft Tertiary sediments reaching a depth of 500m in the syncline of St. Jacob Tüllingen. The predominant 2D character of the structure below the city of Basle and the large scale length derived from the long wavelength associated with the structures of the Rhine graben allow a 2D approximation in this part of the model for determining amplification effects. Over the Tabular Jura in the eastern part of the model the site amplification effects are dominated by the Quaternary sediments and possibly the topography, involving scale lengths in the order of 20-30m. The information in the model is not detailed enough to resolve such scales, therefore we will not determine amplification effects for this area.

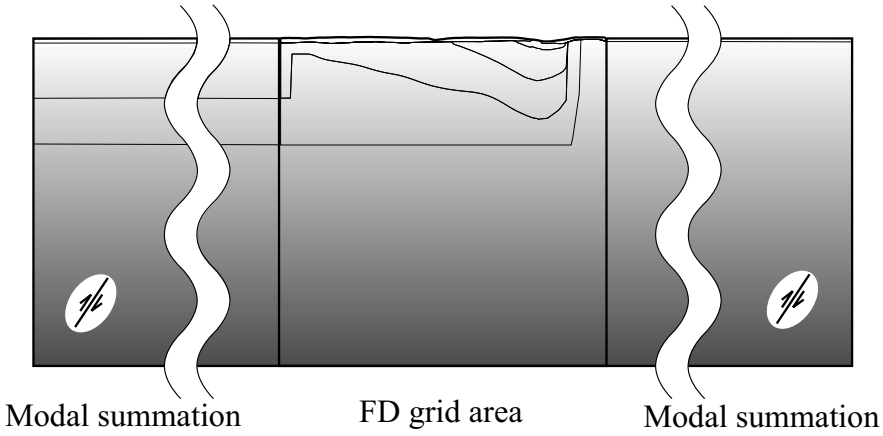

Figure 5.1: Illustration of the hybrid numerical modelling scheme. The sources are modelled in the 1D background structure and the generated wave field is propagated with modal summation to the area of the FD grid. Scenarios are generated with varying source mechanisms, epicentral distances, source depths and for sources on either side of the section.

5.1 Numerical Modelling

A hybrid numerical modelling scheme developed by Fäh (1992) is used. The ground motion on the geophysical model is calculated with a 2D finite-difference scheme, while the propagation from the source to the model area and the source itself are calculated with modal summation. The concept is illustrated in Fig. 5.1. Each of the two techniques is applied in that part of the structural model where it works most efficiently: the finite-difference method in the laterally heterogeneous part of the structural model that contains the sedimentary basin, and modal summation is applied to simulate wave propagation from the source position to the sedimentary basin. Thus computing time and memory are used most efficiently.

The modal summation part is based on the formulation by Haskell (1953) and described in Florsch et al. (1991). The computations include the "mode-follower" procedure and structure minimisation described by Panza & Suhadolc (1987). The introduction of anelasticity into the computations is based on variational methods (Takeuchi & Saito, 1972; Schwab & Knopoff, 1972) and includes the results of Futtermann (1962) concerning the dispersion of body waves in a linearly anelastic medium. The seismic source is introduced by using the formalism of Ben-Menahem & Harkrider (1964). The seismograms computed with modal summation contain all the body waves and surface waves whose phase velocities are smaller than the S-wave velocity of the half-space that terminates the structural model at depth. These computations therefore supply the SH-part of a realistic incoming S-wave and surface-wave wave field that is used as input in the finite-difference computations.

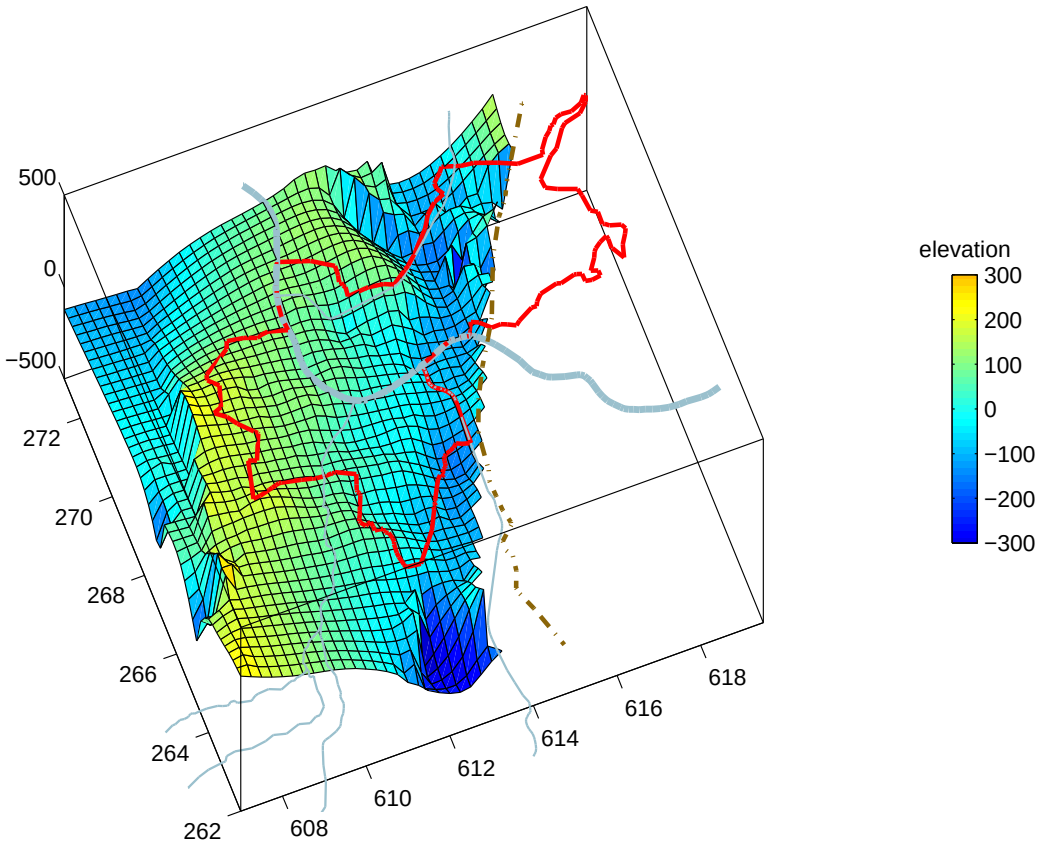

Figure 5.2: 3D-Geometry of the lower bound of the soft sediments (interface MEL/ UPM), where a strong contrast in the S-wave velocities is present.

The FD scheme for SH waves is based on the FD method developed by Korn & Stöckl (1982). Anelasticity is included by using the rheological model of the generalised Maxwell body (Emmerich & Korn, 1987; Fäh, 1992). This approximation can account for a constant quality factor over the frequency band of interest. The discretisation is of second order in time and in space. The scheme requires a minimum of 10 grid points per wavelength. A spatial grid resolution of 8m is chosen for the computations and the minimal S-wave velocity in the models is above 400m/s, so the maximum frequency resolved is slightly higher than 5Hz.

5.1.1 Structural models

The scenario earthquakes are modelled on 2D cross-sections extracted from the geophysical 3D model. The 2D approximation to the structure is valid if the variations of the model vertical to the section plane are small compared to the relevant scale length in the model. To insure this prerequisite, we investigate the two most relevant interfaces in the model, which are the topography and the

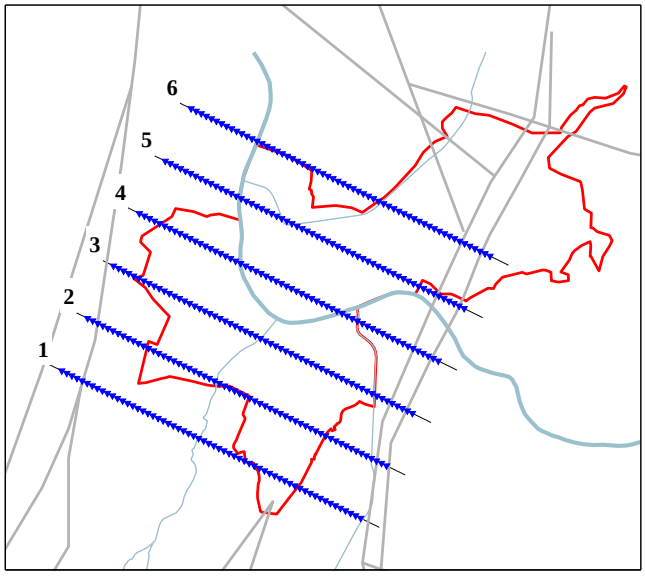

Figure 5.3: Sketch of the location of the sections used in the numerical modelling.

S-wave velocity contrast at the bottom of the Meletta layers.

The most important lateral heterogeneity of the S-wave velocity contrast are the syncline of St. Jacob Tüllingen and the eastern masterfault of the Rhine Graben. The main axis of these structures are parallel in the area of the city of Basle as it is illustrated in Fig. 5.2, where the position of the dominant S-wave velocity interface is shown. To the south the Rhine graben fault curves and the synclinal structure widens and to the north some faults cross the syncline, introducing lateral variations that render a 2D approximation invalid. But in the area of the city of Basle the dominant variations are vertical across the syncline and a 2D approximation by a section vertical to the syncline axis is acceptable. On the topography the slopes in the area of Basle are either smaller than 5^o or the orientation of the slope is within 10^o of the azimuth vertical to the syncline axis, which supports this 2D approximation.

Still the thicknesses of the sediments in the Rhine graben vary along the syncline axis and the amplification response can be expected to differ. To derive information about this variability not only one representative 2D section is modelled, but six cross-sections are extracted from the geophysical model as indicated on Fig. 5.3. Each section is of 8km length and the numerical signals are recorded at 60 positions on each section with a spacing of 120m, indicated as small triangles. The geophysical parameters used in the numerical modelling are the ones discussed in chapter 4 and given in table 4.2, but with the gradient derived for the soft sediments in table A.1.

As reference structure for the ground motion amplification we use a 1D model derived from the Tabular Jura, but with the Quaternary removed. A slight S-wave velocity gradient in the top 30m of material, increasing from 1000m/s to

2000m/s simulates the realistic situation at a reference station and the structure as it can be encountered at the seismic stations from which the regional hazard is determined (rock sites). The sections are then embedded in a 1D regional background model, proposed by Fäh et al. (1997a) for the Basle area. The velocities increase with depth, and the layering on the eastern or western side is horizontally extended from the sections into the background model (see Fig. 5.1).

5.1.2 Scenario earthquakes

In the ground motion scenarios we consider a wide range of parameters, so as to allow for all contingencies. Two source mechanisms are considered, which represent the dominant mechanisms for the tectonic regime of the area of Basle. The mechanisms are normal faulting combined with some strike slip component and strike slip with some normal faulting component. The sources are aligned either with the Reinach fault or the eastern master fault of the Rhine graben; the variation is accounting for radiation effects. Two source depths (5km and 10km), two source distances (20km and 40km) and sources as well on the eastern as on the western side of the cross-sections are considered. Point sources are modelled, assuming that energy is mostly radiated from an asperity at the given depth and epicentral distance. The source spectrum was flat, so as to produce energy at all frequencies for the amplification calculation. The resulting 16 scenario earthquakes from all combinations of source parameters cover the variability of ground motion amplification due to the source and the location.

5.2 Amplification results

The scenarios are modelled as well on the six sections as on the reference structure. Response spectra are calculated for each seismogram in terms of acceleration and with 5% damping. With the corresponding data from the reference structure the spectral amplification is calculated. The results from different sections are very similar, especially in the association of the amplification effects with the 2D model structure. Therefore we use a single section (number 3) to discuss the basic amplification results. The results from the other sections are shown in in Appendix C.

Fig. 5.4 illustrates the amplification from the different scenarios for a point over the syncline of St. Jacob Tüllingen. The amplifications are sorted by the source distance and depth, the results from the two source mechanisms are shown on the same graph. The comparison of the different scenarios underline the expected dependency of the amplification on the source type and position. The fundamental frequency of resonance calculated from the model is marked with a vertical black line. The agreement is excellent throughout the sections and positions on the section. The variation in the location is in the order of $\pm 15\%$,

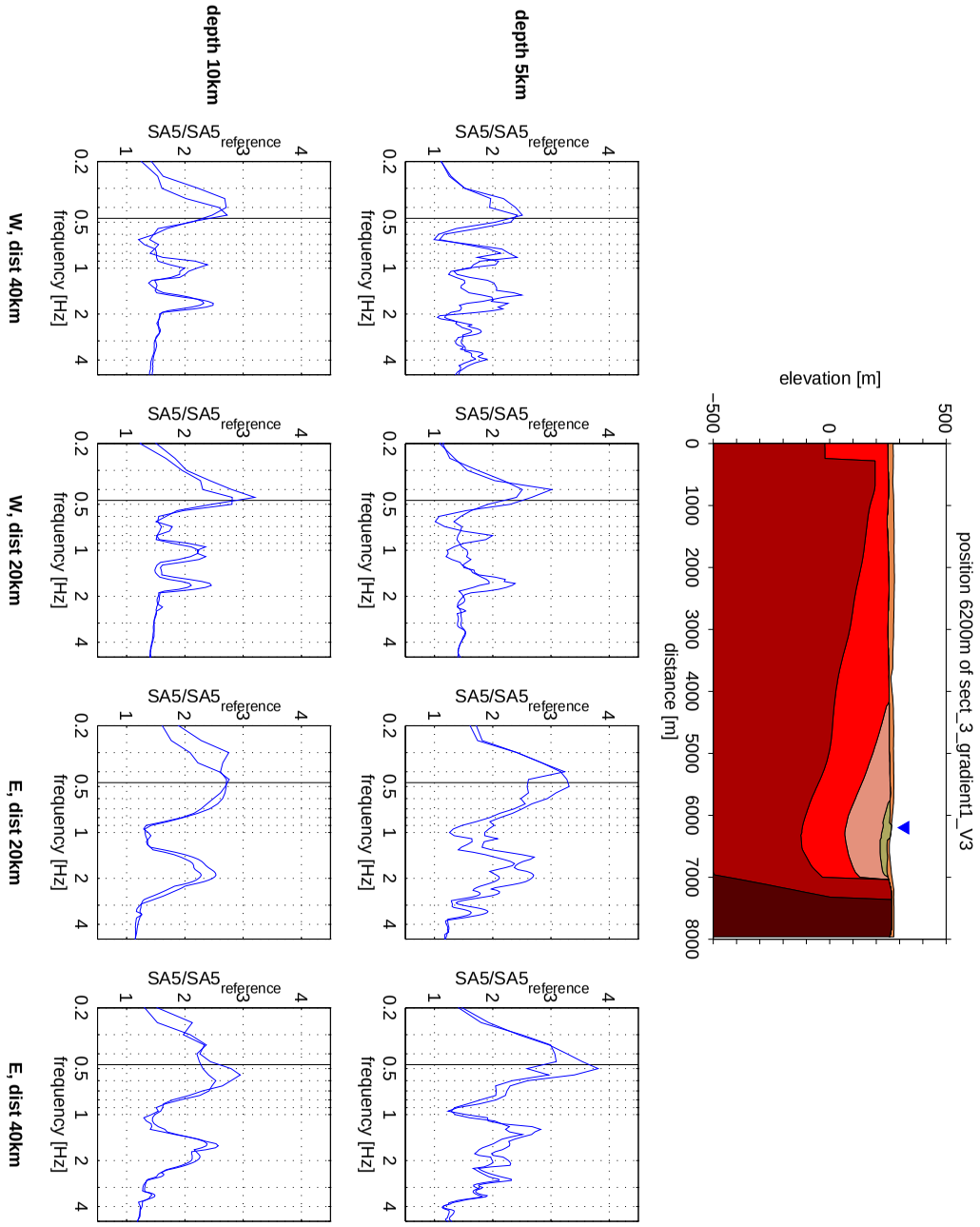

Figure 5.4: Amplification for a point in the syncline of St. Jacob Tüllingen. The triangle over the geologic cross section indicates the location of the point in the Rhine graben. The amplification at this point from different scenario earthquakes are shown in individual graphs, sorted for source depth and epicentral distance. The two curves in each graph are the amplification for the two modelled source mechanisms. A vertical black line marks the fundamental frequency for the location.

the same variation that was determined for the fundamental frequencies in the H/V polarisation survey in chapter 2. Peaks at higher frequencies appear as well and the consistency of their location suggest the excitation of higher modes of resonance.

The next step towards a zonation of the city of Basle is to get an overview on the amplification across the Rhine graben. To this purpose the amplification from the different scenarios are averaged at each point and collected in Fig. 5.5, where the average amplification is shown color coded against the position along the section and the frequency. A black line indicates the fundamental frequencies calculated from the model and underlines the close coincidence with the primary amplification peak. The peak value of the average amplification in the Rhine Graben varies not much with the sedimentary depth, it is about 3. Only at the western edge are lower values visible. The slightly lower values of peak amplification in the range between 4500m and 5500m along the section is associated with a somewhat elevated bump in the bottom interface of the soft sediments, where the wave energy is diffracted, probably causing the elevated values at the position around 3500m. The peak above the syncline (6000m) can be interpreted as focusing from the bottom interface as well.

At higher frequencies the secondary peak parallelling the primary one is visible in a wide area, further supporting the interpretation as a higher mode of resonance. The strong secondary peak at distance 6000m further illustrates the focusing of wave energy by the syncline bottom. Close to the master fault the amplification actually seems to decrease, ridges of elevated amplification towards higher frequencies are probably associated with reflections at this S-wave velocity contrast. The amplifications in this part of the model have to be regarded with some reservation, as the structure of the master fault zone is not well known and is most probably staggered and the layer structure broken up.

If we consider the envelope of the amplifications from all scenarios at each point instead of the average, the structure of the amplifications basically remains the same (Fig. 5.6). But the amplification levels are drastically raised by more than one unit. Furthermore the peaks are widened in the frequency range, caused by the variability in the peak frequency from the different scenarios. A very interesting feature is also the very high amplification levels below the fundamental frequency of resonance in the distance range 4000m to 5000m. Resolving the amplifications from the different scenarios at such a point (Fig. 5.7) shows that these maxima are caused by the shallow source scenarios with the source to the east of the section. This suggests that strong low frequency surface waves are generated at the master fault and propagated farther into the Rhine graben. The strong peaks at higher frequencies indicate that numerous higher modes can also be excited, depending on the local subsurface geometry of the geologic interfaces as well as the source.

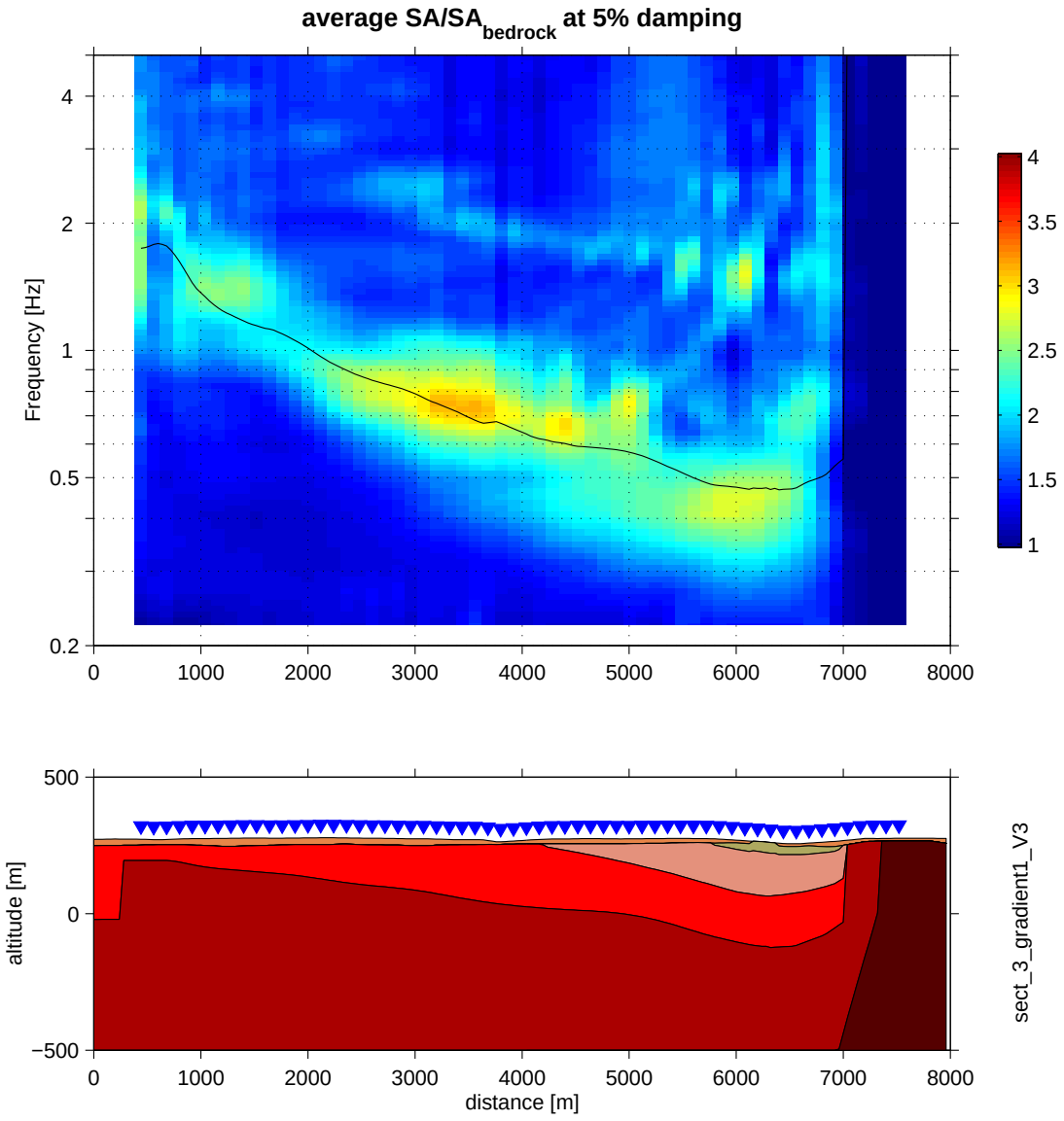

Figure 5.5: Mean spectral amplification along section 3: The lower part of the figure shows the model cross-section used in the simulation, triangles indcate the positions where amplifications were calculated. The upper part of the figure shows in color code the mean spectral amplification along the section, dependent on location and frequency. The black line identifies the fundamental frequencies calculated from the model, which agree very well with the frequency of the peak amplification.

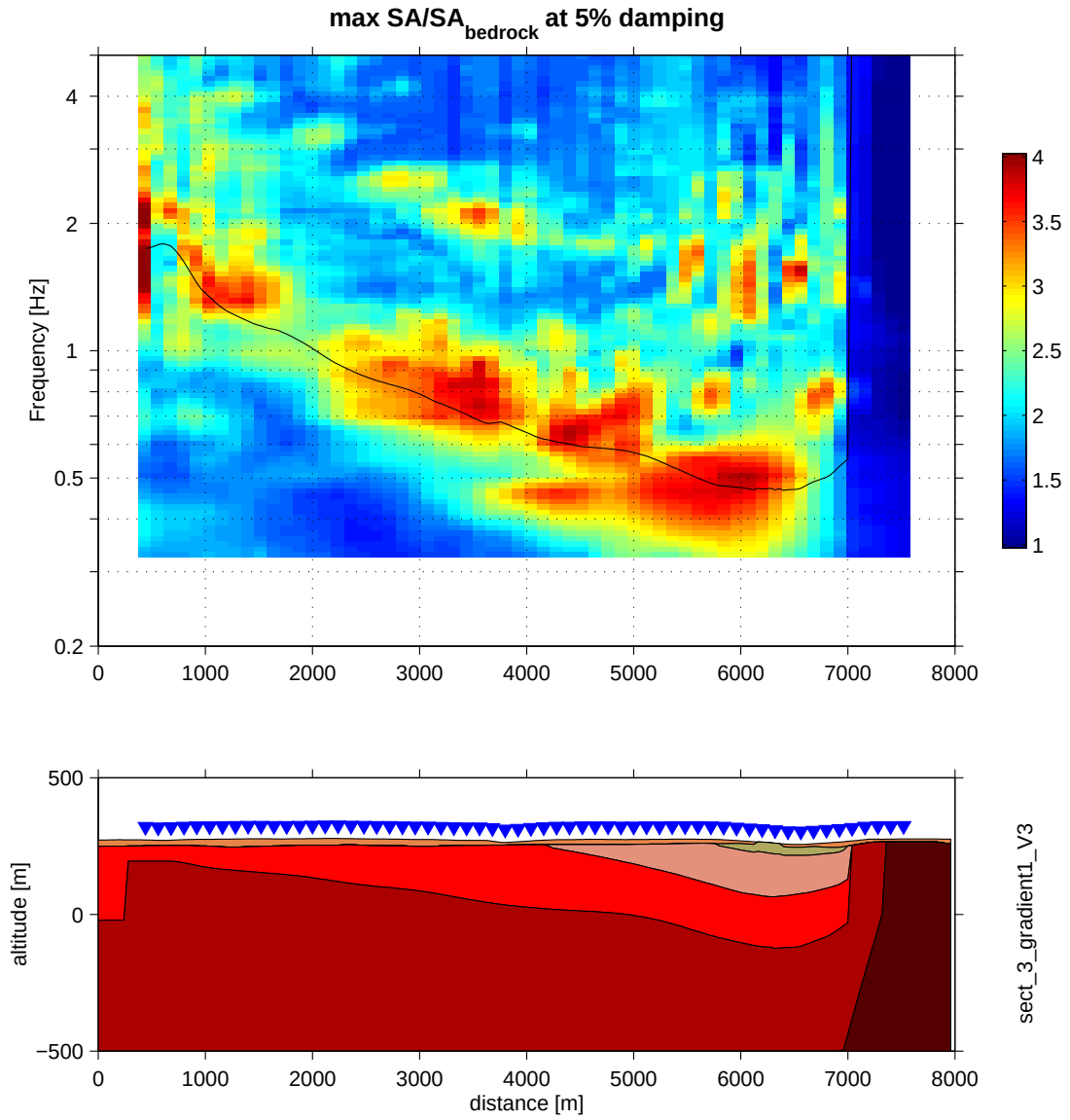

Figure 5.6: Maximum spectral amplification along section 3: The lower part of the figure shows the model cross-section used in the simulation, triangles indcate the positions where amplifications were calculated. The upper part of the figure shows in color code the mean spectral amplification along the section, dependent on location and frequency. The black line identifies the fundamental frequencies calculated from the model, which agree very well with the frequency of the peak amplification.

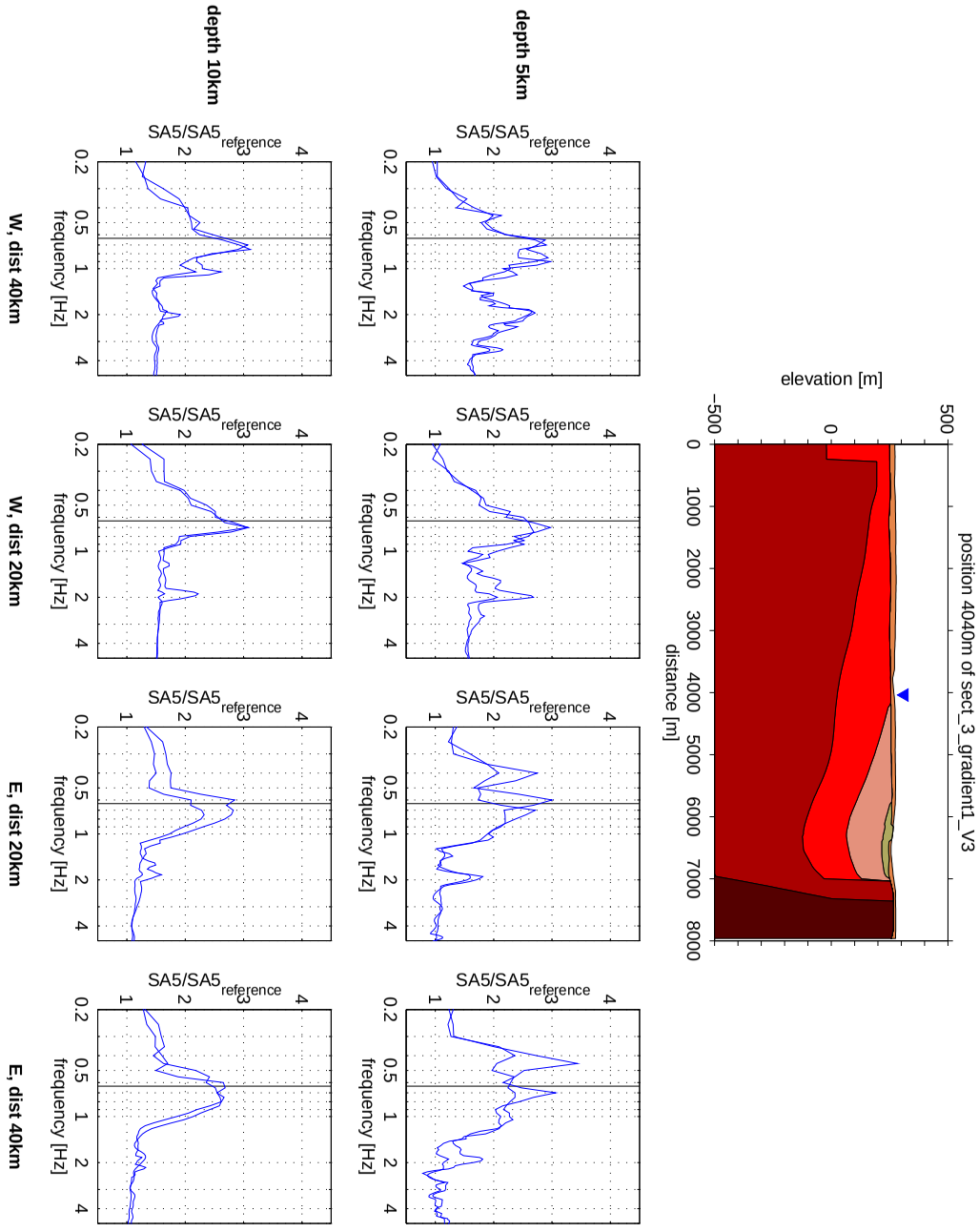

Figure 5.7: Amplification at a point over the Horst of Basle, close to the syncline of St. Jacob Tüllingen. The triangle over the geologic cross section indicates the location of the point in the Rhine graben. The amplification at this point from different scenario earthquakes are shown in individual graphs, sorted for source depth and epicentral distance. The two curves in each graph are the amplification for the two modelled source mechanisms. A vertical black line marks the fundamental frequency for the location.

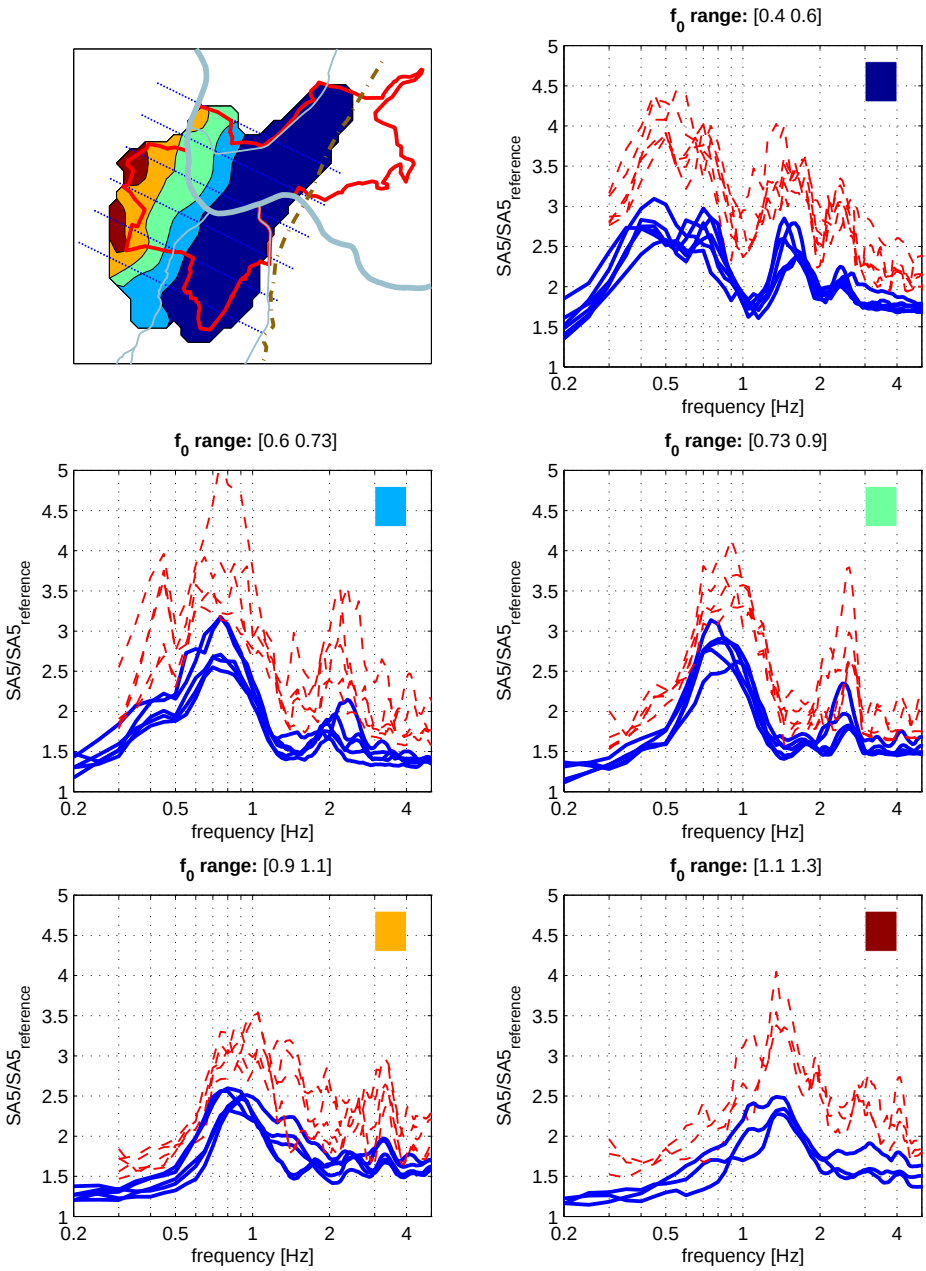

Figure 5.8: Amplification zonation along the individual sections. Five frequency ranges are differentiated, their spatial extent is indicated in the sketch with the frequency increasing from the south east to the north west. For each section and frequency range a dashed line shows the maximum amplification from all scenarios and from all points with a fundamental frequency within the specific range. At each point of a section the average amplification over all scenarios is determined and the envelope of these curves from the same points is shown as continuous line. The reasoning for the choice of frequency intervals is given in the text.

5.3 Zonation

The final step for a zonation is now the differentiation of the Basle area into zones of common amplification effects. The primary distinction in the amplifications that can be determined from the cross-sections are on one hand the focusing effects within the syncline with several peaks of amplification at higher frequencies (Fig. 5.5/5.6) and a fairly constant lowest amplification peak at a frequency in the order of 0.4Hz. On the other hand the horst of Basle with the amplification peak varying continuously with the fundamental frequency of resonance. This suggests that f_0 is a suitable indicator for the distinction of amplification zones. In chapter 2 a variability of $\pm 15\%$ has been determined for the fundamental frequencies, indicating a minimum frequency step of 15% necessary for significant distinction of varying f_0. The distinction into five frequency intervals with bounding frequencies 0.4, 0.6, 0.73, 0.9, 1.1 and 1.3 proved to be best suited as a differentiation. The first interval corresponds to the syncline of St. Jacob Tüllingen with the 2D focusing effects, while the other intervals are steps of 20% in the frequency. The spatial extent of these zones is indicated on a sketch in Fig. 5.8.

For each frequency interval and section the points with f_0 in the interval are collected and the maximum amplification from all scenarios and all points is shown as dashed line. At each point the amplifications are averaged and the envelope for all points within the same class of fundamental frequencies is shown as continuous line. Depending on the way the regional hazard is determined, one or the other is the amplification curve needed.

The agreement of the amplification curves from the different sections is remarkable. For each zone the peak amplitude of the amplification and the lower frequency limit of the first amplification peak fit very well, despite the considerable variability in the geometry of the sedimentary layers in the different sections. This applies as well for the focusing effects in the syncline (f_0 range 0.4-0.6Hz) as for the intrusion of low frequency amplification into the 0.6-0.73 f_0 range and for the peak shapes in the higher frequency ranges. Mainly the peak amplification is varied; from 2.5 to 3 for the maximum average amplifications. The very good agreement of the amplification curves confirms the validity of the 2D approach for the structure and the zoning of the Basle area by the fundamental frequency. By taking the envelope of the zonal amplifications from the individual sections we take into account the uncertainty in the structural model. This final amplification result is shown in Fig. 5.9.

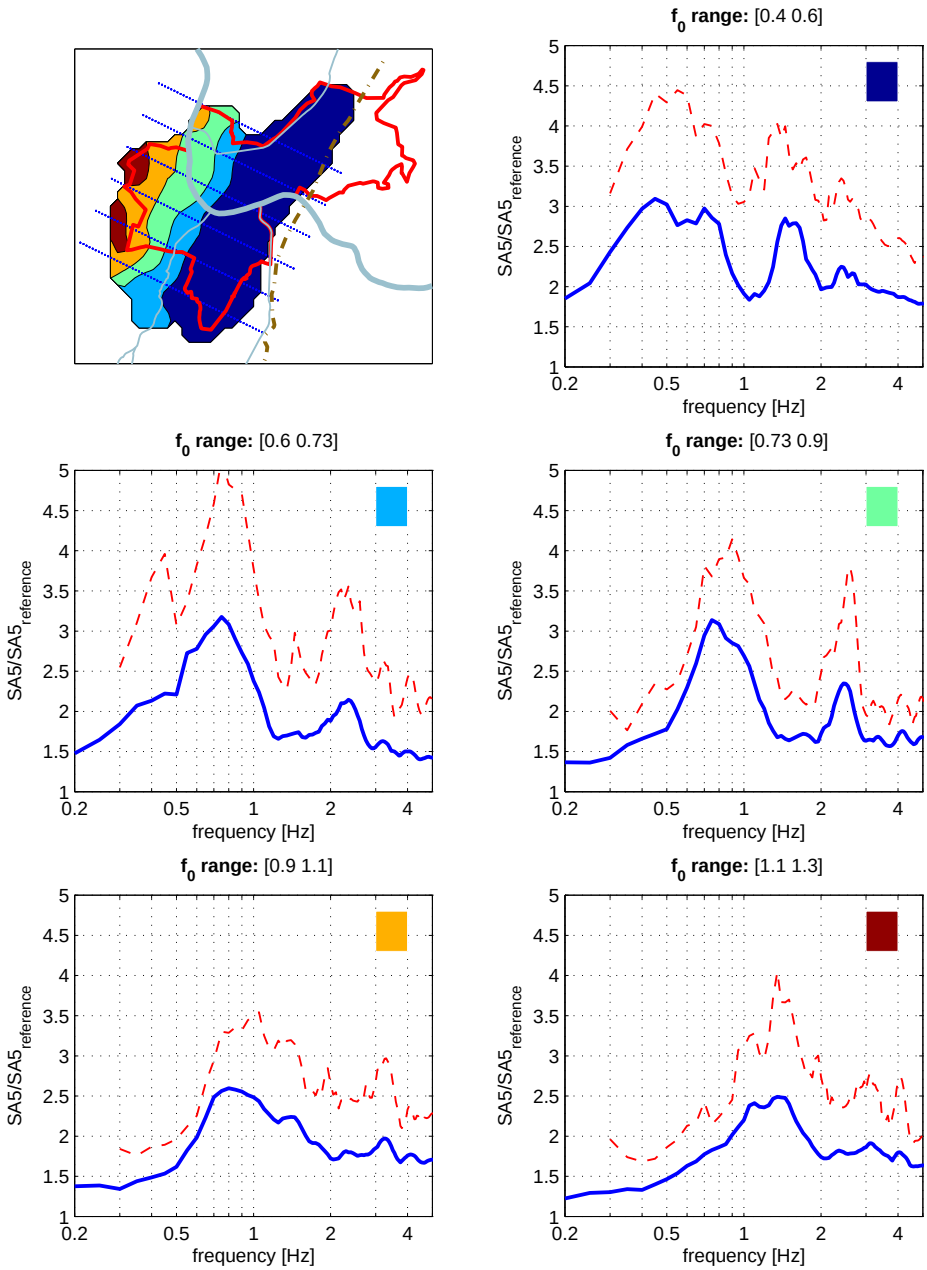

Figure 5.9: Amplification zonation for the city of Basle from the combination of all sections. The same frequency ranges as in Fig. 5.8 are considered, again the dashed line indicates overall maximum amplification from all scenarios, while the continuous line shows the envelope of the average amplification curves, selecting classes of points by the fundamental frequencies. The reasoning for the choice of intervals is given in the text.

Chapter 6

Conclusions

The level of detail in a microzonation study is on one hand a matter of available sources of information and of resources for new investigations. On the other hand the options for investigations are very limited in urban areas, where the interest for microzonation is largest. In this thesis an attempt is made at a microzonation in terms of spectral amplifications, with methods that are applicable in urban areas as well as financially inexpensive. An explicit aim of the study is to go as far as possible in the exploitation of ambient vibration methods, as they are applicable in urban areas where conventional seismic or geotechnical methods cannot be used; either because of the strength of the ambient vibration signals or restrictions by buildings, constructions and streets.

As well for the geology as for seismic P-wave velocities, information from the literature is available for the area of Basle. The large gap of uncertainty for earthquake hazard in Basle before this study were the S-wave velocities and related properties. The development and test of measurement techniques for such properties is also generally needed to improve and facilitate earthquake hazard assessment. The applied measurement methods in this thesis are based on ambient vibrations. Although the methods were known in advance to be applicable and to deliver results, they were and still are under development. So part of this work is dedicated to further develop and test these methods. On the other hand the objective was to determine quantitative and reliable data for ground motion amplification during earthquakes in the city of Basle.

The first part of the project, the H/V polarisation survey was a big success. The large amount of data collected allowed the study of the stability of the H/V polarisation curve over time and distance, showing that a single measurement of 15min duration is sufficient to determine the fundamental frequency of resonance. The low fundamental frequencies in the Rhine graben, respectively the associated large wave length, allowed to relate neighbouring measurements to each other. This proved a high reliability of the results, despite the uncertainty of $\pm 15\%$ on the actual location of f_0 for a single measurement. Especially in urban environments the level of ambient vibrations are high and disturbances

in the measurements often unavoidable. The approach of multiple and densely spaced measurements under such circumstances still allows a reliable and efficient determination of fundamental frequencies.

The value of the map of fundamental frequencies cannot be estimated high enough. In the validation of the geophysical model the determined f_0 allowed to greatly improve the weak information on the geometry of the deep S-wave velocity contrast important for the amplification effects. The change in the geometry was considerable, revealing that the sediment thickness over the horst of Basle is much larger than previously estimated: In some locations the depth changed by more than 50m over the horst of Basle, in the deeper part of the Syncline of St. Jacob Tüllingen it can be even more. This result is confirmed by information from a recent deep borehole (GPI Basle, 2001). The agreement of the first peak in the amplifications with the fundamental frequency in chapter 5 further confirms the validity to the correction of the model. This supports the approach of Ibs-von Seht & Wohlenberg (1999), who derived soft sediment thicknesses from fundamental frequencies and a known S-wave velocity contrast successfully. On the other hand the approach of estimating S-wave velocities from the knowledge of geologic sediment thickness and from the fundamental frequency was not possible in the Basle area. The example of the array measurement site Hardwald (section 3.5) showed that the S-wave velocity contrast can be significantly shifted downward from the location it would be expected from the geologic bedrock interfaces. So the sediment thickness determined from a borehole is not necessarily the relevant thickness for the fundamental frequency of resonance and site amplifications. At the array measurement site over the Tabular Jura the difference amounted to 10-15m. This is probably due to erosion of the bedrock interface or weakening from ground water intrusion, as on other sites the sedimentary thicknesses, S-wave velocities and f_0 are consistent.

The second important method tested and applied in this study is the array technique for the determination of S-wave velocities. Although the method has been studied by several authors in Japan during the last 15 years, most results have been published in Japanese only, which makes them inaccessible to us. With the tests described in section 3.5 the developed application of the array technique to ambient vibrations has proven its validity and allowed to apply it at several sites so as to determine S-wave velocities. The technique allows to determine average S-wave velocities to a depth in the order of the array aperture just from synchronous recordings of ambient vibrations even in an urban center with high human activity. The depth resolution in the order several meters of this technique is nowhere near the resolution of eg. reflection seismics, but the resolution is appropriate for seismic hazard studies. It is therefore an ideal tool for microzonation studies. A major advantage of the method is the large penetration depth, that cannot be attained with S-wave reflexion or borehole seismics in urban centers. In future work with sensors of higher Eigenperiod structural information of even deeper sediments can be determined and the combined use of the horizontal and

vertical components might allow for a more detailed understanding of the ambient vibration wave field. But before such attempts are made, the uncertainty in the measurements and in the inversion have to be determined quantitatively, so as to asses the limits of the method.

In the geophysical 3D model the results of the S-wave velocity measurements are compiled and combined with the geological information and with literature values. The results of the H/V polarisation survey allowed to verify the model and make the structural model and the S-wave velocity information consistent. This is a great success for the ambient vibration techniques, as they provide the majority of the information necessary for the later amplification calculation. But although considerable corrections had to be made to the geometry of the geological model to adapt it to the H/V results, the initial geological model was still crucial to the construction of the final model. The knowledge of the thickness of the Quaternary sediments was important in identifying the deeper sediments as being responsible for the H/V polarisation peak, and if the approximate shape of the syncline of St. Jacob Tüellingen had not been known, the H/V curves might have been considered to be not interpretable.

In the last part of this thesis the derived structural model is used to determine ground motion amplification for the city of Basle. 2D numerical simulations on sections extracted from the full structural model are used to this purpose, as the structure is predominantly 2-dimensional in the Basle area. Various scenario earthquakes are modelled to account for effects of source location and type. The determined amplifications on individual sections have peaks coinciding precisely with the fundamental frequencies calculated with a 1D approach for these sites. No 2D resonances of the syncline structure are identified, but focusing and defocusing at curved interfaces illustrates the necessity of using 2D or even 3D schemes to model amplification. The close agreement of fundamental frequencies and amplification peaks allows a zonation of the Basle area into classes of common f_0, to which average and maximum spectral amplification curves from the different scenarios are assigned.

In comparison with the detailed map from the previous qualitative microzonation of Basle (Fäh et al., 1997b; Noack et al., 1999) the zonation of the city of Basle into 5 zones might seem crude, but this is caused by fundamental differences in their content and approach. The qualitative microzonation was based primarily on a geologic classification of the Quaternary sediments, which were resolved on a grid of 25m. The H/V polarisation survey showed that the Quaternary sediments play only a minor role in the site amplification in the Basle area and the differentiated sediment classes could not be differentiated in the measurements. The fundamental frequencies identify the soft Tertiary sediments as dominant influence on site amplification. Associated to these frequencies are wave lengths in the order of kilometres, resulting in a much larger scale of the variation of ground motion amplification. On the other hand the amplification calculation was limited to frequencies between 0.2 and 5Hz; for higher frequencies

the Quaternary sediments become more relevant and will show a more differentiated amplification pattern, which is certainly associated with the local variations determined in the qualitative microzonation map. But as for the area east of the Rhine graben master fault, a resolution of structural information at a scale of the thickness of the Quaternary sediments would be necessary to resolve such effects. Such a resolution is only possible for specially selected individual locations and this kind of detail is not yet contained in the model. Fortunately the part of the city of Basle over the Tabular Jura is not densely populated and large areas are forests. But major chemical industries are located to the east of the city along the Rhine and a detailed effort to determine local site effects in future studies would be important for these sites.

With the microzonation map derived from the amplification calculations the step from a qualitative microzonation to a quantitative assessment of the local seismic hazard in the city of Basle has been successfully made. The 3D model for the area of Basle has been validated and will be used as a reference structure in future studies like 3D modelling of earthquake ground motion. The use of ambient vibration based measurement techniques to derive a model for numerical calculation of earthquake ground motion points out how in a fast and cost efficient way a structural model can be determined, facilitating deterministic earthquake hazard assessment considerably.

Appendix A

Further Array Measurements

A.1 Measurement data and inversion

Additionally to the test measurement in the Hardwald, four further array measurements were performed. The positions of these measurements are indicated on the map sketch Fig. A.1. The sites were selected to sample - beside the Quaternary at the surface - all three Tertiary sediment layers of the structural 3D model. All sites are located in flat and horizontally layered areas, where the approximation of the wave field as superposition of horizontally propagating plane waves can be assumed to be valid. The limitation of the diameter to 200m allowed on one hand a fast deployment of the instruments by just few persons and on the other hand insured that the necessary assumptions on structure and sources are justified. Two sites in the east of the city (Kannenfeldpark and Schützenmattpark) are public parks, while the sites in the northern part of Basle (Bäumlihof) and just south of Basle (Reinach) are fields of farms. The sensors used in all measurements had an Eigenfrequency of 1Hz. At all sites two data sets of 6min duration were recorded and analysed as described in chapter 3 with a phase velocity grid of 25m/s and a directional resolution of 2.5^o.

The inversion applied to the measured dispersion curves is the scheme described in section 3.5. All inversions were performed with the same approach of seven inversions and with the identical seven sets of parameter constraints for the model start. Only the inverted frequency range and the dispersion curves where adapted to the measurements. The maximum depth to which the inversions are reliable and the uncertainty in the results is depending on many factors: The site itself (involved velocities), the wave field from which the dispersion curve is derived (resolution of the array technique), the instruments used (timing precision and sensor limitations) and the inversion scheme for the S-wave velocities. The variability of the inverted profiles can be used as an indication to what depth the inverted profiles are reliable. The quality of the inverted velocity profiles decreases with depth, 100m is the estimate of the reliability of the inversions. This

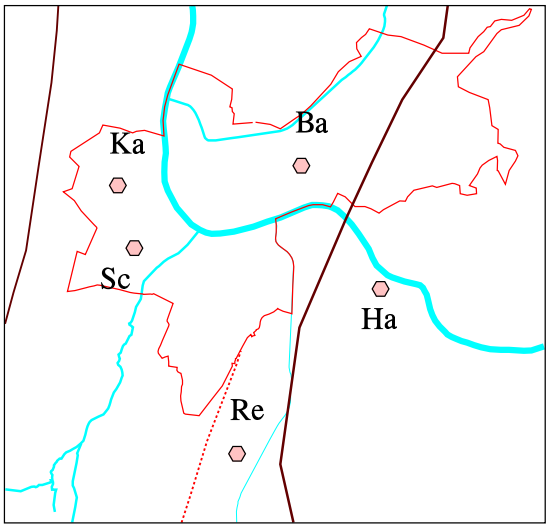

Figure A.1: Sketch of the locations of the array measurements. (Ha: Hardwald, Ka: Kannenfeldpark, Sc: Schützenmattpark, Ba: Bäumlihof, Re: Reinach)

corresponds to slightly more than half the array aperture, a suggestion made by Horike (1985). From the two validations (chapter 3) we estimate the uncertainty in the results to be less than 10%.

A.1.1 Kannenfeldpark

This measurement was done in a park in the west of the city of Basle with an area of 280m by 330m. The measurement was done in the morning just before noon, so the traffic in the city and other man made signal sources are highly active. No industry is in the near vicinity, but a train and tramway line is within a few hundreds of meters to the east.

The array configuration is given in Fig. A.2. The fundamental frequency of resonance at the site is close to 1Hz. The surface on which the sensors are placed is well kept grass, uniform for all sensors. The quality of the analysis results was very high. The dispersion curve was easily identified in the frequency range from 1.7Hz up to 10Hz with no ambiguities. The results are shown in Fig. A.3.

A.1.2 Schützenmattpark

The site Schützenmattpark also a public park within the city of Basle, but inclosed on three sides by major traffic lines with tramways. The measurement were taken in mid afternoon, so traffic was heavy and the park was also busier with people than at the site Kannenfeldpark. The buildings in the neighbourhood are again mainly housing and offices, so the close ambient vibration sources are the

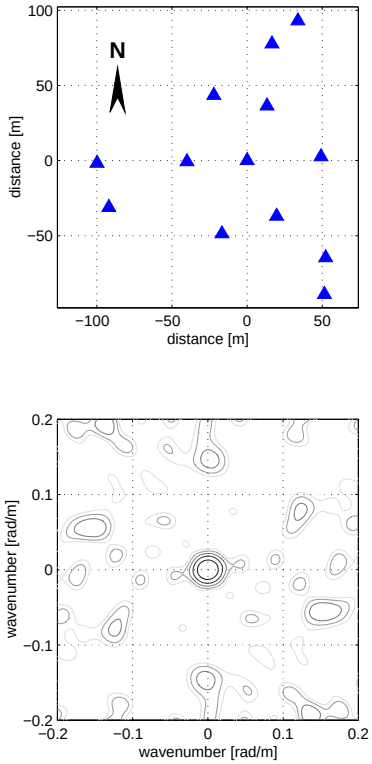

instr. ID	x-coord	y-coord
27	13.2	36.4
11	-99.8	-1.7
14	-40.0	-0.7
12	52.3	-64.6
28	16.5	77.6
13	-22.1	43.4
15	49.1	2.6
7	-16.8	-48.7
16	0.0	0.0
10	-92.0	-31.1
29	33.8	92.9
9	19.6	-36.9
8	51.4	-89.0

alias Δk	0.2 rad/m
resolution dk	0.018 rad/m
background	0.074 db

Figure A.2: Array configuration Kannenfeldpark. The positions in the table are given in meters relative to the central sensor, which has the coordinates 609950/266915 (Swiss coordinate system).

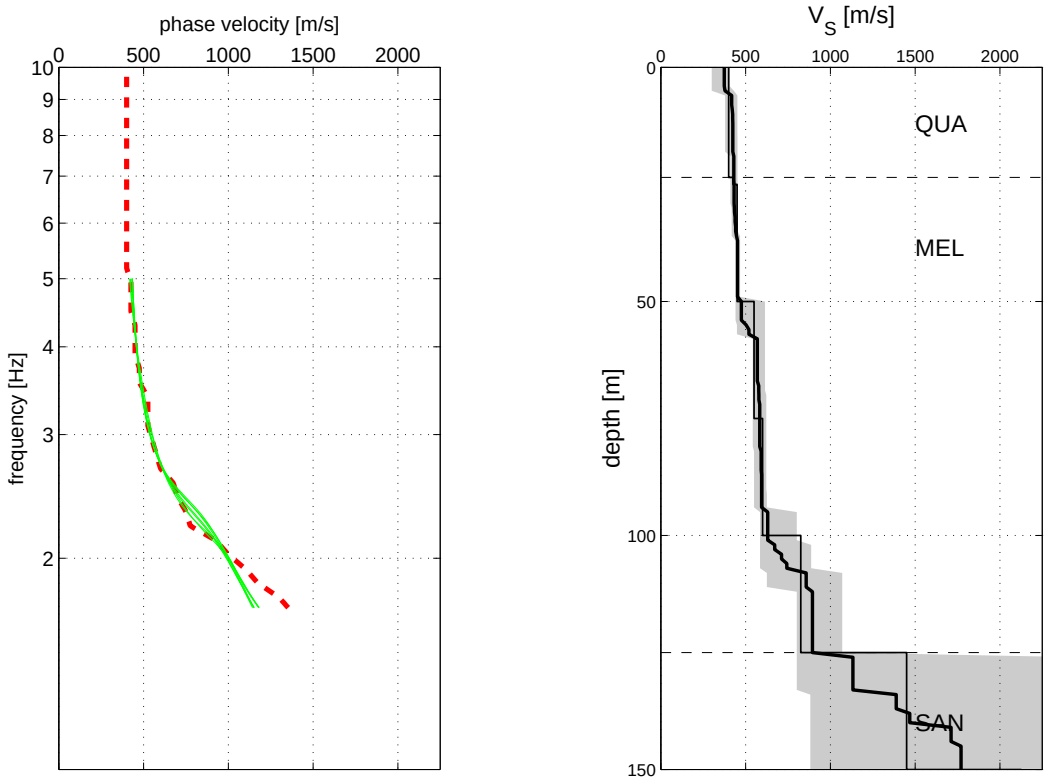

Figure A.3: Results from the array measurement Kannenfeldpark. On the left is the measured dispersion curve shown as dashed line, the dispersion of seven inverted structures are shown as thin gray lines. On the right hand the inverted S-wave velocity profiles are given: The gray shaded area indicates the range spanned by the seven inverted profiles, the thick line gives the average velocity from the inversions and the thin black line indicates average velocities for 25m depth intervals. Dashed lines indicate geological interfaces inferred from the geological 3D model.

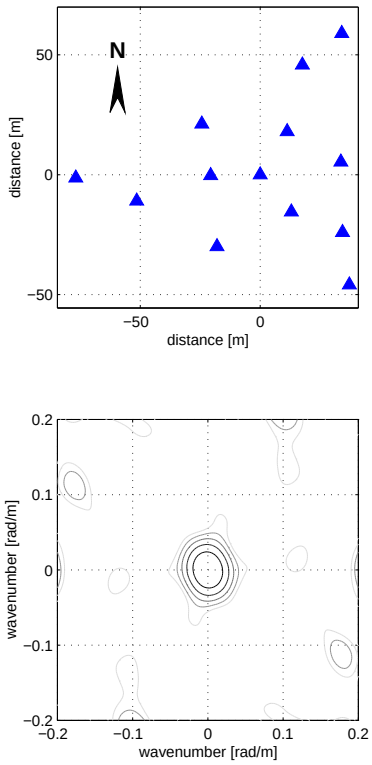

instr. ID	x-coord	y-coord
27	11.2	18.0
11	-76.9	-1.3
14	-20.7	-0.4
12	34.3	-24.0
28	17.6	45.8
13	-24.3	21.2
15	33.7	5.3
7	-18.0	-30.0
16	0.0	0.0
10	-51.5	-10.9
29	34.0	58.9
9	13.0	-15.5
8	37.2	-45.9

alias Δk	0.2 rad/m
resolution dk	0.028 rad/m
background	0.048 db

Figure A.4: Array configuration Schützenmattpark. The positions in the table are given in meters relative to the central sensor, which has the coordinates 610310/266915 (Swiss coordinate system).

traffic, while all other major sources can be assumed to be far away compared to the array aperture.

Fig. A.4 shows the configuration used. As this park is slightly smaller, the configuration was rescaled to a smaller aperture from the concept used in the Kannenfeldpark. The ground surface on which the sensors are placed is short grass, uniformly for all sensors, giving a good ground coupling. The fundamental frequency at the site is about 0.8Hz. The quality of the analysis results was very high. The dispersion curve was easily identified in the frequency range 1.9-10Hz with no ambiguities, despite the high activity within the park. The results are shown in Fig. A.5

A.1.3 Bäumlihof

The site Bäumlihof is a field of a farm within the city limits of Basle, located between the city center and the city district of Riehen. The ground surface was

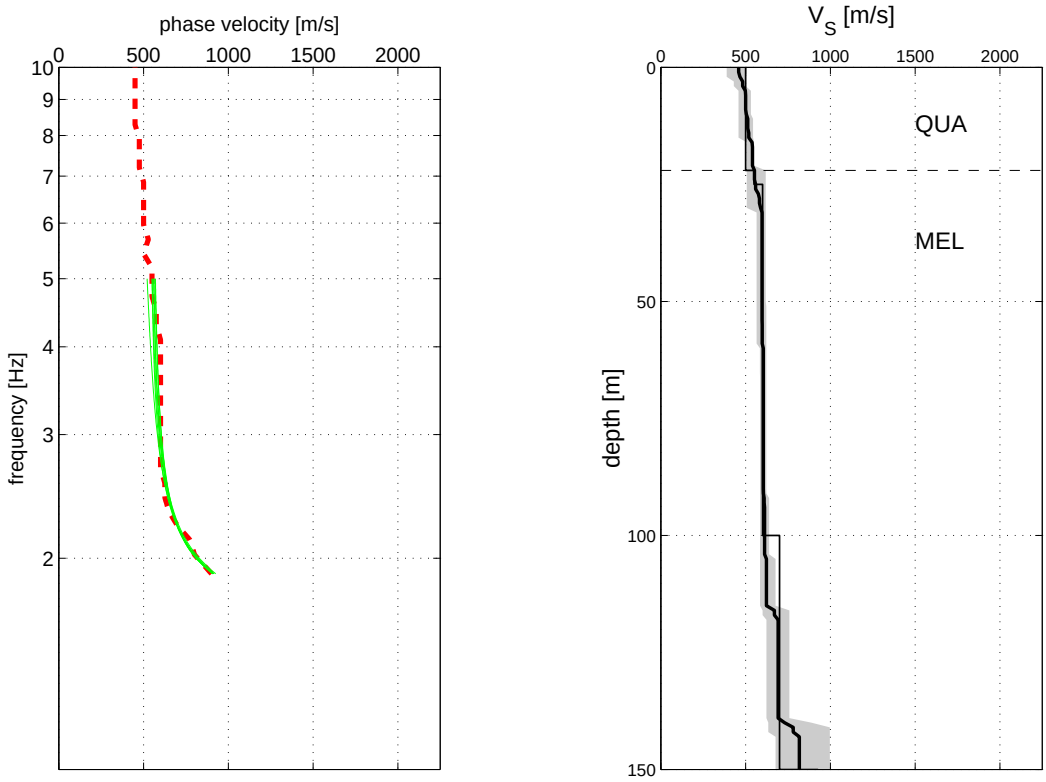

Figure A.5: Results from the array measurement Schützenmattpark. On the left is the measured dispersion curve shown as dashed line, the dispersion of seven inverted structures are shown as thin gray lines. On the right hand the inverted S-wave velocity profiles are given: The gray shaded area indicates the range spanned by the seven inverted profiles, the thick line gives the average velocity from the inversions and the thin black line indicates average velocities for 25m depth intervals. Dashed lines indicate geological interfaces inferred from the geological 3D model.

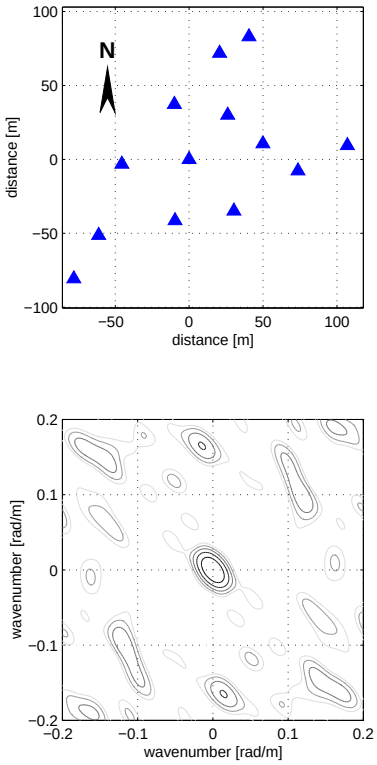

instr. ID	x-coord	y-coord
27	26.1	30.0
11	-78.0	-80.7
14	20.6	71.8
12	73.6	-7.7
28	40.5	83.0
13	-10.0	37.2
15	-9.6	-41.4
7	-45.5	-3.2
16	-61.2	-51.4
10	30.3	-34.9
29	49.9	10.6
9	0.0	0.0
8	107.1	9.4

alias Δk	0.2 rad/m
resolution dk	0.025 rad/m
background	0.071 db

Figure A.6: Array configuration Bäumlihof. The positions in the table are given in meters relative to the central sensor, which has the coordinates 614040/268770 (Swiss coordinate system).

rougher than in the parks and also the grass was standing higher. The field has slight topographic variations in the order of 1.5m, with the deepest part at the center of the array. One street with some traffic is located adjacent to the site, a major street is located 2-3 array diameters to the north.

The configuration used at the site is shown in Fig. A.6. The elongation is caused by the street in the south and the fence of a private property in the north and reflected in the lesser resolution for NW-SE directions compared to the NE-SW. The dispersion curve could be derived for the frequency range 1.7-10Hz. At each frequency level in this range the phase velocity was clearly identified in the F-k-spectrum, so the spikes and irregularities in the dispersion curve at low frequencies are either caused by wave propagation or the spectrum estimator. Fig. A.7 shows the results for Bäumlihof.

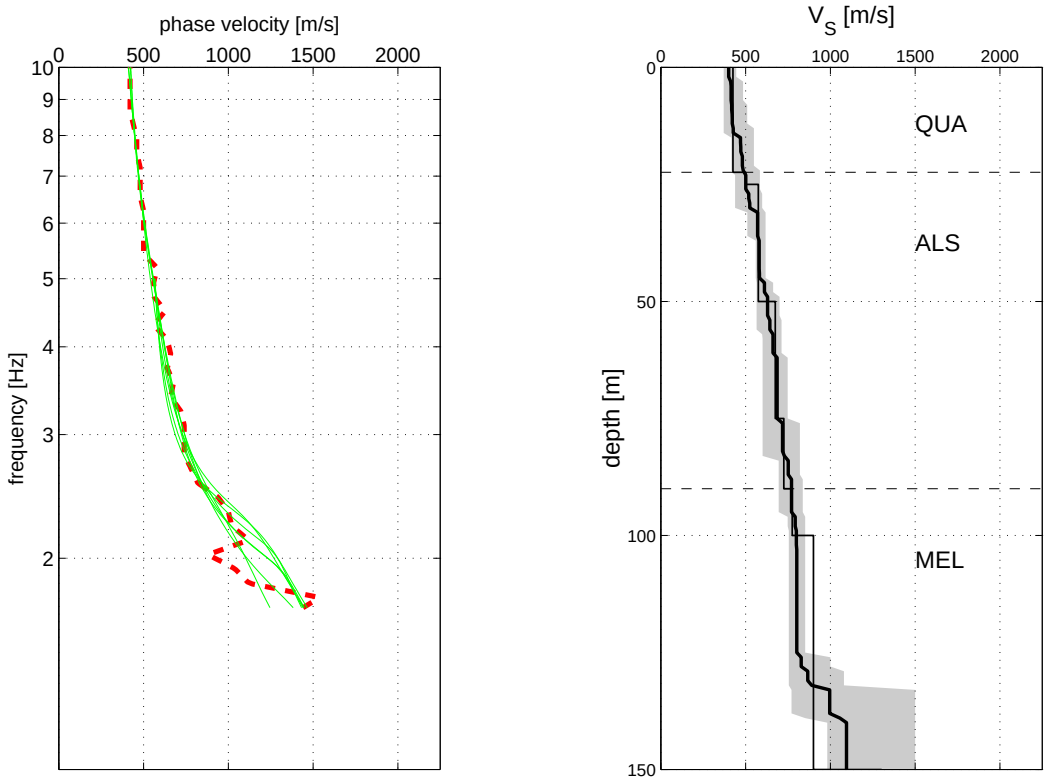

Figure A.7: Results from the array measurement Bäumlihof. On the left is the measured dispersion curve shown as dashed line, the dispersion of seven inverted structures are shown as thin gray lines. On the right hand the inverted S-wave velocity profiles are given: The gray shaded area indicates the range spanned by the seven inverted profiles, the thick line gives the average velocity from the inversions and the thin black line indicates average velocities for 25m depth intervals. Dashed lines indicate geological interfaces inferred from the geological 3D model.

A.1.4 Reinach

The site Reinach is a farm field, a few kilometres south of Basle in the syncline of St. Jacob Tüllingen. To the north further fields follow, to the west is a housing area and to the south was a construction site during the measurements. To the east a steep slope drops 10-20 meters to the ancient flood plane of the Birs in the vicinity. The slope violates the assumptions of a horizontal 1D structure, which can be seen in the results. No coherent energy can be found from this direction, although a motorway with much traffic follows the river. One of the deep boreholes is within 300m reach of the site, so the geology at this site is well known.

The measurements were done at noon time with a L-shaped configuration. The configuration (Fig. A.8) was a test for the case where the site situation does not allow an arbitrary configuration, as it is the case in an urban area. The dominant signals in the f-k-spectrum are coming from the north and south, in the axis of the syncline. The dispersion curve was derived exclusively from signals from this direction to avoid the possible problems from the slope in the east of the array. Fig. A.9 shows the dispersion and inversion results for Reinach, the dispersion curve could be derived for 1.5-10Hz.

A.1.5 Hardwald

For completeness the configuration position table for the Hardwald measurement (Fig. A.10) is included here as well, the dispersion result with the inverted structures is included as well (Fig. A.11).

A.2 S-wave velocity interpretation

The inversion of the dispersion curves measured by the array measurements yield seven S-wave velocity profiles for each measurement site that fit the dispersion curve. To derive S-wave velocities for the geological units of the geological model several steps are necessary. First the seven inverted profiles at each site are averaged. Second the profiles have to be interpreted for velocities of the geologic units encountered at the sites. Large scale average velocities are derived, as the values are to be extrapolated over the whole Basle area.

From the geological 3D model the geological interfaces are inferred at the measurement sites. The thickness of the Quaternary sediments is well defined from the borehole database (Noack, 1993). The depth of the deeper interfaces have uncertainties in the order of several tens of meters, so the shape of the velocity profile is taken into account in discriminating deeper interfaces. In view of the minimum wave length of 40m (400m/s phase velocity at 10Hz) the depth profiles are simplified to average velocities for 25m depth intervals for each geological unit; indicated as thin black lines in the result figures A.3-A.11.

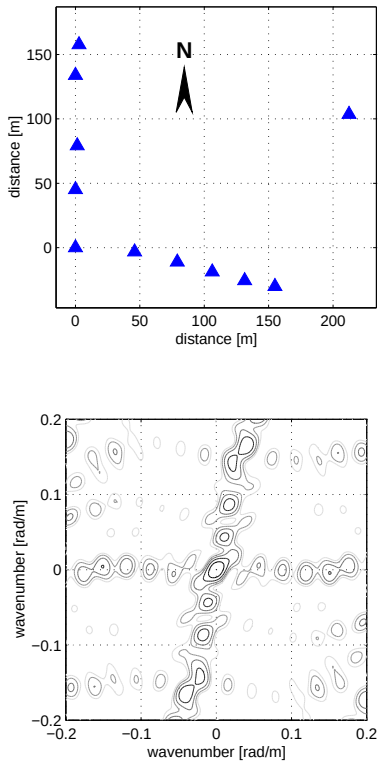

instr. ID	x-coord	y-coord
27	2.8	157.6
11	0.0	45.1
14	106.2	-18.7
12	0.0	0.0
28	0.0	133.8
13	131.3	-25.5
15	1.4	79.1
16	45.9	-3.2
29	154.9	-30.1
9	212.4	103.6
8	79.1	-11.1

alias Δk	0.09 rad/m
resolution dk	0.018 rad/m
background	0.108 db

Figure A.8: Array configuration Reinach. The positions in the table are given in meters relative to the central sensor, which has the coordinates 612515/262260 (Swiss coordinate system).

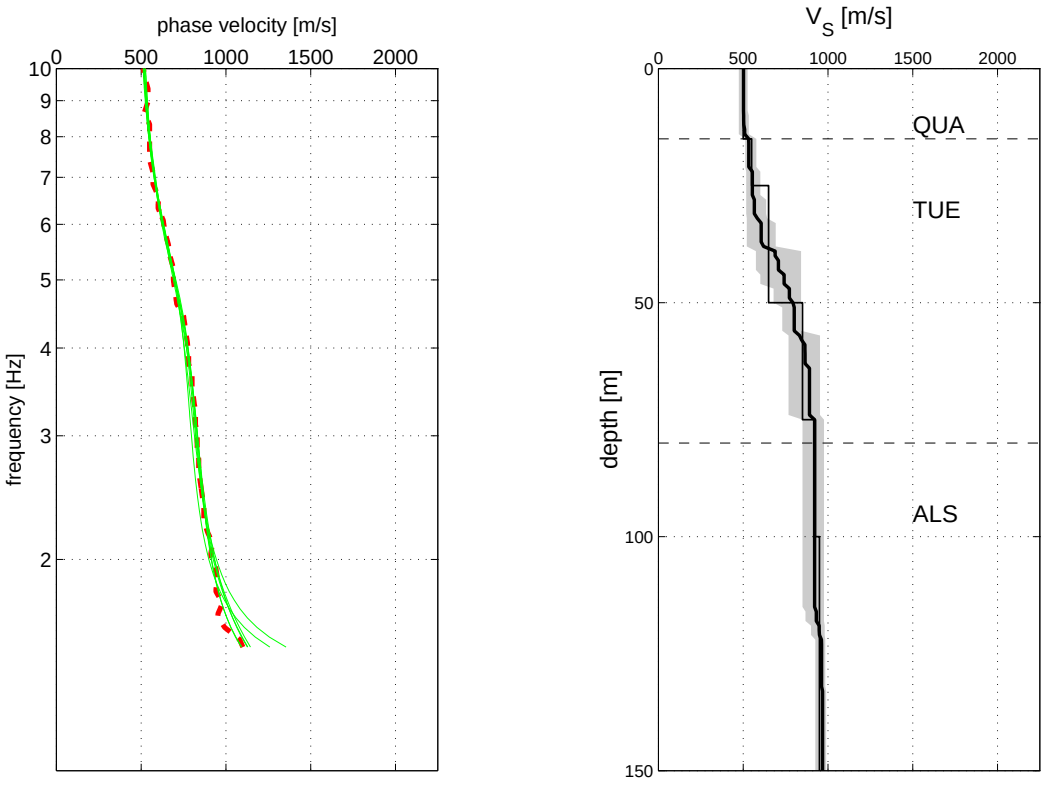

Figure A.9: Results from the array measurement Reinach. On the left is the measured dispersion curve shown as dashed line, the dispersion of seven inverted structures are shown as thin gray lines. On the right hand the inverted S-wave velocity profiles are given: The gray shaded area indicates the range spanned by the seven inverted profiles, the thick line gives the average velocity from the inversions and the thin black line indicates average velocities for 25m depth intervals. Dashed lines indicate geological interfaces inferred from the geological 3D model.

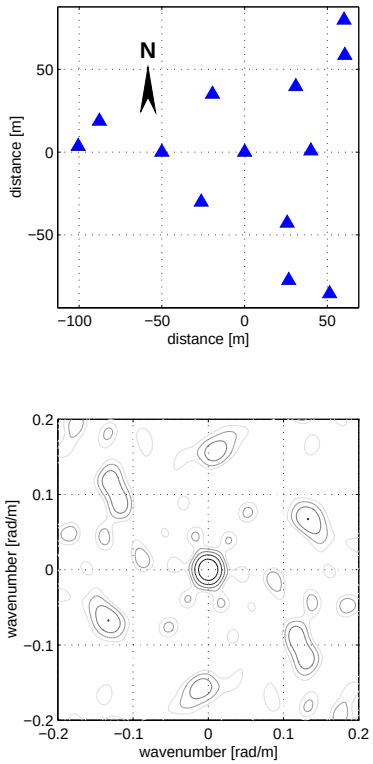

instr. ID	x-coord	y-coord
27	51.4	-85.5
11	-100.5	3.5
14	26.7	-77.5
12	60.6	58.5
28	25.7	-42.8
13	60.1	79.8
15	40.1	0.7
7	0.0	0.0
16	-50.0	0.0
10	30.9	39.6
29	-26.2	-30.2
9	-87.8	18.7
8	-19.4	35.0

alias Δk	0.2 rad/m
resolution dk	0.018 rad/m
background	0.07 db

Figure A.10: Array configuration Hardwald. The positions in the table are given in meters relative to the central sensor, which has the coordinates 615815/266015 (Swiss coordinate system).

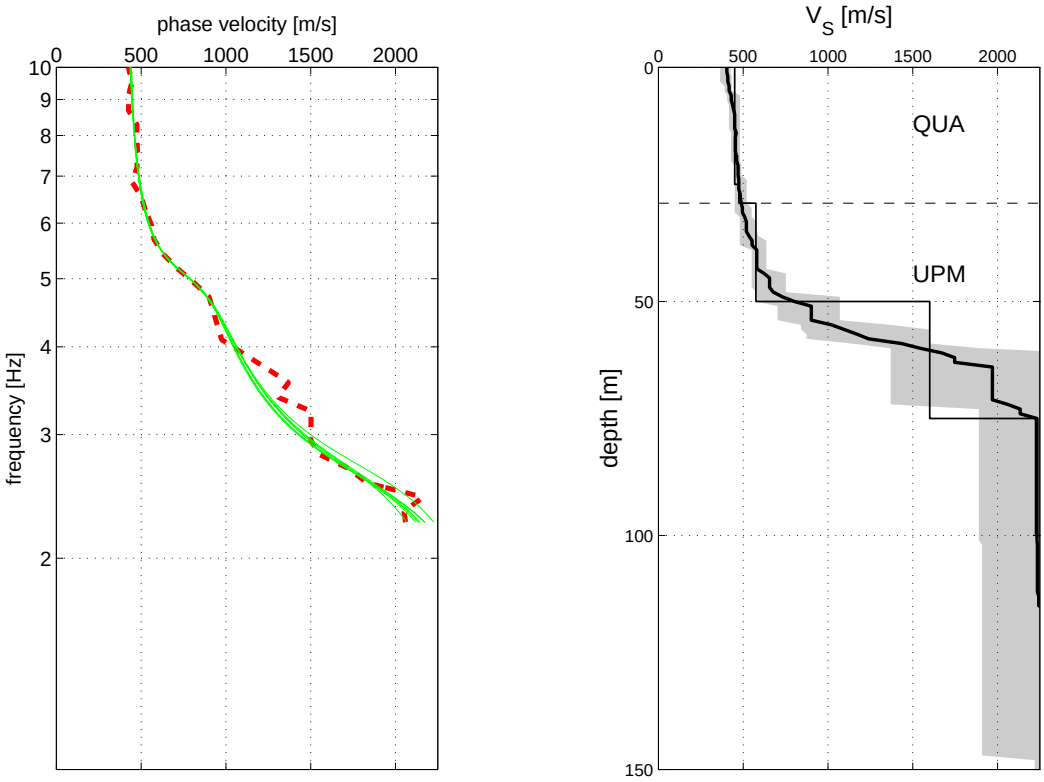

Figure A.11: Results from the array measurement Hardwald. On the left is the measured dispersion curve shown as dashed line, the dispersion of seven inverted structures are shown as thin gray lines. On the right hand the inverted S-wave velocity profiles are given: The gray shaded area indicates the range spanned by the seven inverted profiles, the thick line gives the average velocity from the inversions and the thin black line indicates average velocities for 25m depth intervals. Dashed lines indicate geological interfaces inferred from the geological 3D model.

Table A.1: S-wave velocities for the Tertiary sediments, averaged for depth intervals from the array measurements. Below 100m depth the values are extrapolations. In the last row the average for the first 100m of sediments is given with the uncertainty range in the measurements (AV_{100}).

depth[m]	$V_S(MEL)$ [m/s]	$V_S(ALS)$ [m/s]	$V_S(TUE)$ [m/s]
25-50	600	575	650
50-75	600	675	850
75-100	600	725	925
100-150	650	775	1000
150-200	650	825	1025
200-250	700	850	1050
250-300	700	875	1075
300-350	750	900	1100
AV_{100}	600 (450-700)	650 (600-800)	725 (650-900)

For the Quaternary sediments the S-wave velocities are in the range of 400m/s to 500m/s with an average of 450m/s. The measurement in the Hardwald is the only one reaching into the lower Mesozoic sediments over the Tabular Jura. It indicates weathered or weakened material at the top of this material with velocities as low as the Quaternary. Below 60m the velocities increase rapidly to 2000m/s and more, but the resolution in the measurement is lost there.

Better resolved are the Tertiary sediments TUE, ALS and MEL. TUE is found in the Reinach measurement, showing a velocity gradient of 550m/s at 17m depth up to 925m/s at 80m depth. ALS shows some gradient as well at Bäumlihof (500m/s at 22m up to 750 at 90m), with a lesser gradient below 80m in the Reinach measurement. The MEL has constant 600m/s at Schützenmattpark, while it has a slight gradient or step in the measurement Kannenfeldpark. We favour the constant value from Schützenmattpark, as it agrees for both measurements at depth. We attribute the lower values below the Quaternary sediments to weakening at the top of the MEL which we cannot resolve in this model. The results for the Tertiary sediments are compiled in Table A.1, offering velocity functions with a gradient or an average value for the first 100m.

Appendix B

Borehole logs Otterbach

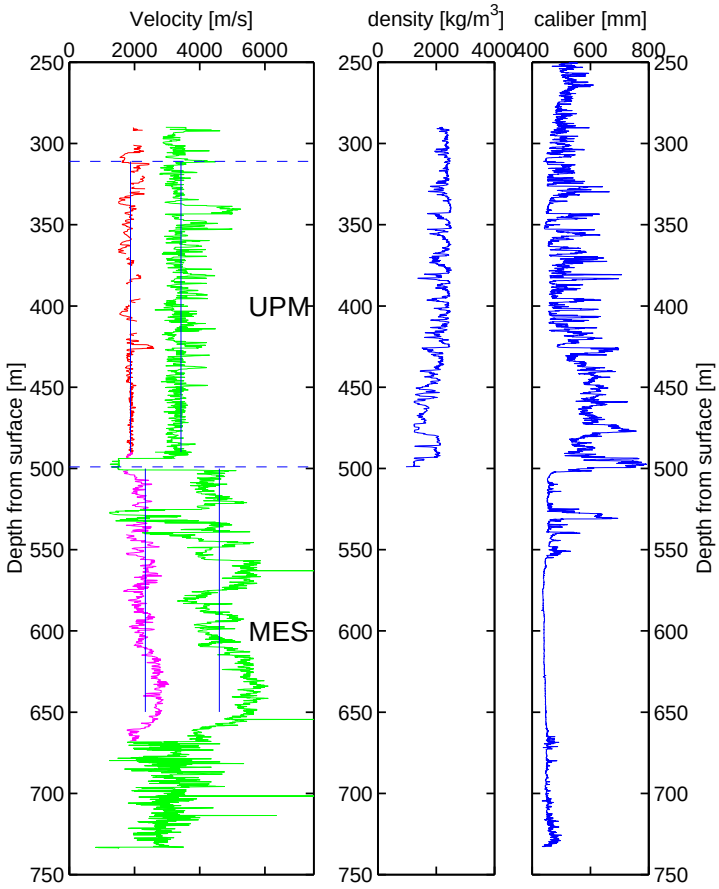

Figure B.1: Sonic log results from the deep Borehole Otterbach (GPI Basle, 2001). The lower velocity values are S-wave velocities, the higher values the P-wave velocities. Vertical lines indicate the average values for the geologic units separated by the horizontal dashed lines. Only data for the shown depth range were available from the borehole.

Appendix C

Amplification along all sections

Collection of the amplification results described in chapter 5. The spectral amplifications are calculated as follows: On each section response spectra at 5% damping are calculated for accelleration ($SA5$). On a section from a reference structure (regional average bedrock model as used for the regional hazard) the same response spectra are calculated ($SA5_{bedrock}$). The ratio between the two response spectra defines the amplification of the ground motion relative to the regional mean.

For each section the mean and the maximum spectral amplifications are shown. The lower part of the figures show the geometry of the cross-section used in the simulation, triangles indcate the positions where amplifications were calculated. The upper part of the figures show in color code the mean or maximum spectral amplifications along the section, dependent on location and frequency. The black line identifies the fundamental frequencies calculated from the model, which agree very well with the frequency of the peak amplification.

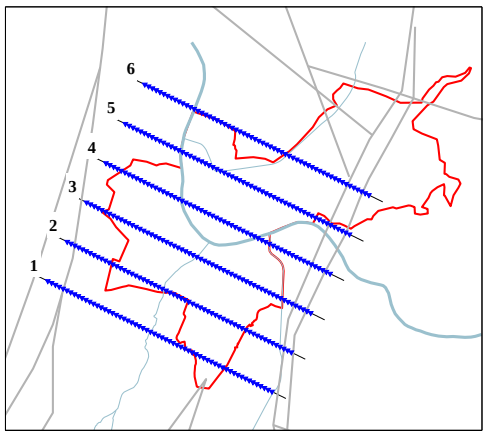

Figure C.1: Sketch of the location of the sections.

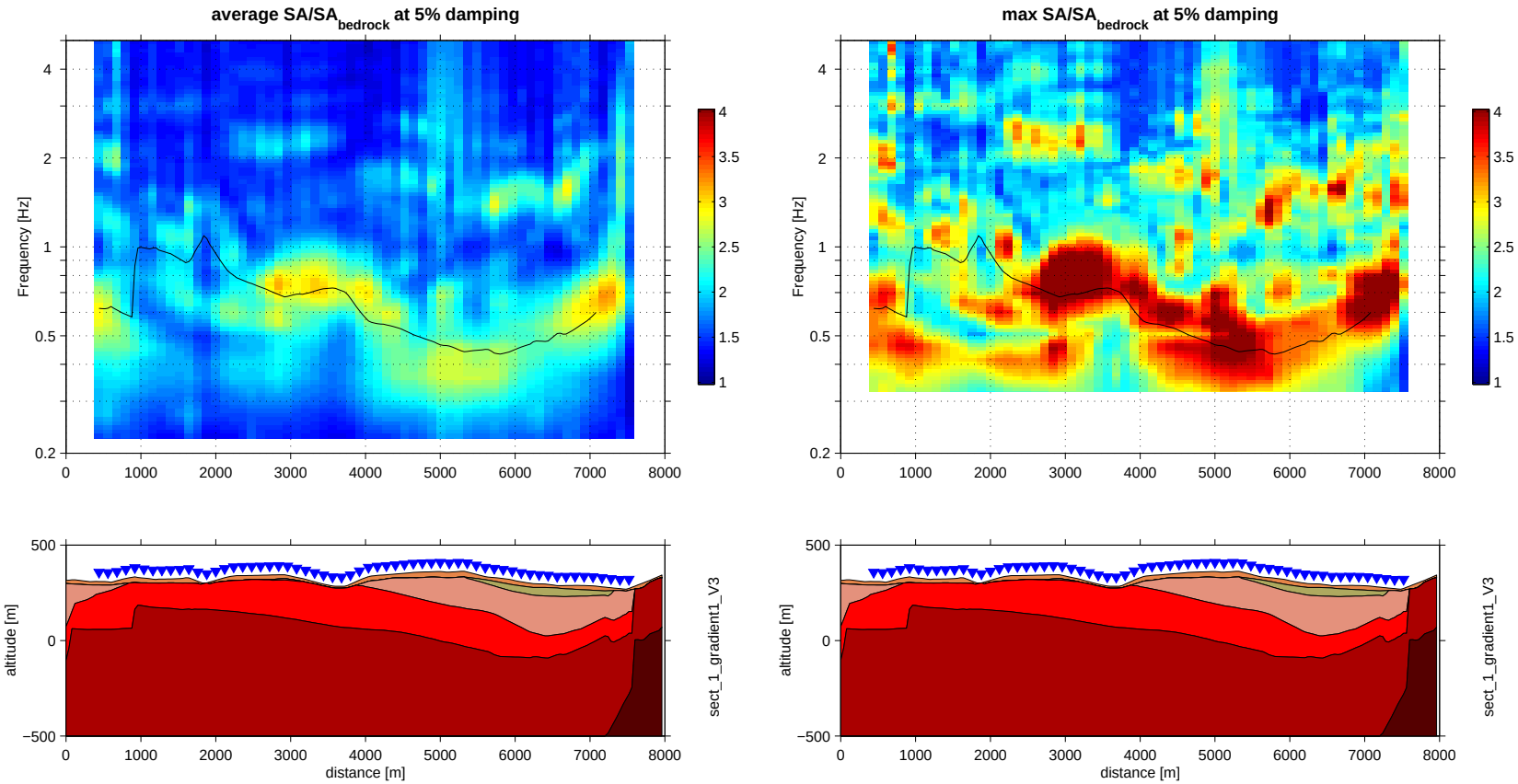

Figure C.2: Mean and maximum amplification along section 1

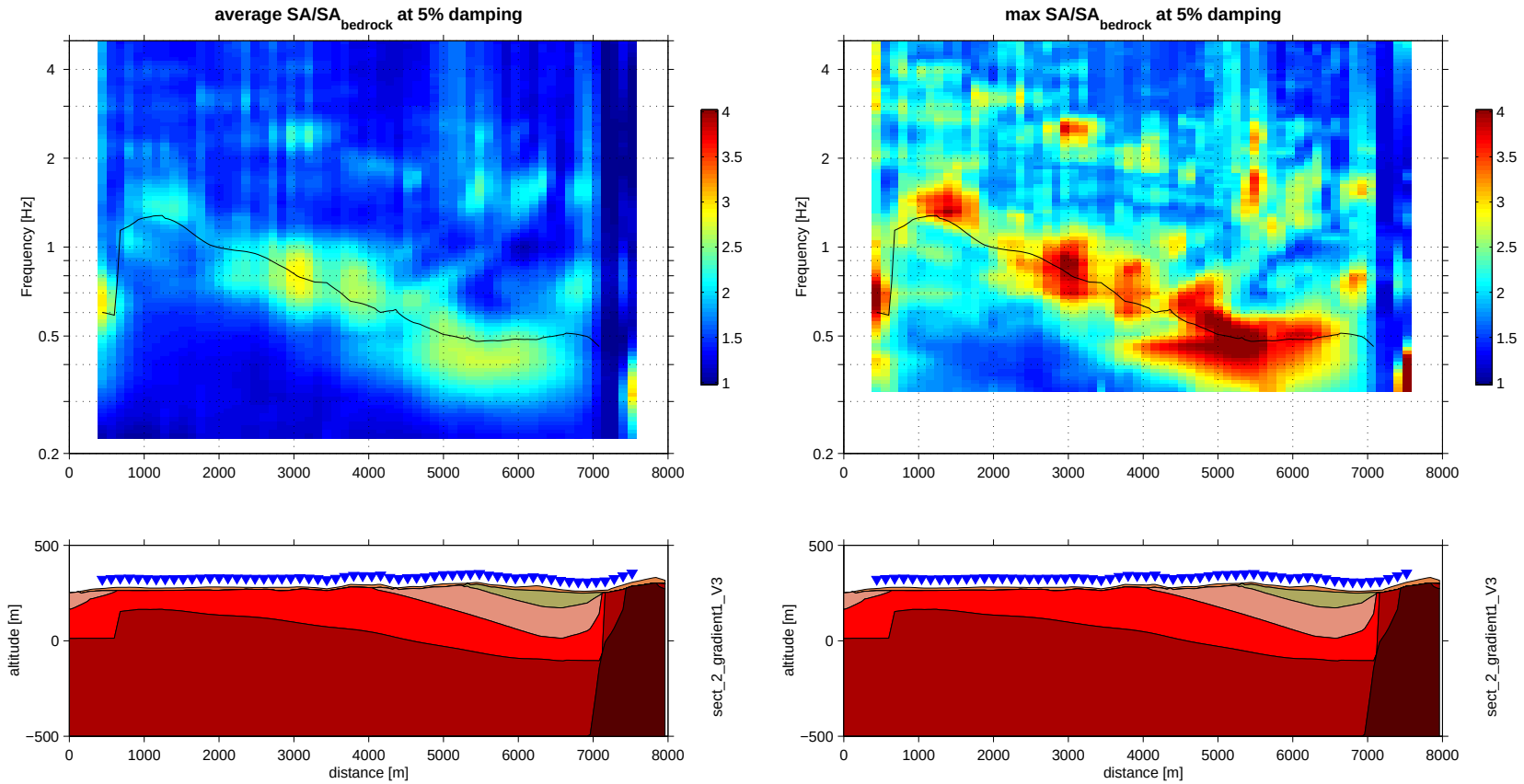

Figure C.3: Mean and maximumamplification along section 2

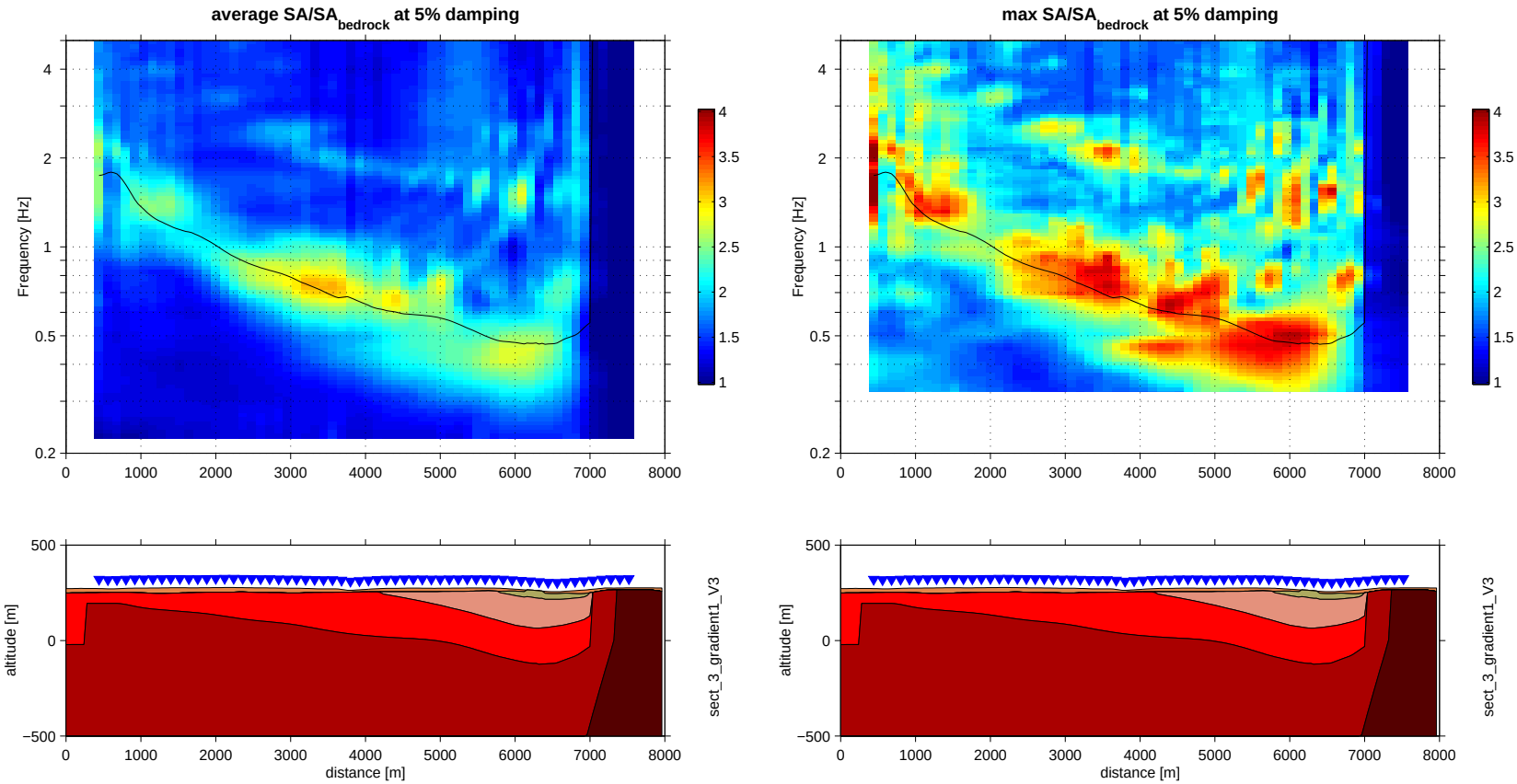

Figure C.4: Mean and maximumamplification along section 3

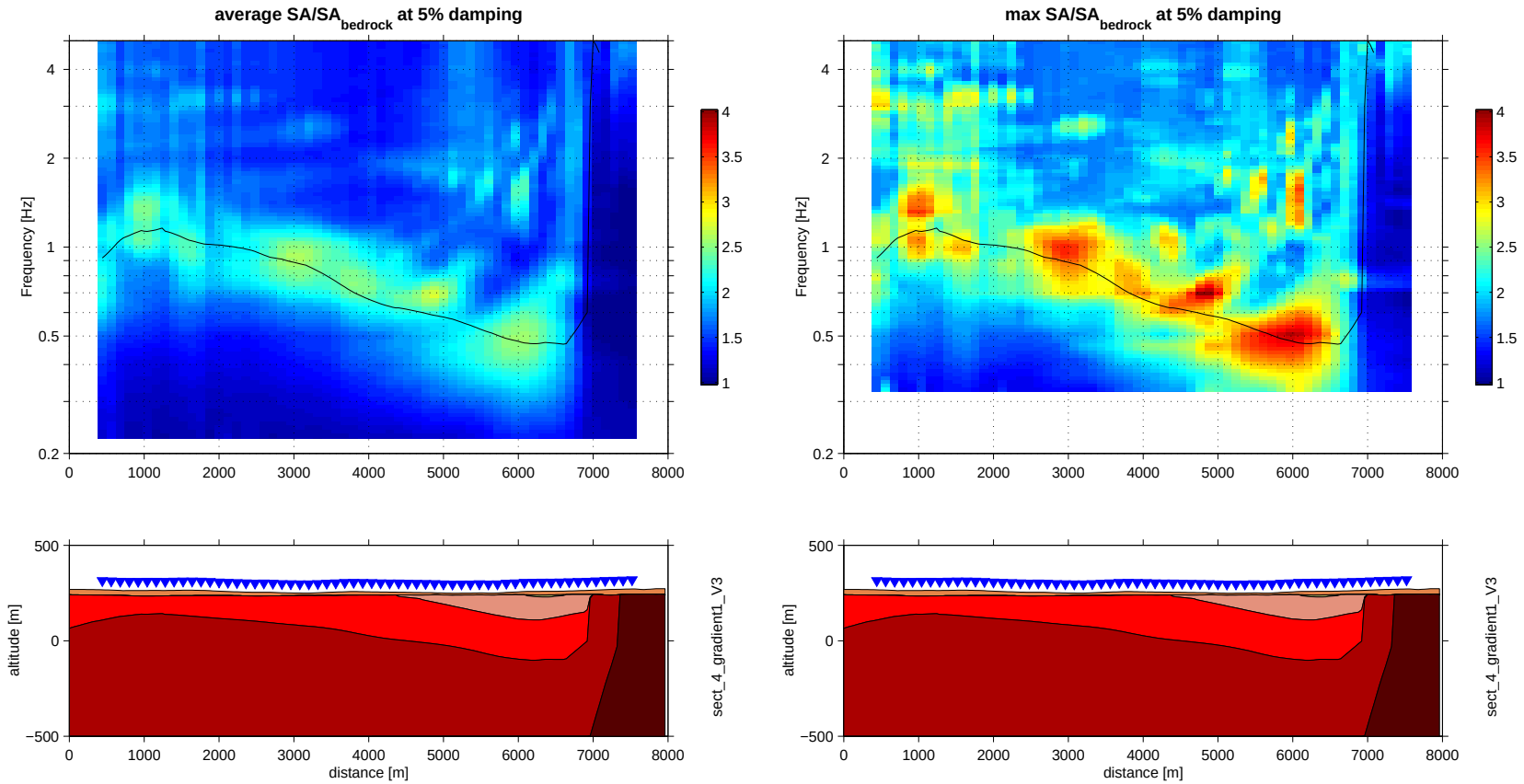

Figure C.5: Mean and maximumamplification along section 4

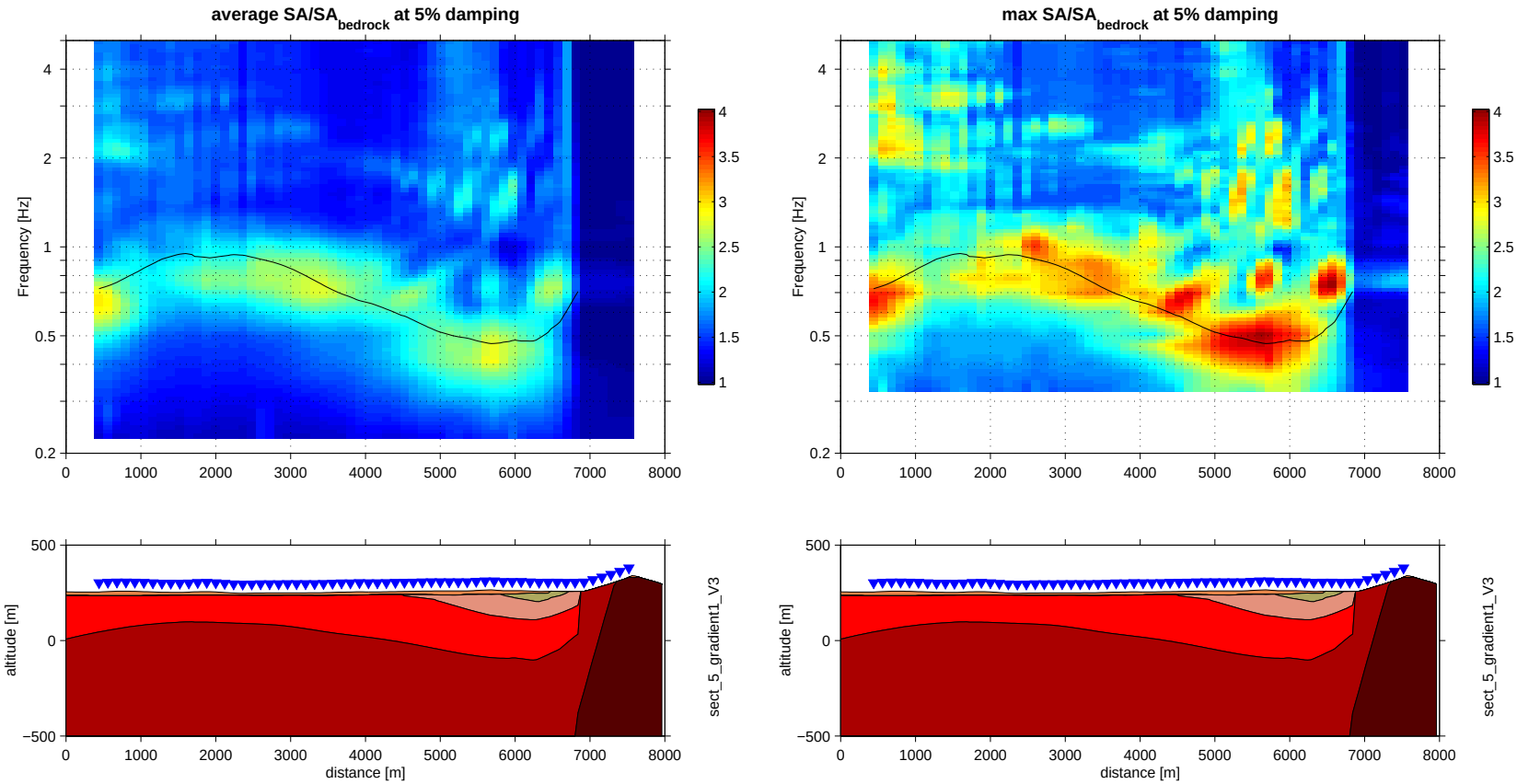

Figure C.6: Mean and maximumamplification along section 5

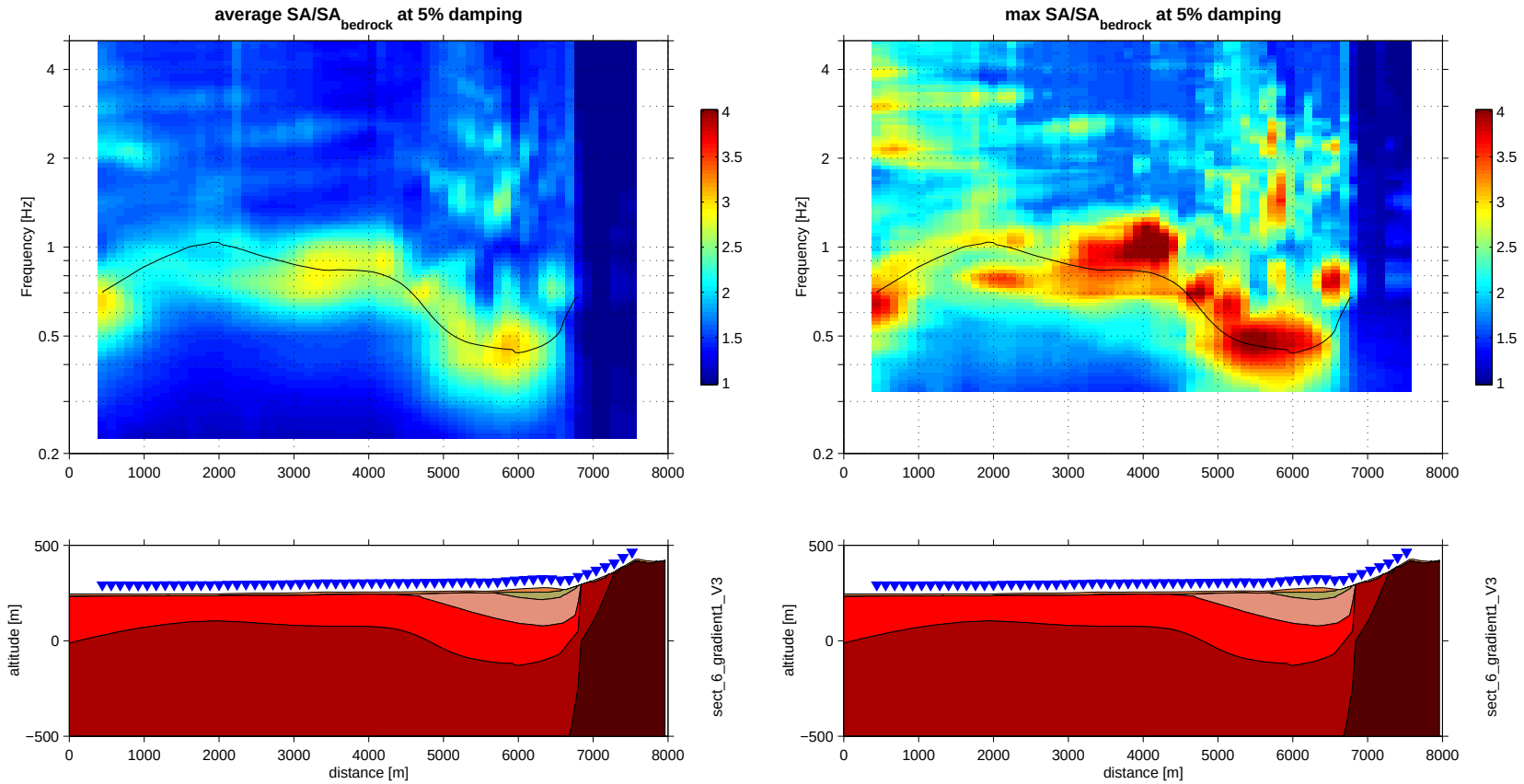

Figure C.7: Mean and maximumamplification along section 6

List of Publications

Kind, F., Fäh, D. and Giardini, D. Application of an array technique to ambient vibrations, *Geophysical Journal International*, accepted for publication

Kind, F., Fäh, D., Steimen, S., Salami, F. and Giardini, D. 2000. On the Potential of Microtremor Measurements, *Proceedings of the 12.WCEE 2000, 30. Jan - 4. Feb 2000*, Auckland, New Zealand, paper No 204

Kind, F., Fäh, D., Giardini, D. 2000. Determination of local structures from ambient vibrations, *Proceedings of the 6.ICSZ, 12. - 15. Nov 2000*

Fäh, D., Kind, F., Lang, K. and Giardini, D. 2001. Earthquake scenarios for the city of Basel, *Soil Dynamics and Earthquake Engineering*, 21, 405 - 413

Fäh, D., Kind, F. and Giardini, D. 2001. A theoretical investigation of average H/V ratios, *Geophysical Journal International*, 145, 535 - 549

Fäh, D., Kind, F. and Giardini, D. 2002. Structural Information Extracted from Microtremor Wavefields, in *Proceedings of the 12. European Conference on Earthquake Engineering*, Paper Reference 819, Elsevier Science Ltd., in press

Fäh, D., Bachmann, H., Bay, F., Becker, A., Giardini, D., Huggenberger, P., Kind, F., Lang, K., Mayer-Rosa,D., Noack, T., Sellami, S. und Wenk, T. 2000. Earthquake Scenarios for Switzerland, *Proceedings of the 12.WCEE 2000*, 30. Jan - 4. Feb 2000, Auckland, New Zealand, paper No 205

Deichmann, N., Baer, M., Braunmiller, J., Ballarin Dolfin, D., Bay, F., Delouis, B., Fäh, D., Giardini, D., Kastrup, U., Kind, F., Kradolfer, U., Kuenzle, W., Roethlisberger, S., Schler, T., Salichon, J., Sellami, S., Spuehler, E., Wiemer, S. 2000. Earthquakes in Switzerland and surrounding regions during 1999, *Eclogae geol. Helv.*, 93/3, 395-406

Baer, M., N. Deichmann, D. Ballarin Dolfin, F. Bay, B. Delouis, D. Fäh, D. Giardini, U. Kastrup, F. Kind, U. Kradolfer, W. Kuenzle, S. Roethlisberger, T. Schler 1999. Earthquakes in Switzerland and surrounding regions during 1998, *Eclogae geol. Helv.*, 92, 265-273

Acknowledgements

This work would not have been accomplished without the help of many persons. First of all I want to thank my supervisor Dr. Donat Fäh for his guidance and patient support throughout the project. He introduced me to seismic hazard in the first place and the concepts on which the thesis is built are his. At the same time I want to thank Prof. Domenico Giardini for refereeing the thesis, his supportive advise on the papers and the interpretation of the results and last but not least the generous opportunities he provided at the institute and abroad.

Many thanks to Eric Zechner, Thomas Noack and Peter Huggenberger for their friendly and helpful cooperation, the input on the geology of Basle and for providing the model geometry, which was fundamental in many parts of the thesis. I thank Prof. Frank Scherbaum for accepting to be co-examiner and the valuable comments on the array technique.

A special thanks I want to extend to Sibylle Steimen for her moral support throughout my work, which was crucial at many times, and for her help in the measurements. Further I want to thank Eva Spühler, Francesca Bay, Kerstin Lang, Stefan Wiemer, Arnfried Becker, Jochen Wössner and Antonia Zeidler for the good discussions, their comradeship and for keeping the spirits high in our research group. Significant support was also coming from the technical and administrative personnel of the institute, by helpfully smoothing the way through the day to day technical and administrative problems.

Curriculum Vitae

Fortunat Johannes Paul Kind
Date of birth: March 10, 1971
Citizenship of Chur, GR, Switzerland

4.1977-4.1983 Primary school, Zürich, ZH, Switzerland

4.1983-9.1990 Gymnasium, type B (Latin and English), Kantonsschule Hohe Promenade, Zürich, ZH, Switzerland

9.1990-10.1991 Practical with ACSS civil engineers, Zürich, job at the railway post office, Zürich main station, Military service ("Rekrutenschule") in the Swiss Army Music (2.1991-6.1991), Herisau, AR, travelling through Canada, hiking, canoeing

10.1991-4.1998 Masters in mathematics, ETH Zürich, Switzerland
Core subject: Numerical analysis
10.1992; 1. Vordiplom
10.1993; 2. Vordiplom
10.1993-10.1994; Part time work for Swissair, visiting lectures in psychology and geography at the Univeristy of Zurich
9.1995-6.1996; Erasmus exchange year at the University of East Anglia, Norwich, GB; applied mathematics and oceanography
10.1997-4.1998 Diploma thesis on "Mass errors in regional numerical weather forecast models, caused by boundary conditions"

5.1998-2.2002 Ph.D. position at the Swiss Seismological Service, ETH Zürich

Bibliography

Asten, M. W. & Henstridge, J. D., 1984. Array estimators and the use of microseisms for reconnaissance of sedimentary basins, *Geophysics*, **49**(11), 1828–1837.

Barber, N. S., 1959. Design of 'optimum' arrays for direction finding, *Electronic and Radio Engineer*, **36**, 222–232.

Bay, F., 2002. *Ground Motion Scaling in Switzerland: Implications for Probabilistic seismic Hazard Assessment*, Ph.D. thesis, ETH Zürich, Switzerland.

Becker, A., Davenport, C., Haeberli, W., Burga, C., Perret, R., Flisch, A., & Keller, W., 2000. The Fulnau landslide and former lake Seewen in the northern Swiss Jura mountains, *Eclogae geol. Helv.*, **93**, 291–305.

Becker, A., Davenport, C., & Giardini, D., 2001. Palaeoseismicity studies on end-pleistocene and holocene lake deposits around Basle, *Geophysical Journal International*, in press.

Ben-Menahem, A. & Harkrider, D. G., 1964. Radiation patterns of seismic surface waves from buried dipolar sources in a flat stratified earth, *Journal of Geophysical Research*, **69**, 2605–2620.

Bitterli-Brunner, P. & Fischer, H., 1988. *Erläuterungen zum Geologischen Atlas der Schweiz, Blatt Arlesheim (1067)*, Landeshydrologie- und geolgie, Bern.

Borcherdt, R. D., 1970. Effects of local geology on ground motion near San Francisco bay, *Bull. Seis. Soc. America*, **60**, 29–61.

Bundesamt für Zivilschutz, 1995. Katastrophen und Notlagen in der Schweiz: Eine vergleichende Übersicht, Bundesamt für Zivilschutz, Bern.

Capon, J., 1969. High-resolution frequency-wavenumber spectrum analysis, *Proceedings of the IEEE*, **57**(8), 1408–1418.

Carpenter, E. W., 1965. A historical review of seismometer array development, *Proceedings of the IEEE*, **53**, 1816–1833.

Clark (Ed.), S. P., 1966. *Handbook of Physical Constants - Revised Edition*, The Geological Society of America, Memoir 97.

Cornell, C. A., 1968. Engineering seismic risk analysis, *Bull. Seis. Soc. America*, **58**, 1583–1606.

Cox, H., 1973. Resolving power and sensitivity to mismatch of optimum array processors, *Journal of the Acoustical Society of America*, **54**, 771–785.

Emmerich, H. & Korn, M., 1987. Incorporation of attenuation into time-domain computations of seismic wave fields, *Geophysics*, **52**, 1252–1264.

Faccioli, E., 1991. Seismic amplification in the presence of geological and topographic irregularities, in *Proceedings of the Second International Conference on Recent Advances in Geotechnical Earthquake Engineering and Soil Dynamics, March 11-15, St. Louis, Missouri*, vol. 2, pp. 1779–1797.

Fäh, D., 1992. *A hybrid technique for the estimation of strong ground motion in sedimentary basins*, Ph.D. thesis, Swiss Federal Institute of Technology (ETH) Zürich, Nr. 9767.

Fäh, D., Noack, T., & Kruspan, P., 1997. Bewertung des geologischen Untergrundes der Region Basel Stadt auf die seismische Erschütterungsfähigkeit, in *Erdbebengefährdung und Mikrozonierung in der Schweiz, Schlussbericht NFP31*, edited by D. Mayer-Rosa, pp. 55–67, VdF Hochschulverlag AG.

Fäh, D., Kind, F., & Giardini, D., 2001. A theoretical investigation of average H/V ratios, *Geophysical Journal International*, **145**, 535–549.

Fäh, D., Kind, F., & Giardini, D., 2001. Earthquake scenarios for the city of Basle, *Soil Dynamics and Earthquake Engineering*, **21**, 415–429.

Fäh, D. J., Rüttener, E., Noack, T., & Kruspan, P., 1997. Microzonation of the city of Basle, *Journal of Seismology*, **1**, 87–102.

Field, E. H. & Jacob, K. H., 1995. A comparison and test of various site-response estimation techniques including three that are not reference-site dependent, *Bull. Seis. Soc. America*, **85**, 1127–1143.

Finn, L., 1991. Geotechnical engineering aspects of seismic microzonation, in *Proceedings of the Fourth International Conference on Seismic Zonation, August 25-29, Stanford, California*, vol. 1, pp. 199–259.

Fischer, H., Hauber, L., & Wittmann, O., 1971. *Erläuterungen zum Geologischen Atlas, Blatt Basel (1047)*, Schweiz. Geol. Kommision, Bern.

Florsch, N., Fäh, D., Suhadolc, P., & Panza, G. F., 1991. Complete synthetc seismograms for high-frequency multimode SH-waves, *Pageoph.*, **136**, 529–560.

Futtermann, W. I., 1962. Dispersive body waves, *Journal of Geophysical Research*, **67**, 5279–5291.

GOCAD, 1999. *Geological Object Computer Aided Design software v1.5.7*, National School of Geology, Nancy.

GPI Basle, 2001. Borehole Otterbach II, Geologic- Paleontologic Institute (GPI) of the University of Basle, Canton Basle City, unpublished data.

Gürler, B., Hauber, L., & Schwander, M., 1987. *Geologie der Umgebung von Basel mit Hinweisen über die Nutzungsmöglichkeiten der Erdwärme*, no. N.F. 160 in Beitr. geol. Karte Schweiz, Swiss Geological Commission.

Guttierez, C. & Singh, S. K., 1992. A site effect study in Acapulco, Guerrero, *Bull. Seis. Soc. America*, **83**, 1042–1063.

Harjes, H.-P., 1990. Design and siting of a new regional array in Central Europe, *Bull. Seis. Soc. America*, **80**, 1801–1817.

Haskell, N. A., 1953. The dispersion of surface waves in multilayered media, *Bull. Seis. Soc. America*, **43**, 17–34.

Haubrich, R. A., 1968. Array design, *Bull. Seis. Soc. America*, **58**, 977–991.

Horike, M., 1985. Inversion of phase velocity of long-period microtremors to the S-wave-velocity structure down to the basement in urbanized areas, *Journal of Physics of the Earth*, **33**, 59–96.

Ibs-von Seht, M. & Wohlenberg, J., 1999. Microtremor measurements used to map thickness of soft sediments, *Bull. Seis. Soc. America*, **89**, 250–259.

ISSMFE, 1994. *Manual for zonation on seismic geotechnical hazards*, Japanese Society of Soil Mechanics and Foundation Engineering, TC4 of ISSMFE (Chairmanship: Prof. K. Ishihara).

Jongmanns, D. & Campillo, M., 1990. The 1983 Liège earthquake: Damage distribution and site effects, *Earthquake Spectra*, **6**, 713–737.

Kagami, H., Okada, S., Takai, N., & Murakami, H., 1995. Seismic zonation maps of Sapporo metropolitan area, northern Japan, derived from dense questionnaire surveys of seismic intensity, in *Proceedings of the Fifth International Conference on Seismic Zonation*, vol. II, pp. 1043–1050, Nice, France.

Kawase, H., Satoh, T., Iwata, T., & Irikura, K., 1998. S-wave velocity stucture in the San Fernando and Santa Monica areas, in *The Effects of Surface Geology on Seismic Motion*, edited by K. Kudo, H. Okada, & T. Sasatani, pp. 733–740, A.A.Balkema.

Korn, M. & Stöckl, H., 1982. Reflecion an transmission of love channel waves at coal seam discontinuities computed with a finite difference method, *Journal of Geophysics*, **50**, 171–176.

Kudo, K., 1995. Practical estimates of site response, state-of-the-art report, in *Proceedings of the Fifth International Conference on Seismic Zonation*, vol. III, Ouest Editions, Presses Academiques.

Lachet, C. & Bard, P.-Y., 1994. Numerical and theoretical investigations on the possibilities and limitations of Nakamura's technique, *Journal Physics of the Earth*, **42**, 377–397.

Lang, K., 2001. *Seismic vulnerability of existing buildings*, Ph.D. thesis, ETH Zürich, Switzerland.

Lermo, J. & Chavez Garcia, F. J., 1994. Are microtremors useful in site response evaluation?, *Bull. Seis. Soc. America*, **84**, 1350–1364.

Liu, H.-P., Boore, D., Joyner, W., Oppenheimer, D., Warrick, R., Zhang, W., Hamilton, J., & Brown, L., 2000. Comparison of phase velocities from array measurements of rayleigh waves associated with microtremor and results calculated from borehole shear-wave velocity profiles, *Bull. Seis. Soc. America*, **90**, 679–689.

Matsushima, T. & Okada, H., 1990. Determination of deep geological structures under urban areas using long-period microtremors, *Butusuri-Tansa*, **43**, 21–33.

Mayer Rosa, D. & Merz, H., 1976. Seismic risk maps of Switzerland. Description of the probabilistic method and discussion of the input parameters, in *Seismic risk assessment for nuclear power plants, Proc. of ESC Symposium*, edited by A. R. Ritsema, pp. 45–52, ESC, Luxembourg.

Meghraoui, M., Delouis, B., Ferry, M., Giardini, D., Huggenberger, P., Spottke, I., & Granet, M., 2001. Active normal faulting in the Upper Rhine Graben and paleoseismic identification of the 1356 Basle Earthquake, *Science*, **293**, 2070–2073.

Milana, G., Barba, S., Del Pezzo, E., & Zambonelli, E., 1996. Site response from ambient noise measurements: New perspectives from an array study in Central Italy, *Bull. Seis. Soc. America*, **86**, 320–328.

Müller, S. & Mayer Rosa, D., 1980. The new seismic hazard maps for Switzerland, *Rev. Geofisica*, **13**, 7–19.

Mykkeltveit, S., 1985. A new regional array in Norway, desing and work and results from analysis of data from a provisional installation, in *The VELA Program. A Twenty-Five Year Review of Basic Research*, edited by A. U. Kerr, pp. 546–553, Defense Advanced Research Projects Agency, U.S.A.

Nakamura, Y., 1989. A method for dynamic characteristics estimation of subsurface using microtremor on the ground surface, *Quaterly Reports of the Railway Technical Research Institute, Tokyo*, **30**, 25–33.

Noack, T., 1993. Geologische Datenbank der Region Basel, *Eclogae geol. Helv.*, **86**, 283–301.

Noack, T., Kruspan, P., Fäh, D., & Rüttener, E., 1999. Mikrozonierung von Basel-Stadt, *Geologischer Bericht Nr. 24, Landeshydrologie und -Geologie Schweiz*.

Panza, G. F., 1985. Synthetic seismograms: The rayleigh waves modal summation, *J. Geohphysics*, **58**, 125 – 145.

Panza, G. F. & Suhadolc, P., 1987. Complete strong motion synthetics, in *Seismic strong motion synthetics*, edited by B. A. Bolt, vol. 4 of **Computational Techniques**, pp. 153–204, Academic Press.

Ramirez, j. E., 1940. An experimental investigation of the nature and origin of microseisms at St. Louis, Missouri, *Bull. Seis. Soc. America*, **30**, 139–178.

Rovelli, A., Singh, S. K., Malagnini, L., Amato, A., & Cocco, M., 1991. Feasibility of the use of microtremors in estimating site response during earthquakes: some test cases in Italy, *Earthquake Spectra*, **7**, 551–561.

Rüttener, E., 1995. *Earthquake hazard evaluation for Switzerland*, Ph.D. thesis, ETH Zürich, Switzerland.

Sägesser, R. & Mayer Rosa, D., 1978. Erdbebengefährdung in der schweiz, *Schweizerische Bauzeitung*, **78/7**, 3–18.

Schwab, F. & Knopoff, L., 1972. Fast surface wave and free mode computations, in *Methods in Computational Physics*, edited by B. A. Bold, vol. 11, pp. 87–180, Academic Press, New York.

Sebe, O., 1997. Contribution methodologique pour l'etablissement de cartes d'alea sismique corrige local, dans une perspective de planification territoriale, Tech. Rep. 2 DAP 01-97-1005, Laboratoire regional des Ponts et Chaussees de Strasbourg, (in French).

Steimen, S., 1999. *2-D Resonanzen in der Mulde von St. Jacob Tüllingen*, Master's thesis, ETH Zürich.

Steimen, S., Fäh, D., Kind, F., Schmid, C., & Giardini, D., 2002. Identification of 2-D resonance in microtremor wave fields, *Bull. Seis. Soc. America*, submitted.

Takeuchi, H. & Saito, M., 1972. Seismic surface waves, in *Methods in computational physics*, edited by B. A. Bold, vol. 11, pp. 217–295, Academic Press, New York.

Toksöz, M., 1964. Microseisms and an attempted application to exploration, *Geophysics*, **24**, 154–177.

Udwadia, F. E. & Trifunac, M. D., 1973. Comparison of earthquake and microtremor ground motions in El Centro, California, *Bull. Seis. Soc. America*, **63**, 1227–1253.

Woods, J. W. & Lintz, P. L., 1973. Plane waves at small arrays, *Geophysics*, **38**, 1023–1041.

Yamanka, H., Dravinski, M., & Kagami, H., 1993. Continuous measurements of microtremors on sediments and basement in Los Angeles, California, *Bull. Seis. Soc. America*, **83**, 1595–1609.

Yamanka, H., Takemura, M., Ishida, I., & Niwa, M., 1994. Characteristics of long-period microtremors and their applicability in exploration of deep sedimentary layers, *Bull. Seis. Soc. America*, **84**, 1831–1841.

Zechner, E., Kind, F., Fäh, D., & Huggenberger, P., 2001. 3-D Geological modell of the Southern Rhinegraben compiled on existing geological data and geophysical reference modeling., in *Abstract Volume of the 2nd EUCOR-URGENT Workshop, 7.-11. October, Mont Saint-Odile, Strasbourg, France*, p. 43.